

# Ion Conductance Through Potassium Channels

Studied by Molecular Dynamics Simulations

International Max-Planck Research School  
for Physics of Biological and Complex Systems  
Göttingen Graduate School for  
Neurosciences, Biophysics and Molecular Biosciences  
Georg August Universität Göttingen

PhD Thesis

by

**David Alexander Köpfer**

Göttingen, 2015

**Thesis Committee Members:**

Professor Dr. Bert de Groot (Reviewer)  
Max Planck Institute for Biophysical Chemistry, Göttingen

Professor Dr. Ralf Ficner (Reviewer)  
Georg August University, Göttingen

Professor Dr. Andreas Janshoff  
Georg August University, Göttingen

**Further Members of the Examination Board:**

Professor Dr. Claudia Steinem  
Georg August University, Göttingen

Professor Dr. Luis Pardo  
Max Planck Institute for Experimental Medicine, Göttingen

Professor Dr. Helmut Grubmüller  
Max Planck Institute for Biophysical Chemistry, Göttingen

**Date of the disputation:** 20.04.2015

To my parents

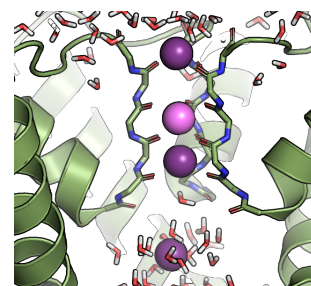


## Abstract

$K^+$  channels are at the basis of fundamental physiological processes in virtually all cells. These functions range from maintaining cell homeostasis to being involved in the nerve signaling process. Their basic function lies in their ability to efficiently mediate the passage of  $K^+$  ions across the membrane along their chemical gradient at rates close to the diffusion limit, while at the same time denying the passage of other physiologically relevant ions—foremost the smaller  $Na^+$  ions.  $K^+$  channels form the largest and most diverse group of ion channels, whose duration and magnitude of electric response differs in response to a variety of external stimuli among their members. For  $K^+$  channels, a wealth of data is available from over half a century of electrophysiology and more recently from an increasing number of atomistic structures, solved by x-ray crystallography. Based on this data, the selectivity filter (SF), the narrowest passage for ions at the extracellular mouth of the channel, has been identified as a core functional element of all  $K^+$  channels. The SF has shown to instantiate the  $K^+$  selectivity of  $K^+$  ions over other ion species, while allowing almost barrierless transition of  $K^+$  ions. Furthermore, the SF has shown to act as a gate regulating the current through the channel.

In this thesis, we employ MD simulations to combine structural information from x-ray crystallography with functional data from electrophysiology to gain insights into the mechanics of the SF of  $K^+$  channel in general. For direct comparison to the electrophysiological single channel recordings we employ the computational electrophysiology method, a setup which allows to subject the channel to a sustained trans-membrane voltage by maintaining an ionic imbalance. Using this setup we were able to induce spontaneous ion permeation across the channel, allowing direct measurement of the channel's most important observable—its current.

Based on this setup, we looked at the permeation process itself and found that—contrary to the textbooks— $K^+$  ions pass through the SF with direct ionic contacts, rather than with interspersed water molecules. Indeed, we found evidence that these direct contacts are key for efficient ion translocation in many different  $K^+$  channels. Additionally we investigated the role of the SF in the permeation process and found a concerted motion of the SF backbone carbonyl-oxygen atoms during



the ion permeation process, that serve to shield the high charge density of the ions. By restraining the SF flexibility we found this motion to be extremely sensitive, to even sub-Ångström perturbations. These findings should help our understanding of the impact on channel conductance from small mutations in the vicinity of the SF. Furthermore, we found the same setup under biionic conditions capable of reproducing the channel selectivity for  $K^+$  ions over  $Na^+$  ions. The data from these simulations presents a solid basis to test various kinetic and thermodynamic models of ion permeation, that have been proposed.

Apart from the permeation of ions, we also looked at changes of the SF structure and their impact on the channel conductance. Using the rapidly inactivating  $K^+$  channel hERG, we showed how alterations in the supporting hydrogen bond network behind the SF are capable of switching the SF conformation between a high  $K^+$  concentration state and a low  $K^+$  concentration state, which helps to understand how the conductance changes in C-type inactivation might be regulated. To gain further insights into this inactivation process we compared long simulations of wild type (WT) and inactivation-impaired mutants of  $K^+$  channels. The difference between these two channels shows a structural rearrangement that impacts on the SF and the gating helices at the same time and seems to be mediated via the pore helices (PH). Such a mechanism could explain the experimentally observed coupling between gating and C-type inactivation.

These deep insights into the channel mechanics can provide a basis for better models of drugs designed to target  $K^+$  channels and may also prove useful in understanding hereditary diseases that are grounded in channel mutations.

## Acknowledgment

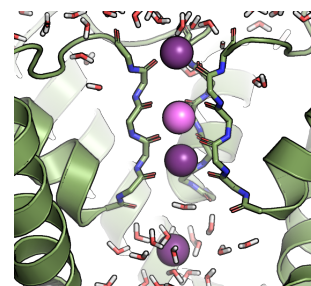
I owe my deepest gratitude to my supervisor Prof. Bert deGroot for his guidance throughout this thesis. He has always been there for me, oftentimes on short notice, patiently listening to all questions and doubts and offering practical solutions. I am very grateful for the freedom he granted me to follow my own research interests and I admire his open and honest way of convincing with facts and clear reasoning rather than authority.

I am indebted to Prof. Ulrich Zachariae for investing much of his scarce time and energy into educating me about  $K^+$  channels and preventing me from losing sight of the big questions. His passion and desire for knowledge have always inspired me. I am very grateful for all the honest and friendly advice on both, scientific and personal questions, he has given me.

I would like to thank the members of my Thesis Committee Prof. Janshoff and Prof. Ficner for their time and helpful discussions about the projects. I thank Petra Kellers and Eveline Heinemann for their day to day help with organizational issues. I thank Martin Fechner, Carsten Kutzner and Ansgar Esztermann for their help with the many computer problems that came up over the years, not to speak of the problems they wholly prevented. I want to express my gratitude to the coordinators of the "Göttinger Graduiertenschule für Neurowissenschaften, Biophysik und Molekulare Biowissenschaften (GGNB) Graduate School": Frauke Bergmann, Tina Trost and especially Antje Erdmann, whose efforts in supporting and encouraging me during troubled times was invaluable. I also acknowledge the funding from the GGNB and the Max Planck Society during my thesis.

Much of this work would not have been possible outside of this thriving environment with so many experts sitting just next door. A special thanks to the department head Helmut Grubmüller for providing this infrastructure and the other members of the department especially, Jan-Henning Peters, Max Linke, Béla Voß, Rodolfo Briones, Christian Blau, Colin Smith, Maximilian Vossel, Daniel Seeliger, Timo Graen, Andreas Russek, Reinhard Klement, Andrea Vaiana, Lars Bock, Camilo Aponte, Vytas Gapsys, Hadas Leonov, Shreyas Kaptan and Nicholas Leioatts for helpful discussions.

I want to thank Maria Loidolt and Susanne Mükusch for their advice and sup-



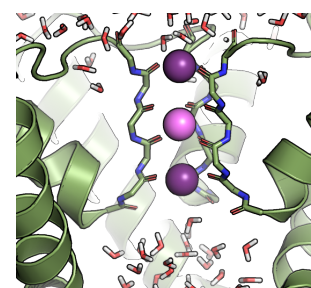
port. From my studies of biophysics in Kaiserslautern, I want to thank my professors Rolf Diller and Herbert Urbassek and my colleagues Beate Moeser, Viktoria Wollrab, Lin Jie, Marina Flöser, Sven Essert, Mariane Bader, Bernd Krolla and Volker Kegel for good times with many hours of intense studies. Furthermore, I also want to thank my physics teacher Klaus Ritzert and my biology teacher Jürgen Mang for their inspiring lectures and my classmates Rudolf Mitsch, Simon Metzendorf and Andreas Krugmann for their fun and friendly competition during physics classes that inspired all of us into perusing a career of physics.

Outside the scientific world, I am grateful to my parents who gave me the freedom and encouragement to pursue my interests and believed in me despite my initial shortcomings in school. Similarly I want to thank my sister Anna and brother Jonas for their support, and especially my brothers' design of the front page of this thesis. I want to thank my children Elisabeth and Viktoria for sacrificing many hours of playground time with their dad in the process of writing this thesis. Finally, with all my heart, I want to thank my wife Maren for her enduring support, her selfless sacrifices and her unceasing optimism even through the most troubled times—I could not have done it without you.



# Contents

<b>1</b>	<b>Introduction</b>	<b>12</b>
1.1	Diversity of K <sup>+</sup> channels . . . . .	13
1.1.1	Classification and nomenclature . . . . .	13
1.1.2	K <sup>+</sup> channels of interest . . . . .	13
1.2	Morphology of K <sup>+</sup> channels . . . . .	15
1.3	Physiology of K <sup>+</sup> channels . . . . .	17
1.3.1	Fast permeation and high specificity—the selectivity filter . .	17
1.3.2	Gating and C-type Inactivation—Modulating the Channel Conductance . . . . .	18
1.4	Pathology and pharmacology of K <sup>+</sup> channels . . . . .	21
<b>2</b>	<b>Aim and Organization of the Thesis</b>	<b>22</b>
<b>3</b>	<b>Theory</b>	<b>24</b>
3.1	Molecular dynamics simulations . . . . .	24
3.1.1	Integration and time step . . . . .	24
3.1.2	Force fields . . . . .	25
3.1.3	Cutoffs and long ranged electrostatics . . . . .	26
3.1.4	Periodic boundary conditions . . . . .	27
3.1.5	Thermostat and barostat . . . . .	27
3.1.6	Limitations of MD simulations . . . . .	27
3.2	Computational Electrophysiology . . . . .	29
3.2.1	Parallel and anti-parallel setup . . . . .	32
3.2.2	Electroporation . . . . .	33
<b>4</b>	<b>Inactivation in hERG</b>	<b>34</b>
4.1	Own contribution . . . . .	34
4.2	Abstract . . . . .	34
4.3	Introduction . . . . .	35
4.4	Methods . . . . .	37
4.4.1	Molecular dynamics simulations and docking . . . . .	37

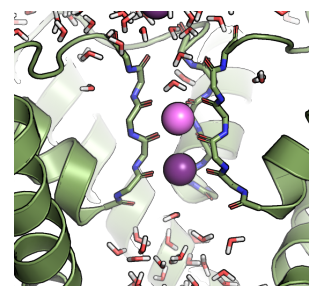


---

4.4.2	In vitro transcription and functional expression in <i>Xenopus laevis</i> oocytes . . . . .	38
4.4.3	Electrophysiological recordings . . . . .	38
4.4.4	Experimental data analysis . . . . .	38
4.5	Results . . . . .	39
4.5.1	Tightening of a hydrogen bond induces collapse of the hERG selectivity filter . . . . .	39
4.5.2	Alternating conformations of N629 act as switch for the selectivity filter . . . . .	43
4.5.3	Experimental evidence for the role of N629 and a neighboring H-bond network . . . . .	45
4.5.4	Structural links to modulation of cavity shape and effect of hERG agonists . . . . .	49
4.6	Discussion . . . . .	50
4.7	Acknowledgments . . . . .	52
<b>5</b>	<b>Direct Coulomb Knock-On</b>	<b>53</b>
5.1	Own contribution . . . . .	53
5.2	One sentence summary . . . . .	53
5.3	Abstract . . . . .	53
5.4	Introduction . . . . .	54
5.5	Materials and methods . . . . .	57
5.5.1	Molecular dynamics simulations . . . . .	57
5.5.2	X-ray crystallography analysis . . . . .	61
5.5.3	Brownian dynamics simulations . . . . .	64
5.6	Results and discussion . . . . .	65
5.7	Conclusion . . . . .	71
5.8	Acknowledgments . . . . .	74
<b>6</b>	<b>Flexibility of the Selectivity Filter</b>	<b>75</b>
6.1	Introduction . . . . .	75
6.2	Methods . . . . .	77
6.2.1	Simulation setup . . . . .	77
6.2.2	Restraining the flexibility . . . . .	77
6.2.3	Determining the electrical properties from the MD simulation . . . . .	78
6.3	Results and discussion . . . . .	78
6.3.1	SF flexibility during spontaneous ion permeations . . . . .	78
6.3.2	Effects of artificially restraining the SF flexibility . . . . .	82
6.4	Conclusions . . . . .	86

---

<b>7</b>	<b>Selectivity of KcsA</b>	<b>87</b>
7.1	Introduction . . . . .	87
7.2	Methods . . . . .	89
7.3	Results and discussion . . . . .	90
7.3.1	Impact of Na <sup>+</sup> on the current . . . . .	90
7.3.2	Ion specificity at the entrance to the SF . . . . .	91
7.3.3	Density profiles of the SF . . . . .	95
7.4	Conclusion . . . . .	97
<b>8</b>	<b>Coupling between Inactivation and Gating</b>	<b>99</b>
8.1	Introduction . . . . .	99
8.2	Methods . . . . .	101
8.3	Results and discussion . . . . .	102
8.3.1	Link between inactivation and gating . . . . .	103
8.3.2	Mechanism of the inactivation process . . . . .	105
8.4	Conclusions . . . . .	105
<b>9</b>	<b>Summary and Conclusions</b>	<b>106</b>
9.1	Ion permeation through the SF . . . . .	106
9.2	Changes of the SF structure . . . . .	107
<b>10</b>	<b>Outlook</b>	<b>109</b>
<b>11</b>	<b>Appendix</b>	<b>128</b>



# 1. Introduction

Potassium ( $K^+$ ) channels are proteins that allow the passage of  $K^+$  ions through the otherwise ion-impermeable membrane.  $K^+$  channels appeared at a very early stage in evolution and are today the largest, most diverse group of all ion channels, found throughout all kingdoms of life. They are estimated to be found in every living cell [1] where they are mostly involved in maintaining the cellular homeostasis such as intracellular salt concentration and the resting membrane potential [1–3]. These regulatory mechanisms are especially important for single cell organisms to quickly respond to environmental changes. In multi-cellular organisms they have become an integral part in inter cell communication and physiological responses: In plants they regulate osmotic pressures by which plants organize nutrient transports and directed motions [4,5]; in higher animals they are essential for nervous signal transduction [6].

Although the existence of  $K^+$  selective channels was postulated as early as 1902 [7], proof for their existence was established by the advances of electrophysiology [8,9] and the patch clamp [10] method. Many different types of  $K^+$  channels could be identified solely based on their characteristic response to electric stimuli or pharmacology [3,11–14]. Later, complementary information from DNA sequencing and targeted mutagenesis allowed to identify the genes of a large number of  $K^+$  channels and gave rise to the first crude structural models.  $K^+$  channel research experienced a big leap with the X-ray structure of the bacterial KcsA  $K^+$  channel by McKinnon and collaborators in 1998 [15] that lead to the Nobel prize in chemistry in 2003. This structure marks the starting point of a comprehensive structure based understanding of  $K^+$  channels. Since then many more crystal structures of  $K^+$  channels were resolved [16–18] and molecular dynamics (MD) simulations have added dynamics to these static pictures [19,19–21]. Still many of the key questions regarding the molecular basis of the voltage sensing mechanism, the extraordinarily fast ion permeation or the high  $K^+$  specificity remain topics with competing models and of lively discussions [15,22,23]. This introduction will therefore give an overview over the current state of  $K^+$  channel research followed by the aims of the presented thesis.

## 1.1 Diversity of K<sup>+</sup> channels

Today, a large variety of different K<sup>+</sup> channels have been identified throughout all kingdoms of life. For the fully sequenced model animals *Caenorhabditis elegans* and *Drosophila melanogaster*, 76 genes and 26 genes have been identified to encode for different K<sup>+</sup> channels, respectively. For mammals, a non exhaustive search has revealed 74 K<sup>+</sup> channel encoding genes [1,24]. Apart from the genes, K<sup>+</sup> channels have been shown to diversify via alternative splicing, hetero-dimerization among different channel types and by binding to different auxiliary proteins [24–28]. This enormous diversity allows a finely tuned electric response to a large variety of stimuli and is at the very basis of many complex signaling patterns [29].

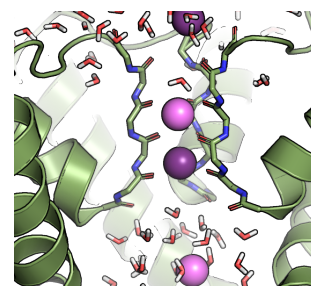
### 1.1.1 Classification and nomenclature

The first most coarse classification of K<sup>+</sup> channels is based on the number of transmembrane (TM) helices of the channel-forming monomer (see Fig. 1.1). Variants with 2TM, 4TM, 6TM, 7TM and 8TM have been described, of which the 6TM is the largest group followed by the 2TM, both of which form symmetric homotetrameric channels [13].

The next level of classification typically looks at the stimulus by which the channel alters its conductance. Most of the channels are sensitive to the transmembrane voltage, but there are ample examples for Ca<sup>2+</sup>, cyclic nucleotides, pH and even G-protein coupled K<sup>+</sup> channels [1,13,30]. The two largest and best characterized groups of vertebrate K<sup>+</sup> channels, the 6TM voltage-gated (K<sub>v</sub>) and the 2TM inward rectifier K<sub>ir</sub> channel family, are further characterized with a x.y nomenclature where x is the number of the subfamily and y the order of discovery. Hence K<sub>v</sub> 1.2 is the second discovered voltage-gated K<sup>+</sup> channel of subfamily one.

### 1.1.2 K<sup>+</sup> channels of interest

The K<sub>v</sub> family comprises a group of channels with 6TM helices, four of which form a voltage sensor that opens the channel shortly after a positive deviation from the normally negative membrane potential, a so called depolarization, has been applied [1,13,30]. Thus they are also referred to as "delayed rectifiers" and are the driving force for the rapid return to the resting potential after action potentials in excitable tissue. The difference between the individual members of this family lies in the time constants with which they open after depolarization and eventually close again. Due to their early electrophysiological characterization, many of these channels also have a common name:



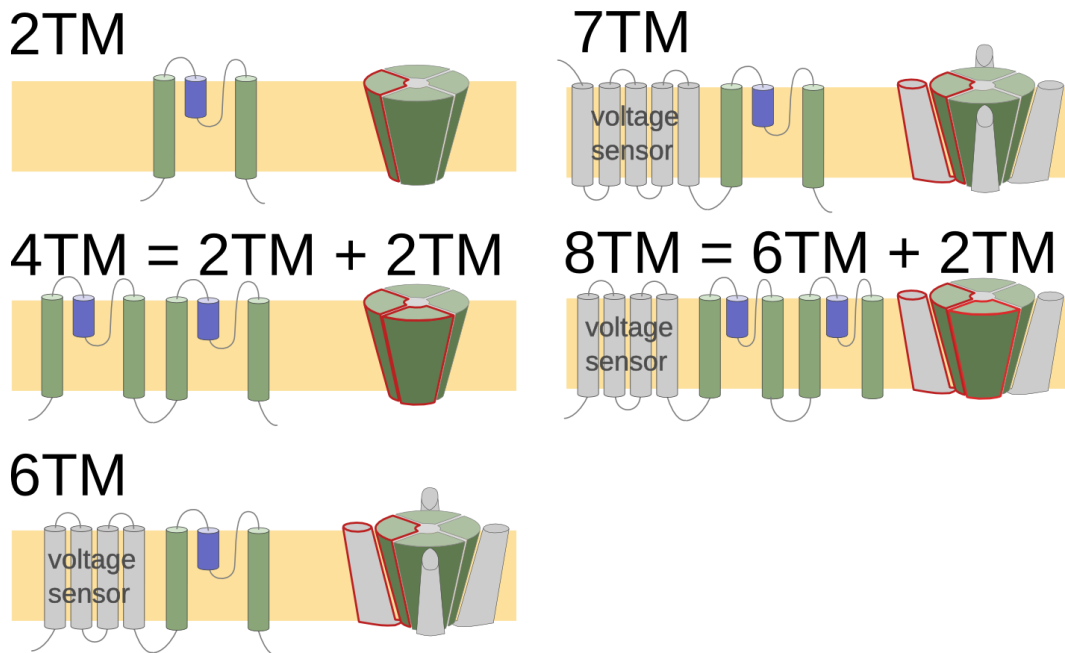


Figure 1.1: **Classification of ion channels by the number of trans-membrane helices (TM).** The left side of each panel depicts the helical arrangement embedded into the membrane (yellow) for each monomer. The pore-forming helices are shown in green, the selectivity filter spanning pore helix in blue and possible auxiliary helices forming e.g. voltage sensors are shown in gray. The right side of each panel shows the channel arrangement with the corresponding monomer as shown to the left highlighted in red.

$K_v$ 1.x	Shakers
$K_v$ 2.x	Shabs
$K_v$ 3.x	Shaws
$K_v$ 4.x	Shals
$K_v$ 11.1	hERG

Of this group three, structures have been solved using x-ray crystallographic techniques:  $K_v$  1.2 [17],  $K_v$  1.2- $K_v$  2.1 chimera [16], both from *Rattus norvegicus*, as well as the closely related bacterial  $K_v$  AP channel from *Aeropyrum pernix*, all three in presence of their voltage sensor.

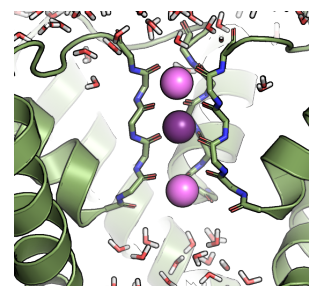
The second large group of voltage sensitive  $K^+$  channels is the "inward rectifier" family ( $K_{ir}$ ) with a 2TM architecture [1, 13, 30]. Contrary to the  $K_v$  family,  $K_{ir}$  channels are more conductive the more hyperpolarized—more negative than normal—the potential across the membrane is. Their role is best understood in cells with oscillating potentials as found in cardiac tissue. Here, they electrically stabilize the resting potential and prevent the depletion of the  $K^+$  gradient during

the prolonged cardiac action potential. Of this group, no mammalian structures have been resolved so far. However, two bacterial variants are available:  $K_{ir}$  Bac3.1 from *Magnetospirillum magnetotacticum* [31,32] and  $K_{ir}$  Bac1.1 from *Burkholderia pseudomallei* [33].

Two channels have especially shaped our understanding and can therefore be regarded as "model organisms" for  $K^+$  channels. Foremost KcsA, a pH sensitive channel from *Streptomyces lividans* was the first channel to have its structure solved using X-ray crystallography [15]. Although it is of bacterial origin, it has been shown to possess most of the electrophysiological features known from mammalian  $K^+$  channels [34]. Today about 10 other structures have been published revealing the structural effect of different salt concentrations, ion species and mutations, giving deep insight into the channel's molecular mechanism. The other channel is the archaic MthK from *Methanothermobacter thermautotrophicus*, a  $K^+$  channel sensitive to intracellular  $Ca^{2+}$ . It is currently the  $K^+$  channel structure with highest resolution at 1.45 Å [18] and it was the first channel crystallized in a conformation opened at the intracellular gate [35].

## 1.2 Morphology of $K^+$ channels

Despite their high physiological diversity, all  $K^+$  channels share a common structure, the so called pore domain [1,15,36]. This core element forms the actual ion pathway through the membrane and consists of an arrangement of four times three  $\alpha$ -helices in a fourfold rotationally symmetric arrangement around the ion permeation pathway (see Fig. 1.2). Two of these so called inner helices (S5 and S6 helix) span the entire membrane, whereas the so called pore helix (PH) lies in the cleft between the inner helices with its C-terminus tilted towards the center of the channel. From the central tips of the PHs spawns the core element of all  $K^+$  channels, the selectivity filter (SF)—a highly conserved structural motif (TxVGYG) which is also referred to as the "signal sequence" of  $K^+$  channels [36]. From the tips of the PHs these stretches of six amino acids extend towards the extracellular compartment forming a narrow cleft, lined by the backbone carbonyl-oxygen atoms (red in Fig. 1.2). These layers of backbone carbonyl moieties form the  $K^+$  binding sites  $S_0$  to  $S_4$  along the channel axis. This highly stretched conformation of the SF is stabilized by a wide ranging hydrogen bond network formed most prominently by the side chains of the PH, but also from the inner helices in this region. The most prominent of these supporting networks is an often found direct link between two residues directly behind the SF [36]. In KcsA this connection is formed by a pair of carboxylate moieties that share a common proton, another example is a bridge formed by a serine and an asparagine in the human hERG ( $K_v$  11.1) channel. Also most channels display a large agglomeration of aromatic



residues in the plane of the SF. This structure has been named the "hydrophobic cuff" and serves as a scaffold to stabilize the SF at its center [15]. The other half of the channel below the PH and SF is a wide water filled space, the cavity. This cavity can be occluded from the intracellular compartment by an aperture-like twisting and straightening motion of the inner helices in a process referred to as "gating" (see Fig. 1.3).

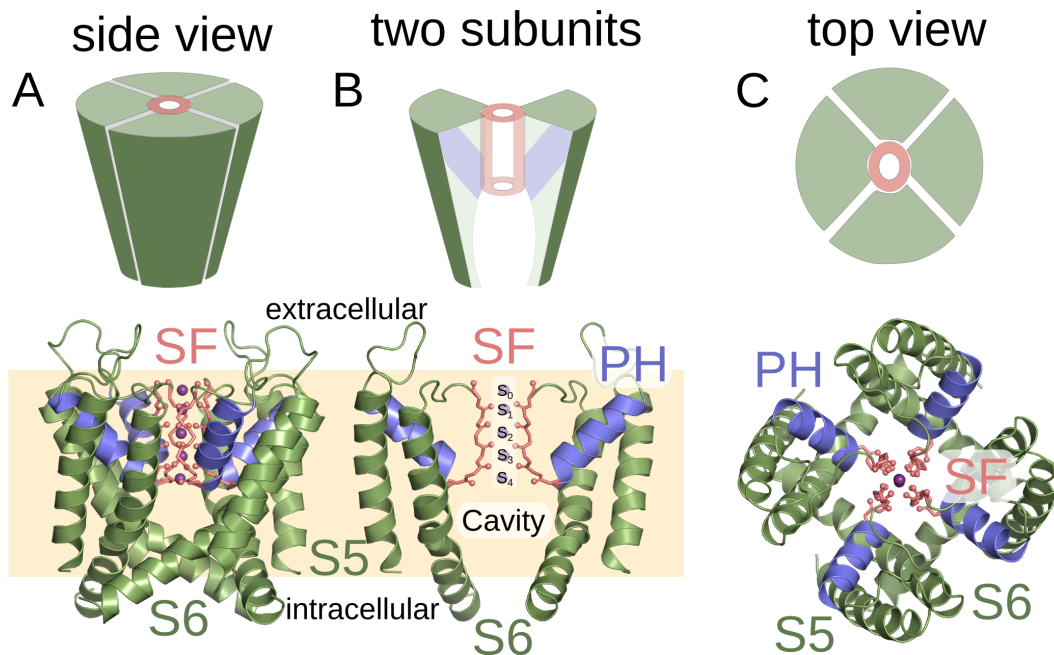


Figure 1.2: **Pore domain structure of  $K^+$  channels.** (A) Side view of the channel: The S5 and S6 helices (green) span the membrane (yellow). To the extracellular side the pore helices (PH, blue) form a scaffold for the selectivity filter (SF, red). (B) Two opposite monomers of the channel are shown, giving a plain view on the ion binding sites in the SF  $S_0$  to  $S_4$  and showing the water filled cavity towards the intracellular side. (C) Top view onto the channel from the extracellular side.

Besides the pore region, the channels diversify mainly by the N-terminal attachment to the inner helices. These attachments are known to bind the channels to the cytoskeleton, tuning their local concentration on the cell surface and predominantly determining the type of triggering signal. These triggering domains are directly connected to the tail of the inner helices and induce the opening and closing of the intracellular gate of the channel [1,24,37].



## 1.3 Physiology of $K^+$ channels

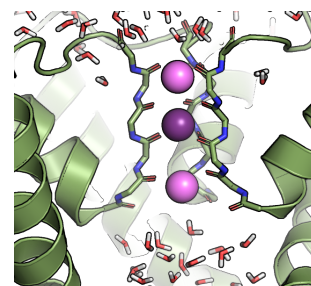
The physiological functions of ion channels can be broken down into two major parts: 1) They must conduct ions fast to reduce the number of channels needed and must be highly specific to their ionic species to avoid depletion of the ionic gradients constituted by other ion types. 2) They must be able to alter their conductance as a response to external stimuli, to assume their role in the complex electrical signaling of cells.

### 1.3.1 Fast permeation and high specificity—the selectivity filter

Since their discovery, one of the intriguing mysteries of  $K^+$  channels remains their high selectivity for  $K^+$  ions over other ions at a ratio of about 1000-100:1 while at the same time maintaining  $K^+$  currents close to the diffusion limit at rates on the order of  $10^8$  ions per second [34, 38, 39]. Based on crystal structures and mutagenesis studies these two core features—selectivity and fast transition—could be pinpointed to the SF [1, 13, 36].

The SF forms discrete ion binding sites along its axis in between the backbone carbonyl-layers, coordinating each bound ion between 8 oxygen atoms [22]. The  $K^+$  ions are not only the substrate of the  $K^+$  channel, they are also important structural elements that stabilize (and are stabilized by) the negative partial charge of the carbonyls. The actual permeation process is prompted by an arriving ion at one side of the SF. By binding to a site at either end of the SF, the already bound ions are pushed onwards, expelling the last ion on the other side into the bulk. This process of a new ion expelling an ion at the other side has been termed "knock-on" (despite the lack of transferred momentum) [15, 40]. Under equilibrium conditions, both directions will be equally likely and thus no net current will flow. However, by applying an electrical or chemical gradient across the membrane, one direction will be energetically favored, resulting in an ionic current. MD studies have calculated the energetic barrier of such a transition to be about  $10 \text{ kJ mol}^{-1}$ , which explains why the transition rate is fast compared with the timescales of ions diffusing to the channel [23, 41, 42].

Apart from the fast translocation rates,  $K^+$  channels are highly optimized for ion specificity. Even before crystallographic structures were available, it was shown that even conservative mutations in the SF would have adverse effects on the specificity [36, 43]. At first, it seems surprising that the larger  $K^+$  ions will easily traverse a narrow pore, whereas the smaller  $Na^+$  ions are unable to pass. Here two lines of theories offer explanations: The first postulates that the specificity of the SF for  $K^+$  ions should translate into a lower free binding energy for  $K^+$  as opposed to  $Na^+$  or other ions. Indeed, both MD as well as QM calculations support this hypothesis, but still competing theories of what exactly causes this difference in the



free energy of binding exist [23]. The first theories were based mainly on the exact geometry of the binding-sites [15], whereas other theories are centered around the number of coordinating ions or a subtle difference in rigidity of different filter regions as source of the binding free energy difference [22, 23]. The second line of arguments focuses on kinetics and postulates that the barriers of crossing the channel are much lower for  $K^+$  ions as compared to other ions. Such models have shown to elegantly model the phenomenon of the intracellular  $Na^+$  block of  $K^+$  channels—a known process by which intracellular  $Na^+$  acts as a voltage dependent blocker. Certainly, these two types of models are not mutually exclusive, they rather represent to different approaches to look at the same problem.

### 1.3.2 Gating and C-type Inactivation—Modulating the Channel Conductance

Most of what we know about the physiology of  $K^+$  channels goes back to electrophysiology. The development of the patch clamp technique alongside with high performance amplifiers allowed to monitor and manipulate ionic concentrations, current and voltage at the cellular and even down to the single channel level [44]. From the single channel measurements, we know that individual channels frequently switch between a conductive and a non-conductive state in a stochastic manner [1, 34]. This switching typically shows different rate constants and is oftentimes triggered by different types of external stimuli (see below). So with the discovery of these different rate constants, it was postulated that these channels possess more than one gate and thus more than one closed state. Through mutant channels and electrophysiology studies, three of such gates have been established: a conformational change at the SF called "C-type inactivation", the bundle crossing of the inner helices at the intracellular gate called "gating" and an autoinhibitory domain of the channel at the extracellular side referred to as "N-type inactivation" [28].

Gating is the most common electric regulatory mechanism in all  $K^+$  channels, opening and closing the channel as a response to external stimuli. It goes back to a structural rearrangement of the S6 helices straightening or bending sideways, to occlude or open the cavity from the bulk as shown in Fig. 1.3. The coupling to external stimuli is reflected structurally by a direct connection of the S5 helices to other specialized domains of the protein, acting as various sensors. A well studied example of such sensor domains is the voltage sensor of the  $K_v$  family where each of the subunits contributes a 4TM surrounding the pore domain, one of which carries an excess charge of  $+4e^-$ . This charged helix is subject to the strong electric fields inside the thin membrane and induces a conformational change that is relayed to the inner helices and close or open the channel accordingly [1, 15, 16,

20,28].

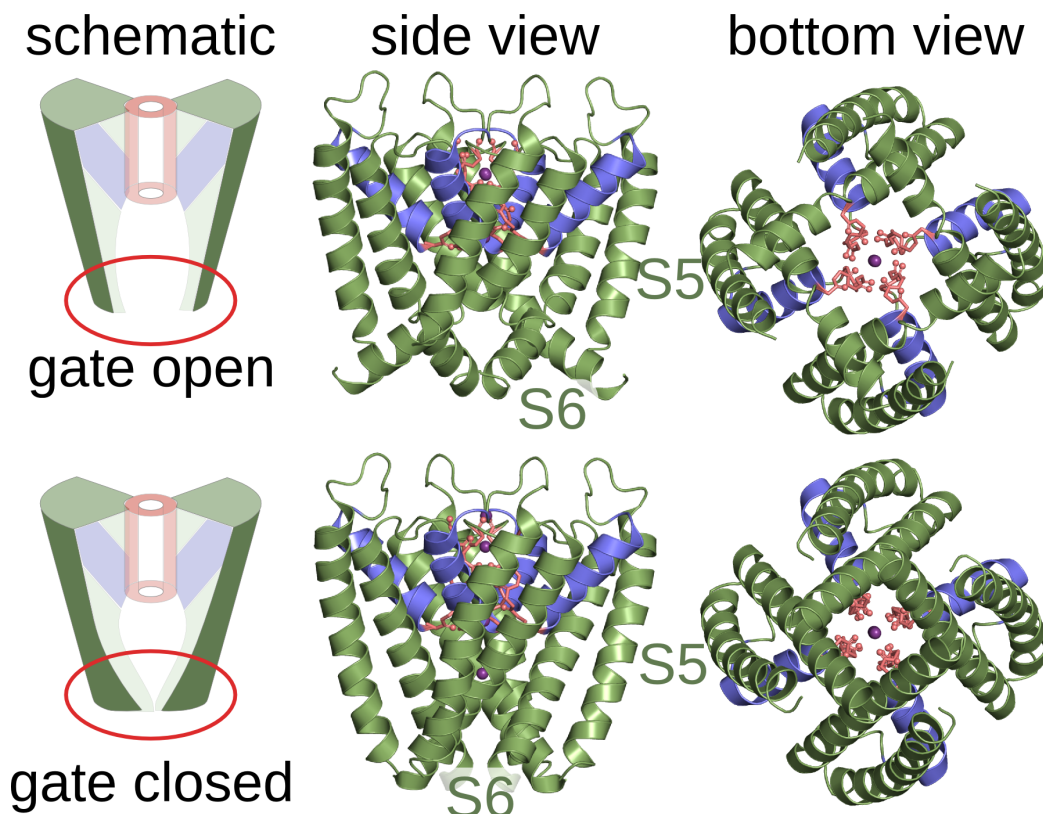
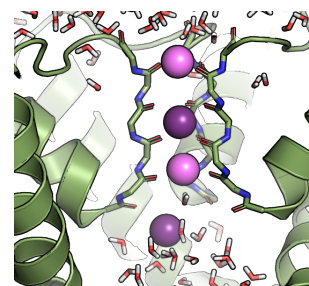


Figure 1.3: **Structural changes associated with the gating mechanism in  $K^+$  channels.** Top row: In the open state with the S6 helices tilted sideways, the water filled cavity is accessible from the bulk (PDB id: 3F5W [37]). Bottom row: Straightening of the S6 helices blocks access to the cavity and disrupts ion flow through the channel (PDB id: 3FB5 [37]).

The C-type inactivation usually closes the channel after prolonged opening times [28,31,37,45–47]. Typically, the C-type inactivation is slower than the gating, but there are counterexamples like  $K_v$  11.1 (hERG) which shows fast inactivation kinetics [48]. Structurally, inactivation goes back to a conformational change of the SF and is thought to resemble structures found under low  $K^+$  concentrations. Under these conditions, the SF adopts a "collapsed" conformation in which the SF structure tilt sideways and the central  $K^+$  binding sites are lost [49] (see Fig. 1.4). However, a recent study based on a synthetic  $K^+$  channel incapable of undergoing this collapsing transition, but still capable of inactivation, has stirred new discussions about the nature of the inactivated state [50]. C-type inactivation is extremely sensible to alterations of the hydrogen bond network around the SF;



even relatively conservative changes in this region tend to have a dramatic impact on the inactivation timescales or even completely eliminate the inactivated state [36,51]. The most famous example of such a non-inactivating channel is the E71A KcsA mutant, where the link of the proton sharing carbonic acids behind the SF is broken [52,53].

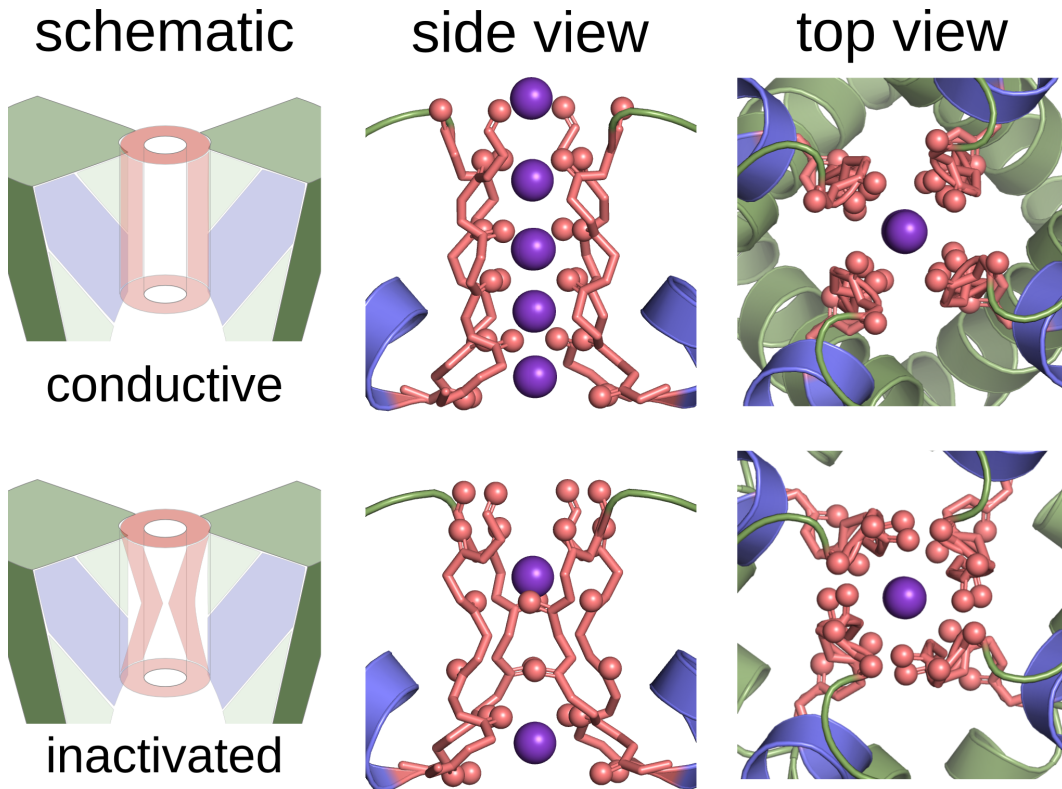
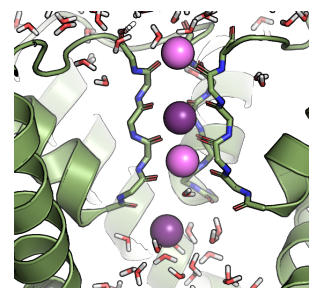


Figure 1.4: **Structural rearrangements of the SF attributed to inactivation.** Top row: structures recorded under high  $K^+$  concentration show neatly stacked carbonyl-oxygen atoms with equidistant  $K^+$  binding sites (PDB id: 3FB5 [37]). Bottom row: for structures recorded under low  $K^+$  concentrations the SF undergoes a distinct sideways tilt, compromising the central  $K^+$  binding sites (PDB id: 3F5W [37]).

Gating and C-type inactivation are not independent from each other, but have shown to open and close antagonistically. Typically, the channel will inactivate some time after the channel has been opened, and it will only recover from the inactivated state in a closed state. However, the mechanism by which these two gates are coupled remains elusive [37,45,46,53–55].

## 1.4 Pathology and pharmacology of K<sup>+</sup> channels

As K<sup>+</sup> currents are deeply involved in many regulatory pathways, it comes to no surprise that a malfunction of K<sup>+</sup> channels manifests itself in the form of various symptoms ranging from cardiac arrhythmia to diabetes and deafness [12, 56–59]. For such kinds of diseases that are based upon a channel malfunction, the term “Channelopathy” has been coined. By the same token the deep involvement renders K<sup>+</sup> channels to be promising drug targets for a wide range of applications such as auto immune diseases, multiple sclerosis, in the treatment of diabetes and even certain types of cancer [60–63]. Here, the difficulty often lies not so much in the search for a molecule that alters a targeted K<sup>+</sup> channel in the desired way but—in light of the omnipresence and similarity of K<sup>+</sup> channels in virtually all cells of the body—avoid unwanted interactions that would cause side effects. Even worse, some K<sup>+</sup> channels have proven to be promiscuous binders, even for drugs not targeting K<sup>+</sup> channels. A prominent example is K<sub>v</sub> 11.1 (hERG); it is highly involved in the cardiac action potential and its blockage can lead to cardiac arrhythmia and sudden death [48, 60]. Astemizole, an antihistamine, had to be retracted from the US and European markets in 1999 due to unintended interaction with hERG. To avoid such expensive cancellations at a late stage of the drug development, today, early electrophysiological screening against hERG interactions is routine procedure [64–66].



## 2. Aim and Organization of the Thesis

This thesis contributes to an atomistic understanding of the core element of all  $K^+$  channels: the selectivity filter (SF). After an introduction to the methods employed throughout this thesis in chapter 3, chapters 4 to 8 will present our findings from MD simulations of various  $K^+$  channel pore domains. In these simulations we will use the static structures from x-ray crystallography as a starting point. To validate our simulation results we will make use of electrophysiological data and complementary analysis from crystal structures to find a coherent mechanistic picture of the atomistic physiology of the SF. Chapter 9 will summarize what we have learned about the SF and will put our results into perspective. Finally, chapter 10 will show what future research based on this thesis we believe to be promising.

We will start in chapter 4 and address the question: How is the SF structure influenced by its surrounding hydrogen bond network? Comparisons between structures of different members of the  $K^+$  channel family and a series of single point mutations around the SF have shown that the intricate hydrogen bond network around the SF has a strong impact on the C-type inactivation kinetics [28, 36, 37]. Here, we will use MD simulations of the rapidly inactivating  $K^+$  channel hERG (human ether-à-gogo related gene) and systematically vary its hydrogen bond interactions behind the SF to probe the induced changes in the SF. We will then use our insights from these simulations to predict the behavior of several mutants, which were experimentally validated by our collaborators.

All subsequent chapters will build on the recently developed computational electrophysiology setup [67] by which ion permeation through various  $K^+$  channels can be simulated at voltages and ion concentrations close to the ones found in living cells.

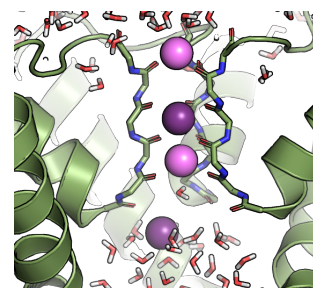
The main finding of this thesis will be described in chapter 5 and answers the question: What does the permeation process of  $K^+$  ions look like on an atomistic scale? In this chapter, we will first carefully validate the results by comparing observables such as current and ion occupancy at crystalline conditions as found in the simulations, to the corresponding experiments. We will then use the high spatial and temporal resolution of MD simulations for a detailed analysis of the typical ion permeation through the channel which we can compare to the es-

established “knock-on”-mechanism. Finally, we will propose a new model for ion permeation through the SF based on these findings.

Having established how the ions normally pass through the SF, we will focus on the question: How does the SF mediate the transition of ions? Here, we will take a closer look at the interactions between the binding-site-forming backbone carbonyl-oxygen layers over the course of spontaneous permeation events through the KcsA  $K^+$  channel. We will also test the implications of the “snug fit”-hypothesis, which states that the  $K^+$  channel physiology is based upon  $K^+$  ions moving through ideally formed binding sites tailored to accommodate  $K^+$  ions but not the smaller  $Na^+$  ions. This hypothesis entails very rigid binding sites as the difference in radius of  $K^+$  and  $Na^+$  is on the sub-Ångström scale. We will therefore artificially restrict the SF-flexibility in MD simulations and monitor the impact on the current.

Chapters 7 and 8 will present preliminary data with a promising outlook. In chapter 7 we will address one of the core questions of  $K^+$  channels: How do  $K^+$  channels discriminate between the bigger  $K^+$  and the smaller  $Na^+$  ions? This question is as old as the discovery of  $K^+$  channels themselves where competing theories have emerged: some focusing on thermodynamic arguments, others based on kinetic considerations. Using the computational electrophysiology setup for the KcsA  $K^+$  channel and adding  $Na^+$  ions we will test if the simulations are capable of reproducing the experimentally observed ion specificity. The results will be viewed in light of a recently proposed kinetic model and we will also test how the free energy-landscapes derived from Boltzmann-inversion of the simulated ion densities compare to previous free-energy calculations obtained by other methods.

In chapter 8 we will broaden our view from the SF to the whole pore region of the KcsA  $K^+$  channel and focus on the  $K^+$  channel’s ability to regulate its current as a response to external stimuli. From electrophysiological measurements, several mechanisms by which the channel can disrupt the ion flux are known [1,28]. Electrophysiology and a series of crystal structures have established that in particular two of these mechanisms are directly coupled: gating—a rearrangement of the helices at the intracellular mouth—and C-type inactivation originating from rearrangements of the SF [37,45,54]. To find a mechanistic link, we will compare our simulations of the wild type (WT) KcsA to simulations of the non-inactivating E71A mutant. To systematically assess the difference between these two ensembles, we will use the recently developed functional mode analysis [68].



## 3. Theory

### 3.1 Molecular dynamics simulations

Molecular dynamics (MD) simulation is a computational method to study the dynamics of proteins or other biomolecules at the atomistic level. There are several textbooks about this method [69–71] as well as comprehensive reviews [72–74]. The core idea of this method is to treat the atoms as classical entities whose dynamics can be described by integrating Newton’s equations of motion.

$$m_i \frac{\partial \vec{r}_i}{\partial t^2} = \vec{F}_i, \quad i = 1, \dots, N \quad (3.1)$$

With  $m_i$ ,  $\vec{r}_i$  and  $F_i$  being the mass position and force of the  $N$  individual particles. The crucial and computationally expensive task lies in the calculation of the forces acting on the atoms. These are derived from empirical energy functions which model the interactions between the particles. A consistent set of such energy functions capable of describing the interactions between all atoms is called a force field.

$$F = -\nabla V_{forcefield}(\vec{r}_1, \vec{r}_2, \dots, \vec{r}_N) \quad (3.2)$$

Trajectories are obtained by repeatedly calculating the forces for the current atom configuration and then numerically solving Newton’s equations with a sufficiently small time step to propagate the system. The following sections will give a more detailed description of the integration, the force fields and their approximations and will finally look at the limitations of the method.

#### 3.1.1 Integration and time step

There are multiple ways to numerically integrate Newton’s equations of motion (equation 3.1). Throughout this thesis the “leap frog” algorithm implemented in the GROMACS software was used. It calculates the velocities for the time in between the evaluation of the forces and positions. One could therefore think of



the velocity calculations “leaping over” the position calculations and vice versa, hence the name “leap frog”.

$$\vec{v}_{t+\frac{\Delta t}{2}} = \vec{v}_{t-\frac{\Delta t}{2}} + \frac{\vec{F}_t}{m} \Delta t \quad (3.3)$$

$$\vec{r}_{t+\Delta t} = \vec{r}_t + \vec{v}_{t+\frac{\Delta t}{2}} \Delta t \quad (3.4)$$

The numerical error associated with a finite time step  $\Delta t$  becomes large as soon as it reaches the order of magnitude of the smallest vibrations in the system, as these vibrations can no longer be sampled correctly. The fastest vibrations of the system therefore limit the integration time step. For biomolecules these smallest vibrations are typically associated with the bond stretching of the light hydrogen atoms limiting the time step to about 1 fs. By constraining these bonds to fixed length the time step can be doubled to 2 fs. These constraints can be justified because these high frequency bond vibrations are rarely excited at ambient temperature. By further constraining the angular vibrations of the hydrogen atoms the time step can be doubled again allowing for a 4 fs integration time step [75–77].

### 3.1.2 Force fields

The force fields comprise a set of empirical potential functions which model the interactions between the particles. They typically include simple potential functions to describe the non specific interactions—Coulomb and van der Waals (vdW)—and functions modeling the properties of chemical bonds such as bond lengths, angles and dihedral angles. The forces for a given atomic arrangement is accordingly calculated as the vector sum of the individual contributions.

$$\vec{F} = -\nabla V_{force\ field}(\vec{r}_1, \vec{r}_2, \dots, \vec{r}_N) \quad (3.5)$$

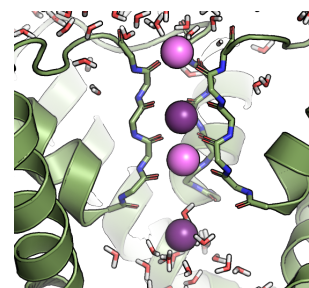
$$= -\nabla (V_{bonds} + V_{angles} + V_{dihedrals} + V_{improper} + V_{coulomb} + V_{vdW}) \quad (3.6)$$

where the bonds, angles and improper dihedral angles are typically modeled as harmonic functions,

$$V_{bonds} = \sum_{bonds} \frac{k}{2} (l - l_0)^2 \text{ (or constant, as written above)} \quad (3.7)$$

$$V_{angles} = \sum_{angles} \frac{f}{2} (\phi - \phi_0)^2 \quad (3.8)$$

$$V_{improper} = \sum_{imp\ dihedrals} \kappa (\xi - \xi_0)^2 \quad (3.9)$$



the proper dihedral angles as cosine functions,

$$V_{dihedrals} = \sum_{dihedrals} \frac{V}{2} [1 + \cos(\Phi - \Phi_0)] \quad (3.10)$$

and the non-bonded interactions are calculated using Coulomb's law for the electrostatic interactions and the Lennard-Jones potential for the vdW interactions and Pauli repulsion:

$$V_{coulomb} = \sum_{pairs\ i,j} \frac{1}{4\pi\epsilon_0} \frac{q_i q_j}{|\vec{r}_{i,j}|} \quad (3.11)$$

$$V_{vdW} = \sum_{pairs\ i,j} 4\epsilon_{i,j} \left[ \left( \frac{\sigma_{ij}}{|\vec{r}_{i,j}|} \right)^{12} - \left( \frac{\sigma_{ij}}{|\vec{r}_{i,j}|} \right)^6 \right] \quad (3.12)$$

A force field can therefore be thought of as a list of parameters such Lennard-Jones parameters for every atom type and harmonic force constants for each possible pair of atom types. These parameters are fine tuned within a given force field to describe as closely as possible the true nature of the system dynamics. To obtain such a consistent set of parameters two general approaches are perused: "Ab initio" approaches base the parameters on forces obtained from quantum mechanical calculations. Prominent members of this approach are the amber [78] and CHARMM [79] force field. The opposing strategy, as pursued by GROMOS [80] and OPLS-AA [81], optimizes the force field parameters to reproduce thermodynamic properties such as phase transitions and/or solvation free energies.

### 3.1.3 Cutoffs and long ranged electrostatics

By far the computationally most expensive step of an MD simulation is the force calculation for each atom. Especially the non bonded interactions—electrostatic and van der Waals—are expensive as there is an interaction of every atom with every other atom which computationally is on the order of  $N^2$ . As the vdW interactions decay with the distance as  $r^{-6}$ , the contribution to the force of far away atoms can be neglected. Thus through the use of neighbor lists, which keep track of closely spaced atoms and a cutoff that is typically around 1 nm, the vdW interactions can be calculated as an order  $N$  problem.

This strategy of cutoffs fails for electrostatic interactions as their decay with the distance ( $r^{-1}$ ) is much slower. Solely using plain cutoffs as with the vdW interactions would produce severe artifacts [82], due to the significant force-contribution of far reaching interactions. To cope with these long ranged interactions the particle-mesh Ewald (PME) method was developed. It uses the quick convergence of summing the smooth long ranged part of the electrostatic potential in

Fourier-space and is able to reduce the computational effort from  $N^2$  to the order of  $N \log(N)$  [83].

### 3.1.4 Periodic boundary conditions

According to the Young–Laplace equation a water droplet ( $\gamma$  = surface tension) at the typical system sizes on the order of 10 of nm would give rise to an internal pressure of

$$\Delta P = \gamma_{water} \frac{2}{r_{droplet}} \quad (3.13)$$

$$= 0.072 \frac{N}{m} \frac{2}{10 \cdot 10^{-9} m} = 7.2 \cdot 10^6 \frac{N}{m^2} \approx 72 atm \quad (3.14)$$

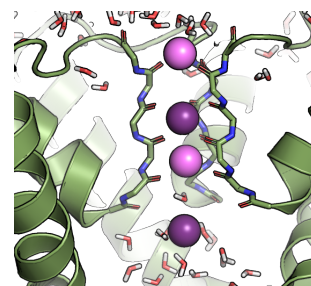
To avoid such extreme internal pressures, periodic boundary conditions are used. Under these conditions, the simulation system interacts with an infinite virtual crystal of systems around itself. Interactions of atoms at one side of the box are relayed to atoms on the opposite side of the box. In the same way atoms which leave the box on one side re-enter the box on the other side thus fully removing any surface. Of course these kinds of boundaries entail periodicity artifacts; however they are by far less severe than dealing with the extremely high pressures [84].

### 3.1.5 Thermostat and barostat

A system of a fixed size calculated with a perfect integrator would represent an ensemble with constant volume and constant energy (NVE). However, due to the accumulation of numerical errors in the integration process the total energy of the system (and with that the temperature) typically diverges over time. Additionally, simulations are most often compared to experimental results conducted under constant pressure and constant temperature (NPT). To reproduce these conditions in the simulations algorithms are used to regulate the system's temperature and pressure. Barostats calculate the pressure of the system using virials and linearly rescale the position of the particles to adapt the pressure to the desired value [85]. Analogously thermostats measure the temperature and rescale the velocities of all particles to obtain the desired temperature [86].

### 3.1.6 Limitations of MD simulations

The main limiting factor for MD simulations is computing power. For a given computing power, MD simulations have to compromise between a sufficiently accurate modeling of the physical interactions between the atoms while at the



same time producing enough sampling of the system's dynamics to reduce the statistical error. The more complex and thus more accurate the description of the force fields, the longer each iteration will take. This in turn will reduce the number of iterations for the same computer power and thus will decrease the sampling of the system's dynamics. Here I want to briefly sketch the nature of the errors connected with limited sampling and approximated physical interactions.

### Limitations in sampling

Theoretically many thermodynamic properties including entropies and free energies could be deduced from equilibrium simulations by simply binning and weighting of the states the system visits. In practice, however, MD simulations return a finite set of snapshots gathered over a finite time span which of course can only approximate the true equilibrium. It is surprisingly hard to determine how well a trajectory of given length already represents the equilibrium conditions. It is clear, however, that the more opportunity the system had to explore its phase space the better the trajectory is representative of the true equilibrium.

Insufficiently converged simulations will typically have a strong bias towards the starting conditions and will therefore overestimate its part in the actual equilibrium, opposed to states which have not been visited at all but which actually strongly contribute to the true equilibrium.

A widely practiced strategy to get an estimate for the convergence is to run multiple simulations of the same system and compare their sampling. How much sampling is in fact needed, strongly depends on the system in question. With current computing power, systems of 10 nm can be simulated on the order of 10  $\mu$ s within months. On these length and timescales interesting processes in small and medium sized proteins can be addressed. However, physiological processes taking place on the millisecond to second time scale and on lengths scales on the order of organelles to cells (e.g. action potentials or protein biosynthesis) are beyond the scope of today's standard MD simulations and require more advanced techniques.

### Limitations in modeling the physics

The most accurate simulations for molecular systems known today are quantum mechanical calculations. At their core they entail solving the time dependent Schrödinger equation which turns out to be computationally demanding despite a number of good and reliable approximations the field has developed. So even for systems with tens of atoms, nanoseconds are beyond their scope.

To reach longer timescales with larger systems, MD simulations treat all atoms as classical particles and empirically use the functions in the force field to approximate the effects which originate in quantum mechanics. E.g. the Lennard-Jones

potential approximates effects like Pauli-repulsion and the attractive London dispersion forces. Although these empirical force field functions have been carefully parametrized and successfully tested, there are certain caveats intrinsic to these approximations.

Practically breaking and formation of chemical bonds can not be modeled in classical MD simulations. This entails that chemical reactions like the protonation or the catalysis of enzymes can not be modeled in a straightforward way. Furthermore, current MD simulations neglect the effects of dynamic electronic polarization of molecules.

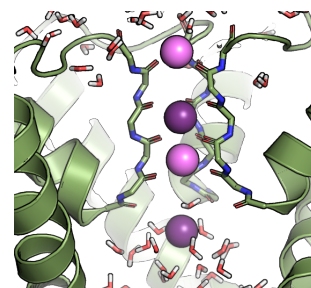
Apart from such intrinsic limitations, a frequently encountered critique of MD simulations raises doubts if the crude modeling of the force fields with its harmonic approximations is at all capable of describing the dynamics at the atomistic level. This fundamental critique is best addressed by close comparison to experimental results. There are ample examples of MD simulations not only reproducing experimental results but also predicting them. In the ideal case we find a fruitful collaboration between experiment and simulation, where experimental results back the validity of the simulation, and the simulation's deep insights into the atomistic mechanics help to understand the system giving rise to new hypothesis that can be experimentally validated.

## 3.2 Computational Electrophysiology

To assess the quality and predictability of MD simulations comparisons to experiments are invaluable. For ion channels the experiments with the deepest and richest insight into their physiology are electrophysiological measurements. These types of experiments examine the relationship between voltage and current for one channel (single channel recordings) or even all channels of a cell or vesicle (whole cell recordings). This relationship can be quite complicated as the measured currents and voltages strongly depend on time, concentration and types of involved ions and even other external stimuli, for example pH or pressure.

The Computational Electrophysiology method [67] was developed to closely match the conditions of single channel recordings in MD simulations. It is based upon a setup with two membrane-separated compartments as shown in Fig. 3.1A. Between these two compartments a charge imbalance can be created by placing a surplus of ions into one of the compartments while still maintaining an overall neutral system. This charge imbalance will in turn give rise to an electric field and therefore a voltage drop across both membranes as depicted in Fig. 3.1C.

This voltage will drive ions across ion channels embedded into either membrane, which would deplete the ionic gradient. The Computational Electrophysiology scheme maintains these gradients by swapping ions for a water molecules



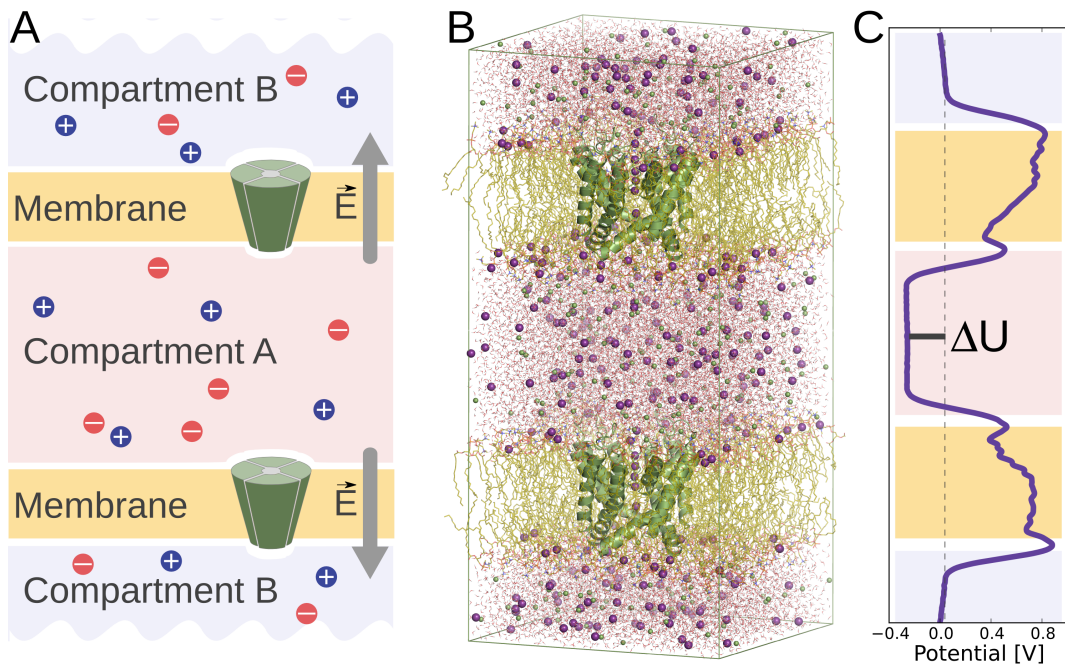


Figure 3.1: (A) Parallel setup for the Computational Electrophysiology scheme. Two separate membranes form two compartments respecting periodic boundary conditions. (B) Atomistic example of a such a system with a POPC membrane and two KcsA  $K^+$  channels embedded into each membrane. (C) The charge imbalance between these two compartments creates a voltage drop across the membranes.

after ion permeation events. These kind of simulations therefore do not sample an equilibrium but rather steady state conditions. Energy is constantly pumped into the system by the swapping of the ions against the electric gradient, however due to the thermostat this energy will be dissipated and will not accumulate in the system.

The current implementation of the Computational Electrophysiology scheme is used to keep the number of anions and cations constant for each compartment and thus, allowing only integer multiples of the elementary charge ( $e^-$ ) as differences. To get an estimate for the expected voltage at the typical system sizes, we must consider the following: as the overall system is required to be electrically neutral these integer differences amount to multiples of  $\Delta Q = 2e^-$ . At the typical MD system sizes  $L$  of about 10 nm and with a membrane thickness  $d$  of 4 nm and an estimated permittivity  $\epsilon_r$  of the membrane in the range of 10 (benzene  $\sim 2$ , propanol  $\sim 18$  [87]) we can estimate the minimal potential difference  $U_{min}$  to be:

$$U_{min} = \frac{\Delta Q \cdot d}{L^2 \cdot \epsilon_0 \epsilon_r} \quad (3.15)$$

$$= \frac{2 \cdot 1.60 \cdot 10^{-19} \text{C} \cdot 4 \text{nm}}{(10 \text{nm})^2 \cdot 8.85 \cdot 10^{-12} \text{C}^2 \text{J}^{-1} \text{m}^{-1} \cdot 10)} \quad (3.16)$$

$$= 0.223 \text{V} \approx 200 \text{mV} \quad (3.17)$$

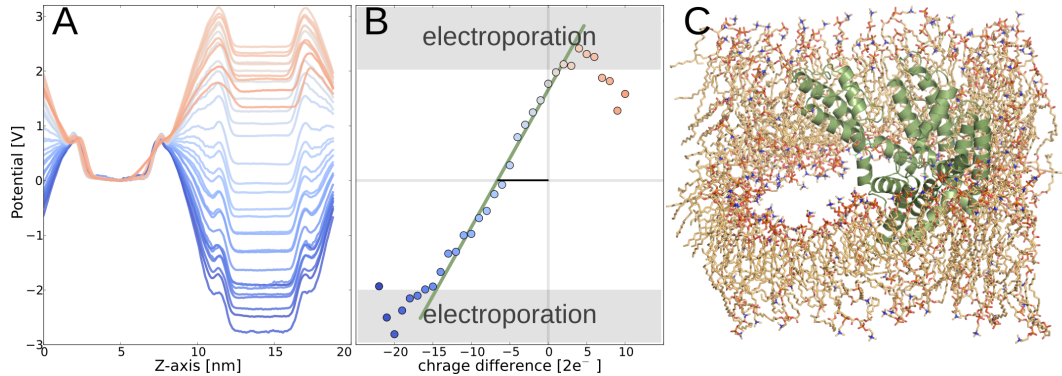
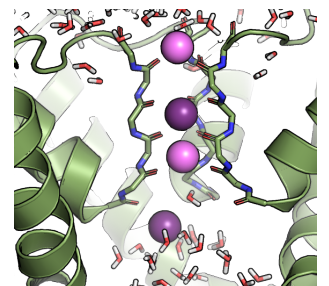


Figure 3.2: **(A)** Average potential along the Z-axis for varying charge differences (color code) from Computational Electrophysiology simulations of the anti-parallel double membrane system (25 ns each). Defining the lower bulk potential as zero (red area), one can observe how the potential in the upper bulk (blue area) changes with the charge imbalance. **(B)** The potential difference increases linearly with the charge imbalance. Due to the dipoles in the channel proteins, the anti-parallel configuration yields a potential offset, even when no ionic charge imbalance is imposed. Beyond a voltage of about 2 V the linear relation between charge imbalance and voltage breaks down. **(C)** In those cases we find spontaneous pore formation in the membrane and a subsequent collapse of the system.

Compared to the resting membrane potential of around -70 mV and the spikes of action potentials of around +40 mV this is already quite high. According to Eq. 3.15 this value could be lowered by increasing the membrane surface or decreasing the membrane thickness. As in most cases the membrane type will be determined by the experimental conditions only the size of the membrane remains to modify the electrical potential. This, however, comes with bigger systems and therefore longer simulation times or less sampling. Here a possibility might be to add multiple channels in each lipid bilayer and compensate the reduced sampling by an increase in sampling per channel. This strategy, however, comes with the risk of unwanted channel-channel-interactions.

In future implementations of the Computational Electrophysiology method this



problem will most likely be overcome by allowing the number of ions to be distributed between the compartments in non-integer values. The Computational Electrophysiology scheme will then swap ions to fulfill these fractions as a time average.

### 3.2.1 Parallel and anti-parallel setup

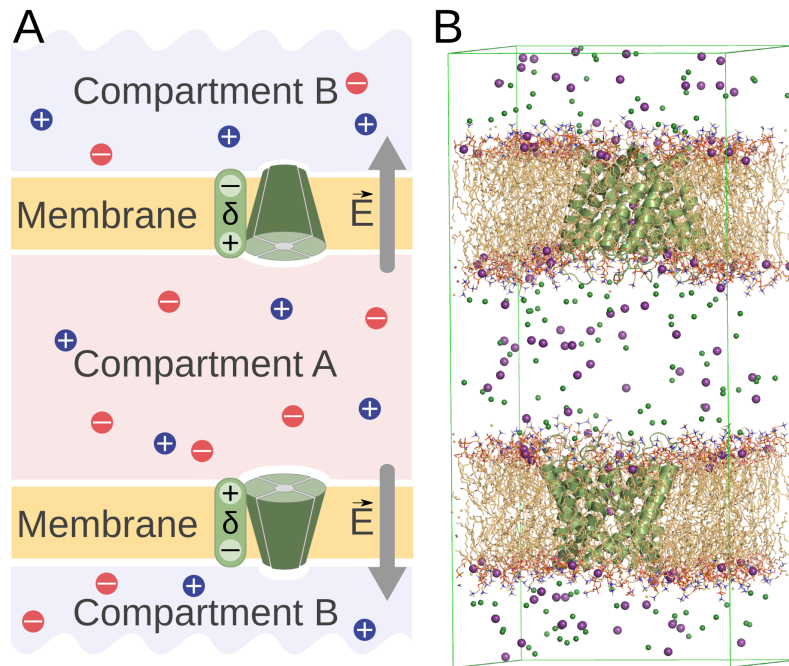


Figure 3.3: Anti-parallel setup for the Computational Electrophysiology scheme. With this configuration both channels can be sampled at the same voltage. It comes with the caveat of doubling the dipoles of the single system which will create an offset voltage (see below.)

The use of a double membrane system of course also doubles the system size which, for a given computing power, ideally gives only half the simulation time for the whole system. However, when we construct the system to include two channels—one in each membrane—the sampling per channel should be comparable to the single system.

In constructing these double membrane systems from single systems, two configurations are possible:

1. parallel configuration (Fig.3.1A,B): In this configuration the two compartments are per construction symmetric. Any dipoles from the membrane or

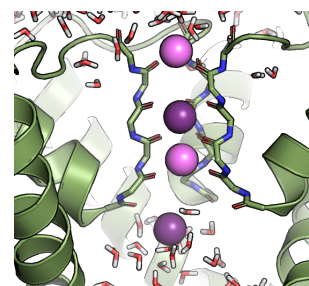


the channel will cancel out. As the electric field across the membranes is anti-parallel the channels will be subject to the same magnitude in voltage but of opposite sign.

2. anti-parallel configuration (Fig. 3.3A,B): In this configuration possible dipoles of the protein and the membrane are doubled and give rise to an offset voltage as shown in Fig. 3.2B. This offset voltage has to be compensated by an additional ionic imbalance between the compartments (see Fig. 3.2). Aside from these caveats, this configuration allows to sample both channels at the desired voltage.

### 3.2.2 Electroporation

As shown in Fig. 3.2B the linear relation between charge difference and voltage breaks down at around 2V. At these extremely high potentials ruptures of the membrane can be observed at the 10 ns timescale as shown in Fig. 3.2C. This might well correspond to the experimentally observed phenomenon of electroporation [88]. It has been shown that cells or vesicles subjected to high potential pulses become leaky and allow otherwise impermeable molecules to enter [88–90]. However, whether the experimental and the simulated electroporation describe the same phenomenon remains to be investigated.



## 4. A Molecular Switch Driving Inactivation in the Cardiac K<sup>+</sup> Channel hERG

This chapter has been published as **David A. Köpfer**, Ulrike Hahn, Iris Ohmert, Gert Vriend, Olaf Pongs, Bert L. de Groot, Ulrich Zachariae. A Molecular Switch Driving Inactivation in the Cardiac K<sup>+</sup> Channel hERG *PLoS ONE* 7(7): e41023 (2012); doi:10.1371/journal.pone.0041023

### 4.1 Own contribution

I performed all the MD simulations and their analysis. Interpretation of the data and writing of the paper was done in collaboration with Bert de Groot and Ulrich Zachariae.

### 4.2 Abstract

K<sup>+</sup> channels control trans-membrane action potentials by gating open or closed in response to external stimuli. Inactivation gating, involving a conformational change at the K<sup>+</sup> selectivity filter, has recently been recognized as a major K<sup>+</sup> channel regulatory mechanism. In the K<sup>+</sup> channel hERG, inactivation controls the length of the human cardiac action potential. Mutations impairing hERG inactivation cause life-threatening cardiac arrhythmia, which also occur as undesired side effects of drugs. In this paper, we report atomistic molecular dynamics simulations, complemented by mutational and electrophysiological studies, which suggest that the selectivity filter adopts a collapsed conformation in the inactivated state of hERG. The selectivity filter is gated by an intricate hydrogen bond network around residues S620 and N629. Mutations of this hydrogen bond network are shown to cause inactivation deficiency in electrophysiological measurements. In addition, drug-related conformational changes around the central cavity and pore helix provide a functional mechanism for newly discovered hERG activators.

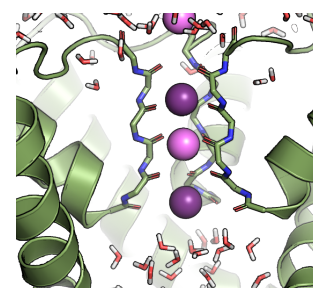
### 4.3 Introduction

Regulated current through  $K^+$  channels plays an essential role in cellular ionic homeostasis and intercellular signaling [1]. Although activation gating—a large-scale reconfiguration of the pore-forming trans-membrane helices—had long been viewed as the main regulatory switch of  $K^+$  channels, C-type inactivation and the coupling between activation and inactivation have recently been recognized as general control mechanisms of  $K^+$  channel gating [31,37,45–47]. There is increasing evidence that the inactivation gate of  $K^+$  channels resides near the  $K^+$  selectivity filter (SF), and that C-type inactivation entails a conformational change of the filter itself [37,45,46,53–55]. C-type inactivation plays a particularly important role in the  $K^+$  channel hERG (human ether-à-go-go related gene potassium channel,  $K_v$  11.1).

hERG is a channel protein predominantly expressed in human cardiac myocyte membranes [48,91]. It forms a pore at the interface of four subunits each containing six trans-membrane (TM) helices and the pore helix. The pore comprises the  $K^+$  selectivity filter (SF) and a central, water-filled cavity (Fig. 4.1A) [48], lined by the innermost TM helices S5 and S6. In addition to its cardiac function, hERG also appears to contribute to tumor cell proliferation and apoptosis [92]. In most  $K^+$  channels, C-type inactivation is a slow process that decreases channel current on time scales of seconds. In hERG, it proceeds much faster (0.7–2.9 ms) and thus dominates its conductance properties. As the repolarization phase of the human cardiac action potential is governed by flux through hERG, its kinetics determine the length of the action potential and, thereby, strongly contribute to normal function of the heart [48,93].

hERG malfunction is thus implicated in many forms of cardiac arrhythmia, which affect up to 1 in 5000 humans and are a common cause for sudden death [95–97]. The highest arrhythmic risk is associated with hERG mutations in the pore region which affect inactivation, and with undesired drug binding to hERG, again primarily affecting the inactivated form of the channel [98–103]. Long-QT syndrome is caused by loss of hERG function, either through misfolding, trafficking defects, or hERG missense mutations, while impairment of inactivation induces short-QT syndrome via gain of hERG function [104–107].

To understand inherited or acquired short- and long-QT syndrome, insights into the mechanistic basis for inactivation gating are essential. It has been suggested that the inactivated state of the hERG SF resembles the collapsed (low- $[K^+]$ ) configuration of the SF (as displayed by the crystal structure of KcsA; [49]), but this hypothesis awaits validation [103]. We used our recently developed consensus structure model of the hERG open state [94] to investigate the driving forces, nature, and consequences of the conformational change that leads to hERG



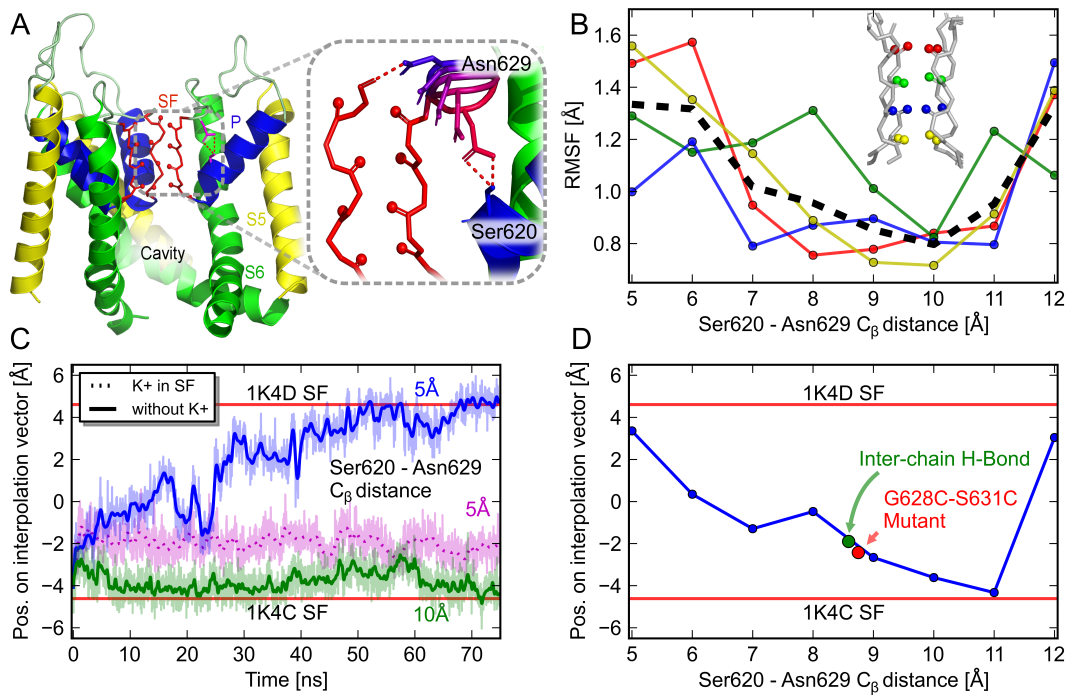


Figure 4.1: **Model structure of the hERG channel and switch behind the selectivity filter.**

(A) hERG channel, lined by the S6 helices (green), and including the K<sup>+</sup> selectivity filter (SF, red), pore helices (P, blue), internal cavity and outer pore loop. As structural information on the turret loops is sparse and modeling according to homology is not possible in this region, the loops were modeled as in KvAP [94]. (A, inset) Scan of H-bonds between either N629 and S620 or N629 and G628. (B) Dependence of the backbone carbonyl fluctuation (RMSF) of SF residues S624-F627 on the distance between S620 and N629. (C) Smaller separations between S620 and N629 (5 Å, blue curve) promote SF collapse (1K4D, upper red bar), while larger separations (10 Å, green curve) stabilize its conductive state (1K4C, lower red bar). (D) Direct dependence of the extent of SF collapse on the interaction between N629 and S620 (blue line). Formation of a stable inter-chain H-bond to G628 stabilizes the conductive SF (green). The non-inactivating mutation G628C/S631C precludes close contact between N629 and S620 and thus collapse (red)

inactivation. This model has recently been shown to quantitatively reproduce experimental hERG blocker structure-activity relationships [108]. Combinations of *in silico* molecular dynamics (MD) and docking studies with *in vitro* and *in vivo* mutagenesis and electrophysiology studies revealed the pathway of the conformational change at the SF and a distinct molecular switch that toggles the SF between conductive and collapsed states.

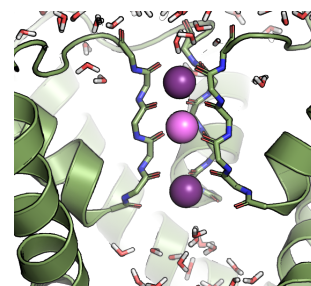
## 4.4 Methods

### 4.4.1 Molecular dynamics simulations and docking

All simulations were based on the recent consensus homology model of the pore-forming region of hERG, comprising helices S5 and S6, the pore helix, and the pore loop [94]. The hERG model was inserted into a simulation box with a fully hydrated and equilibrated membrane consisting of 176 dimyristoylphosphatidylcholine (DMPC) molecules and 12 888 water molecules using *g\_membed* [109]. The *amber99sb* force field was used for the protein and ions [78]; parameters for DMPC were derived from Berger et al. [110] and the solvent was modeled using the SPC/E water model [111].

All simulations were carried out with the Gromacs simulation software, version 4.0 [84]. Electrostatic interactions were calculated explicitly at a distance smaller than 1.0 nm, long-range electrostatic interactions were treated by particle-mesh Ewald summation at every step [83]. Lennard-Jones interactions were calculated using a cut-off of 1.0 nm. The LINCS algorithm was employed to constrain all bonds [76], allowing for an integration time step of 2 fs. The simulation temperature was kept constant by weakly ( $t = 0.1$  ps) coupling the lipids, protein and solvent separately to a temperature bath of 310 K by using the velocity-rescale method [86]. Likewise, the pressure was kept constant by Berendsen coupling of the system to a pressure bath of 1 bar [85]. To ensure a conductive conformation of the SF at the beginning of the simulations, the system was equilibrated for 1 ns with position restraints on the SF backbone atoms using the high-[K<sup>+</sup>] crystal structure of KcsA as reference (PDB entry 1K4C [49]) with a force constant of 1000 kJ mol<sup>-1</sup> nm<sup>-2</sup>. For the S620–N629 distance scan simulations, a distance restraint between the C<sub>β</sub> atoms of S620 and N629 was introduced by means of a harmonic potential with a force constant of 5000 kJ mol<sup>-1</sup> nm<sup>-2</sup>. In simulations of the collapsed SF, the low-[K<sup>+</sup>] conformation of the SF was used together with position restraints of 1000 kJ mol<sup>-1</sup> nm<sup>-2</sup>. After energy minimization and equilibration of the system using position restraints of the same strength on all protein heavy atoms for 2 ns, simulations of 50–100 ns length were carried out. The collective coordinate describing the transition between the high- and the low-[K<sup>+</sup>] crystal structures of the KcsA SF was obtained by performing a principal component analysis of the SF backbone on the set of PDB entries 1K4C and 1K4D [49]. To derive the data points shown in Fig. 4.1D, we used the average projection of each simulation on the difference vector after 40 ns.

Dockings of PD-118057 [104] and ICA-105574 [112] were performed using FlexX from LeadIT [113] with standard parameters. A degree of flexibility of protein side chains was introduced as derived from the simulations. The spatial extent of the



side-pocket was determined by calculating its solvent accessibility for molecules the size of water using in-house code. Independently, the accessibility of the pocket for PD-118057 and ICA-105574 molecules was investigated by using FlexX. The receptor surface was defined using a radius of 18 Å around S620 nearest to the side-pocket. The best scoring molecule docked in the side-pocket was selected for visual representation.

#### 4.4.2 In vitro transcription and functional expression in *Xenopus laevis* oocytes

mRNAs were prepared from hERG wild-type or mutant constructs (Y616F, F617Y and N629Q) in pGEMHE using the mMACHINE T7 kit (Ambion) according to the manufacturer's instructions. Oocyte incubation and cRNA injections were performed as described previously [114]. Briefly, 1 day after surgery, oocytes were injected with cRNA ( $1-2 \mu\text{g} \mu\text{l}^{-1}$ ). Functional expression was typically assessed 1-3 days after microinjection. Inward current levels were in the range of 1-10  $\mu\text{A}$  at repolarizing voltages of -100 mV to ensure proper voltage control.

#### 4.4.3 Electrophysiological recordings

Whole-cell currents were recorded under two-electrode voltage control using an Oocyte-clamp amplifier (Oc-725C Oocyte-clamp, Warner Instrument Corp., USA). Glass microelectrodes (World Precision Instruments, Sarasota, FL, USA) were pulled (DMZ Universal puller, Zeitz Instruments, Martinsried, Germany), and their tips were bevelled (Micro forge, Narishige Co. LTD, Tokyo, Japan) to obtain resistances between 0.1-2 M $\Omega$ . The pipettes were filled with 3M KCl and the oocytes were superfused with ND96 solution: (in mM) KCl 2, NaCl 96, CaCl<sub>2</sub> 1, MgCl<sub>2</sub> 1, HEPES 5, pH 7.4 (adjusted with 1 N NaOH). All currents were digitally sampled at 2 kHz and leak and capacitive currents were corrected on-line using the P/4 subtraction method. The sweep interval was 25 s and the holding potential was -100 mV. Data were converted with an AD/DA-computer interface (TIC16, Instrutech Corporation, Great Neck, USA) and stored on a personal computer. All experiments were performed at room temperature (20-23 °C). The program packages Pulse+Pulsefit (HEKA Elektronik, Lambrecht, Germany) and IGOR Pro (WaveMetrics Inc., Oregon, USA) were used for data acquisition and analysis.

#### 4.4.4 Experimental data analysis

The voltage dependence of activation was assessed by standard tail current analysis using repolarizing pulses to -140 mV. Tail current amplitudes were normalized

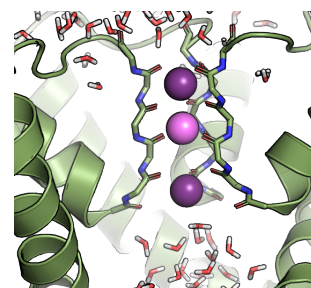
to maximum. A Boltzmann function  $I_{tail}/I_{max} = 1 + 1/(1 + (\exp(V_{1/2} - V)/k))$  was fit to the data to estimate  $V_{1/2}$  and the rate constant  $k$ , where  $V_{1/2}$  is the potential at half-maximal current activation and  $k$  the slope factor. A single exponential function was fit to the deactivating currents to using Pulsefit software. Steady-state inactivation was determined essentially as described by Zhang et al. [115]. The ratio of instantaneous current amplitude and amplitude of current remaining after 100ms was taken as measure of steady-state inactivation at a given test potential. The voltage of half-maximal steady-state inactivation ( $V_{1/2,inact}$ ) was calculated by fitting a Boltzmann function to the data. To obtain an estimate of  $V_{1/2,inact}$  for F617Y hERG channels, we used an open fit procedure with the assumption that the mutation did not alter the slope of the steady-state inactivation–voltage relation. Data are given as mean  $\pm$  S.E.M.

## 4.5 Results

### 4.5.1 Tightening of a hydrogen bond induces collapse of the hERG selectivity filter

Crystal structural and electrophysiological studies on KcsA have indicated that hydrogen bonding between residues E71 and D80 behind the SF affects C-type inactivation in this prokaryotic  $K^+$  channel [53,55]. Inactivation is thought to involve conformational changes within a network of residues encompassing the SF as highly conserved structural element [116]. Many mutations that affect hERG inactivation scatter around the homologous hERG sequence positions S620 and N629 as central residues [99]. According to most present hERG structural models, these residues are arranged behind the fully conserved hERG SF [117–119], however without a close and direct interaction in most cases [118,119]. On the basis of our recent consensus structural model [94], we carried out a computational interaction scan, in which the distance between the side chains of S620 and N629 was systematically varied in intervals of 1 Å (Fig. 4.1A). We then monitored the response of the inner SF, i.e. the backbone region between residues S624 and G627, in extensive MD simulations. The most pronounced level of conformational variability was observed in simulations with a transiently vacated SF. To distinguish protein-mechanistic from ion-induced effects, we repeated the simulations with varying ion occupancy in the SF (Fig. 4.3).

As shown in Fig. 4.1, the configuration of S620 and N629 markedly influenced the dynamics of the SF. The root mean square fluctuation (RMSF) of the carbonyl-oxygen atoms that coordinate  $K^+$  ions at the binding sites  $S_1$ – $S_4$  [49] was minimal when the distance between S620  $C_\beta$  and N629  $C_\beta$  remained close to 10 Å (Fig. 4.1B). Especially the fluctuation of the terminal groups of oxygen atoms in the SF (S624



and F627) was modulated by up to a factor of 2 by the distance between S620 and N629. The average fluctuation levels varied between  $\sim 0.8$  Å and 1.6 Å, depending on their separation. At distances larger than  $d = 11$  Å, a sharp increase in fluctuation was seen owing to stretching of the SF backbone.

To investigate the structural consequences of such increased flexibility, we examined hERG configurations with minimum and maximum fluctuation levels. The obtained SF conformations were then compared to high-resolution crystallographic data. We chose the highest-resolution structures of the KcsA SF backbone in their high-[K<sup>+</sup>] (conductive, PDB ID 1K4C; [49]) and low-[K<sup>+</sup>] (collapsed, PDB ID 1K4D; [49]) configurations as comparison, and used the projection of the SF configurations on the difference vector between these extreme geometries as reaction coordinate.

Fig. 4.1C shows that a conformational change from the conductive (1K4C) to a collapsed SF state (1K4D, horizontal red bars) was elicited when the interaction distance between S620 and N629 was closest ( $d_{S-N} = 5$  Å, measured between the respective  $C_\beta$  atoms in four independent simulations, compatible with an intact H-bond, blue curve). The conformational change occurred on a time scale of  $\sim 40$  ns. In sharp contrast, a wider S620–N629 separation ( $d_{S-N} = 10$  Å) stabilized the highly ordered, conductive state of the SF (Fig. 4.1C, green curve), even without the presence of ions in the filter. For comparison, in KcsA, collapse of the SF to its low-[K<sup>+</sup>] state has recently been identified as the most likely cause of slow inactivation [37,45,46]. In addition, hydrogen bonding between the residues homologous to S620 and N629 in KcsA, E71 and D80, has been shown to directly influence entry into the C-type inactivated state of KcsA [53,55]. It has been debated whether the mechanism of hERG inactivation may be fundamentally different from other K<sup>+</sup> channels, in particular from slow inactivation in KcsA [116]. For instance, there are major differences in the response to extracellular tetraethylammonium and K<sup>+</sup> concentration. However, recent mechanistic insights gained by mutation studies and simulations point toward many common mechanistic features shared by SF inactivation in the pore domain of most K<sup>+</sup> channels, including KcsA and hERG [37,116].

Fig. 4.2 displays a direct view of the SF observed in the two extremes of the distance scan with water molecules present at that particular time frame, together with a comparison to KcsA SF crystal structures. Please note that the transient presence of water does not imply stable binding sites. At the end of the  $d_{S-N} = 10$  Å simulation, the SF backbone (Fig. 4.2B) had remained close to the configuration of the high K<sup>+</sup> state (1K4C, Fig. 4.2D). This is remarkable, as K<sup>+</sup> ions were not bound to the SF and the fluctuation level at the simulation temperature was relatively high. The only exception are transiently flipped carbonyl groups at V625, as previously reported (see below). By contrast, a distance  $d_{S-N}$  of 5 Å resulted in fil-



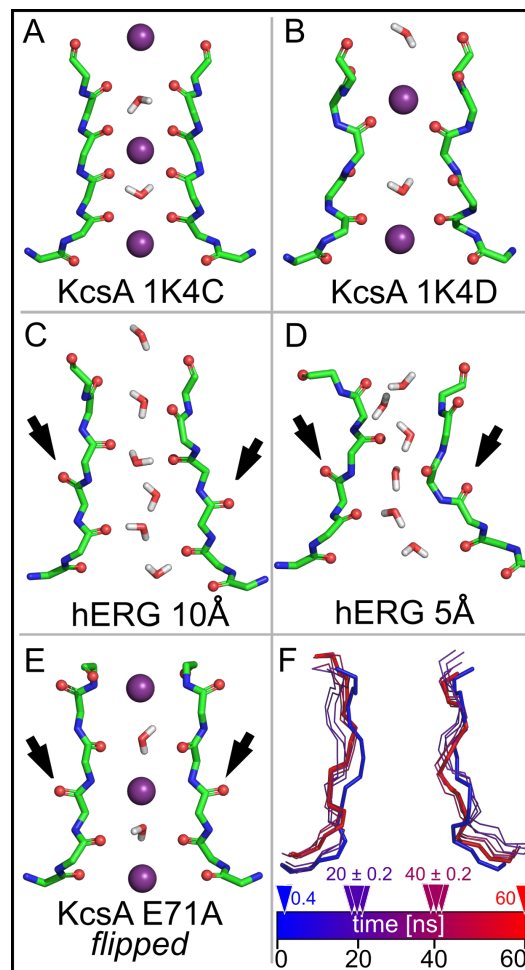
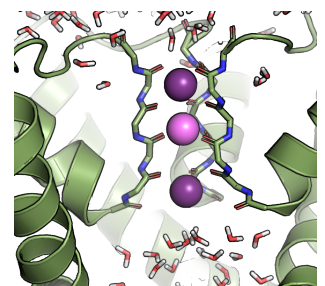


Figure 4.2: **Selectivity filter conformations of hERG simulations and KcsA crystal structures** For clarity, two subunits are shown. Snapshots were taken at the end of the hERG simulations with a 5 Å  $C\beta$  distance between S620 and N629 (A), and a 10 Å distance (B). A flip of the V625 carbonyl group is seen (black arrows). For comparison, (C) displays the crystal structures of the collapsed (pdb: 1K4D) and (D) the conductive KcsA SF (pdb: 1K4C). (E) Comparison with the flipped SF conformation observed in a crystal structure of the non-inactivating KcsA mutant E71A (pdb: 2ATK) (F) Pathway of the SF conformational change as shown by molecular snapshots taken at  $t = 0.4, 20, 40$  and 60 ns. Thermal fluctuations are illustrated by three consecutive snapshots taken 200 ps apart, each near 20 and 40 ns.

ter collapse toward a final state closely resembling the KcsA SF low- $K^+$  state, again within the limits of thermal fluctuation (Fig. 4.2A,C). Please note that Fig. 4.2A,B show simulation snapshots at  $T = 310$  K, and so, in contrast to crystals, a complete



four-fold symmetry between the channel subunits cannot be expected.

The carbonyl groups of V625 were frequently observed to transiently flip backward (black arrows in Fig. 4.2A,B) in our simulations. In the past, such flips have been linked to non-conductive SF states (e.g. [47, 118]), but crystal structures and electrophysiological measurements of a non-inactivatable KcsA mutant (E71A, Fig. 4.2F) have demonstrated that flipped states of V625 retain a conductive channel [53]. In addition, recent crystallographic studies on the E71A KcsA mutant have concluded that the flipped SF conformation is actually yet another conductive filter state, encountered with high frequency [52].

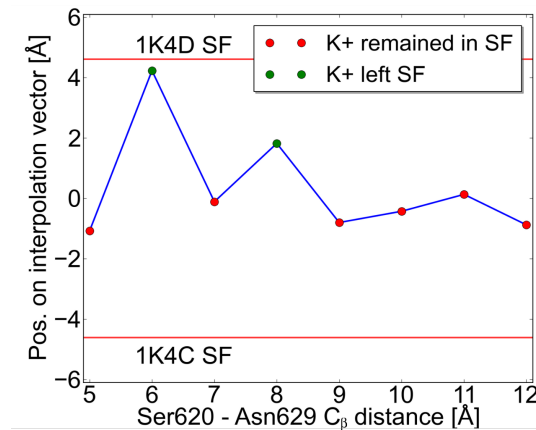


Figure 4.3: **Distance scan (S620-D629) with a single K<sup>+</sup> ion in the hERG SF.** The position on the interpolation vector was sampled after 25 ns simulation time. In all cases in which the ion remains in the SF (red dots), the conformation of the SF remained stable in an intermediate state between the “ordered” 1K4C and “collapsed” 1K4D conformation. At enforced C $\beta$  distances of 6 and 8 Å, the K<sup>+</sup> ion diffused out of the channel (green dots) resulting in a conformational change of the selectivity filter toward the collapsed state. This effect is more pronounced at the shorter S-N distance. We ascribe the lesser extent of the transition toward a collapsed state to insufficient sampling especially when ions are present in the SF.

Taken together, our simulations suggest that the conformational state(s) of S620 and N629 control inactivation of hERG, which comprises a change of the hERG SF from a conductive conformation to a geometry resembling a collapsed SF state. From simulations with varying ion occupancy in the SF (Fig. 4.3), we conclude that the complete transition of the SF is promoted by at least a transient phase in which K<sup>+</sup> ions are not bound in the filter, although the final conformation of the collapsed state exhibits a single K<sup>+</sup> ion in the crystal structures [49]. In a range of further simulations, raised K<sup>+</sup> occupancy disfavored collapse of the SF (Fig. 4.3). It is however important to note the limitations of the present hERG model, which in

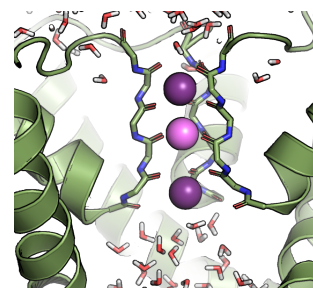
particular include the absence of the extracellular turret loop section which may contribute to inactivation.

#### 4.5.2 Alternating conformations of N629 act as switch for the selectivity filter

We further examined the conformational toggle between S620 and N629 by investigating distances between  $d_{S-N} = 5-12 \text{ \AA}$ . The end points of six additional 50-ns MD simulations ( $d = 6, 7, 8, 9, 11$  and  $12 \text{ \AA}$ ), together with the eight simulations for  $5$  and  $10 \text{ \AA}$ , were determined by averaging the projection of the simulation trajectories onto the difference vector after 40 ns, as described above. As shown in Fig. 4.1D, the degree to which the SF was driven toward the collapsed state showed a strong dependence on  $d_{S-N}$ . The relationship was found to be almost linear between  $d_{S-N} = 5-11 \text{ \AA}$ . Inter-side chain distances of  $10 \text{ \AA}$  and  $11 \text{ \AA}$  stabilized the highly ordered, conductive filter configuration, while small  $d_{S-N}$  drove the SF toward the collapsed state. A sharp move toward the collapsed state was recorded at a distance of  $12 \text{ \AA}$  (and larger distances, not shown). This demonstrates that the distance between S620 and N629 acts as a direct and nearly linear switch that can toggle the SF between its conductive and collapsed state. We identified the close interaction between S620 and N629 as a bidentate hydrogen bond that is stably formed around  $d_{S-N} = 5 \text{ \AA}$ , and disrupted toward  $d_{S-N} = 10 \text{ \AA}$ .

To test the behavior of known inactivation-deficient mutants of hERG in the light of these findings, we investigated both the mutant S620T [102] and the G628C/S631C double mutant [93,102,118], two intensely studied, non-inactivating forms of hERG. In the S620T mutant, a methyl group is added directly behind the SF on the acceptor residue of the proposed hydrogen bond toggle, providing more steric bulk which may alter a potential hydrogen bond network. In the double mutant G628C/S631C, an intra-subunit disulfide bond between sequence positions 628 and 631 is introduced, which is expected to enclose N629 and so to disrupt a possible hydrogen bond between S620 and N629 [118].

Interestingly, we did not observe a complete transition toward the collapsed state in the case of the S620T mutant, despite our simulation settings strongly imposing a distance of  $5 \text{ \AA}$  between T620 and N629, which is the most favorable contact distance for collapse in the wildtype (Fig. 4.1C, magenta curve and Fig. 4.1D, magenta circle). This was due to the additional methyl group, which disrupted a close hydrogen bond contact there. In the G628C/S631C double mutant, the steric hindrance introduced by the disulfide bond inhibited such a close approach even further. Here, the simulations showed that  $d_{S-N}$  remained near  $9 \text{ \AA}$ , a distance which stabilizes the SF near its conductive state (Fig. 4.1D). The mutant data shows that hERG variants with experimentally determined inactivation deficient



cies also exhibit a changed behavior in our simulations. Both mutants were found to be incapable of fully reaching the collapsed SF state.

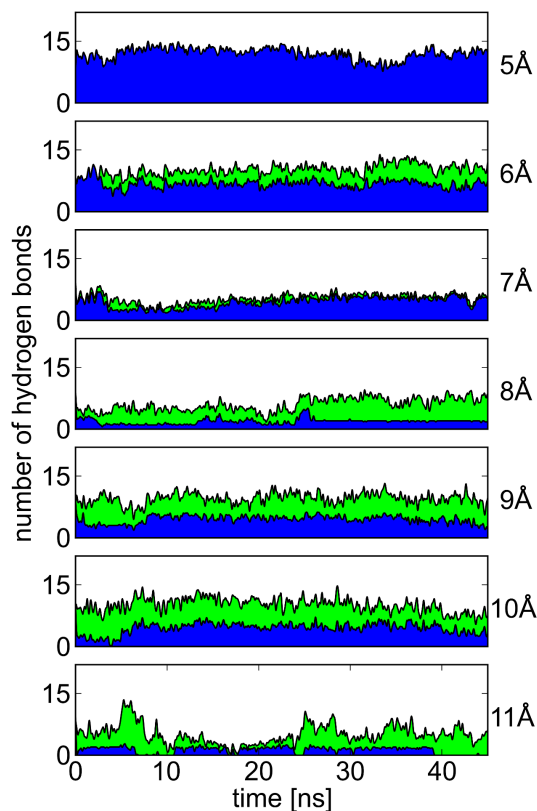


Figure 4.4: **Hydrogen bonds formed by N629 at different S620-N629 distances.** For each S620-N629  $C\beta$  distance we investigated, the number of hydrogen bonds formed by the N629 side-chain to the same subunit (blue area) and to neighboring subunits (green area) is shown over simulation time. A steady rise in the proportion of inter-subunit hydrogen bonds is seen with an increase in S-N distance.

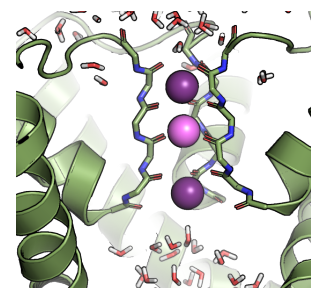
To further evaluate the toggle function of N629 in the course of the simulations, we compared the number of H-bonds formed by N629 to the same and adjacent subunits, respectively (Fig. 4.4). At the smallest S-N-distance, N629 exclusively formed intra-chain H-bonds, whereas toward larger S-N distances, the proportion of H-bonds interconnecting neighboring subunits steadily increased. A closer inspection at S-N distances around  $10 \text{ \AA}$  exhibited inter-subunit H-bonds formed between the side chain of N629 and the backbone carbonyl unit of G628 from the adjacent subunit as the dominant species (Fig. 4.1A). Such a connection can be conceived to stabilize the ordered state of the SF by confining the motion

of the extracellular entry. Simulations of wt-hERG, in which inter-chain N629–G628 H-bonds were further stabilized by introducing a weak harmonic potential, showed that the SF continuously remained near its conductive conformation there, while the S620–N629 distance was around 9 Å such as in the G628C/S631C mutant (Fig. 4.1D).

### 4.5.3 Experimental evidence for the role of N629 and a neighboring H-bond network

A number of mutations around the SF have been found to strongly affect C-type inactivation in hERG [99]. Furthermore, it could be demonstrated in KcsA that mutation of the H-bonding power of W67 strongly influenced KcsA inactivation and the strength of the E71–D80 interaction [51]. According to our structural model and simulations of hERG, the N629 side-chain forms the central inactivation switch by tightly interacting with S620.

We next aimed for independent experimental tests of these hypotheses. Therefore, we measured channel current of a mutant that directly altered the S620–N629 interaction by introducing a longer side-chain into this position (N629Q). Moreover, in our model, the S620–N629 link is surrounded by side chains that are likely to modulate the strength of an in-lying H-bond, either by their hydrophobicity or alternative H-bonding potential. Thus we additionally tested the conservative mutations Y616F, homologous to KcsA W67, and F617Y, which both comprise an altered H-bonding potential in its close vicinity. The effects on hERG inactivation were then monitored using whole-cell electrophysiology in the *Xenopus* oocyte expression system. Fortunately, the three mutant hERG channels expressed functional currents amenable to characterizing the mutational influence on hERG channel activation, deactivation and inactivation, respectively. The voltage dependence of hERG channel steady-state activation was measured with long duration (6 s) depolarizing test pulses. From a holding potential of -100 mV, test pulses ranged from -90 to +40 mV in 10 mV increments, followed by a hyperpolarizing test pulse to -140 mV for recording tail currents (Fig. 4.5, panel III). Tail current amplitudes were normalized and plotted against test potential (Fig. 4.5 III B, C). In agreement with previous data [120], Boltzmann fits to the data showed that the voltage of half-maximal activation ( $V_{1/2}$ ) of wild-type hERG channels was  $-28.5 \pm 0.44$  mV ( $n = 3$ ) with a slope factor  $k = 7.41 \pm 0.39$  mV ( $n = 3$ ). Activation of the mutant Y616F and N629Q hERG channels was shifted by  $\sim 15$  mV to more negative potentials in comparison to wild-type (see Fig. 4.5, panel III B). The steady-state values of  $V_{1/2}$  and  $k$  of wild-type and mutant hERG channels are summarized at the bottom of Fig. 4.5 III. Because the current-voltage relations for the F617Y mutant hERG channel apparently showed two phases, we did not fit a Boltzmann



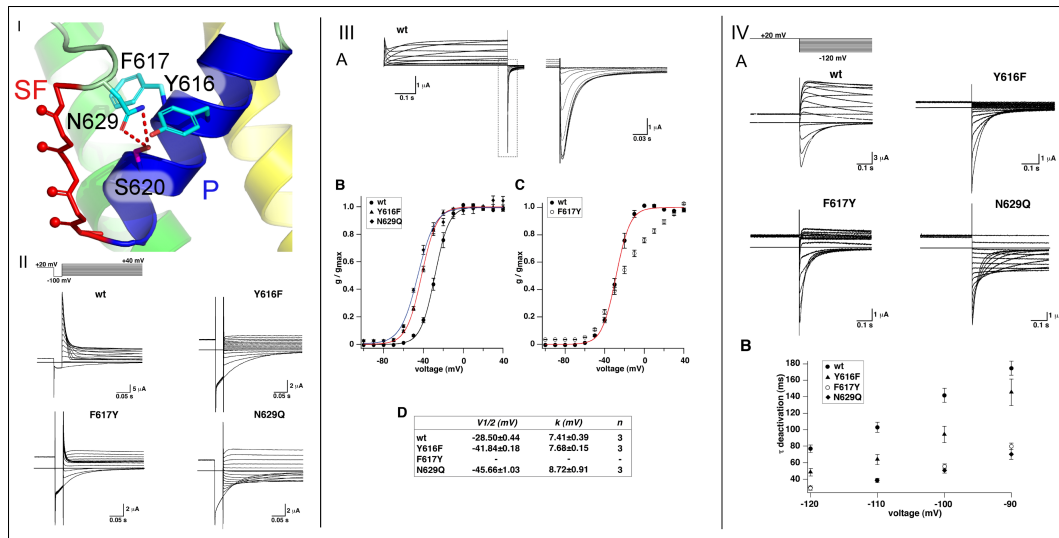


**Figure 4.5: Mutations of the H-bond network behind the selectivity filter.** (I) Mutation sites N629Q (pore loop), F617Y, and Y616F (both: pore helix, P). (II) Inactivation properties of wild-type and mutant hERG channels. Inactivation time courses for the different hERG channels were recorded as shown. A conditioning pulse to +20 mV followed by a 100 ms hyperpolarizing pulse to -100 mV preceded various depolarizing pulses from -90 to +40 mV in 10 mV increments as illustrated by the pulse protocol on top. (III) (A) Exemplary wild-type (WT) hERG current traces elicited by 6 s depolarizing voltage steps from -100 to +40 mV followed by a hyperpolarizing pulse to -140 mV. Respective tail currents are shown enlarged at left. (B) Conductance-voltage relations determined from Boltzmann fits to normalized tail current amplitudes for hERG wild-type and Y616F and N629Q mutant channels. (C) Conductance-voltage relation for the mutant hERG channel F617Y. (D) V1/2 and k parameters obtained under steady state conditions from the Boltzmann fits for wild-type and mutant channels are summarized at the bottom. \* $p < 0.05$  versus wild-type. (IV) (A) Deactivation time courses of wild-type and mutant hERG channels. Tail currents were elicited according to the pulse protocol shown on top. Note mutant hERG channels Y616F, F617Y, and N629Q lack a 'hook' in the tail current indicating that they lost wild-type inactivation behavior. (B) Voltage dependence of mean deactivation time constants ( $\tau_{deact}$ ) ( $n=4$ ) for the different channels as indicated.

function to the F617Y data (Fig. 4.5 III C).

Deactivation time courses were recorded by applying a depolarizing conditioning pulse to +20 mV for 1.6 s from a holding potential of -100 mV, followed by various test potentials from -120 to +50 mV in 10 mV increments for 6 s. Single exponential fits to the data were used to obtain deactivation time constants ( $\tau_{deact}$ ;

Fig. 4.5 IV). Consistent with previous data [101],  $\tau_{deact}$  was, at -120 mV,  $73.2 \pm 4.1$  ms ( $n = 7$ ) for wild-type hERG and, on average,  $33.7 \pm 3.2$  ms ( $n = 6-9$  for each mutant) for the different mutant hERG channels (Fig. 4.5 IV). In comparison, time rise to peak at +20 mV was not markedly different between wild-type and mutant hERG channels (on average  $59.1 \pm 1.8$  ms;  $n = 3-4$  for each channel).

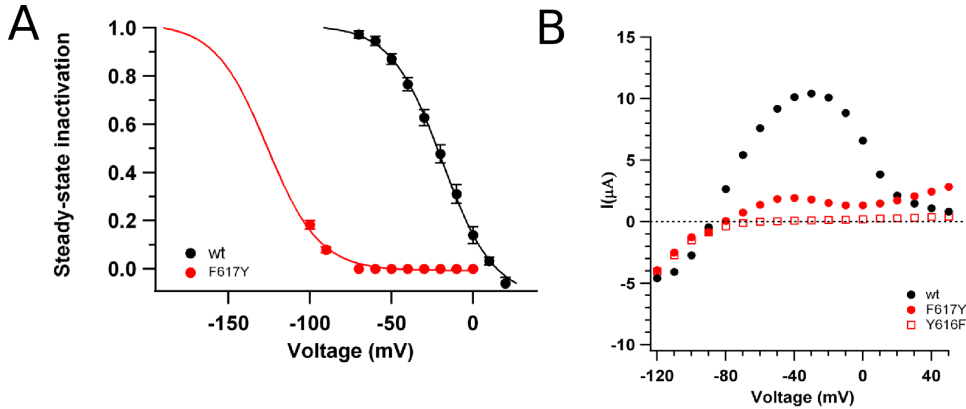
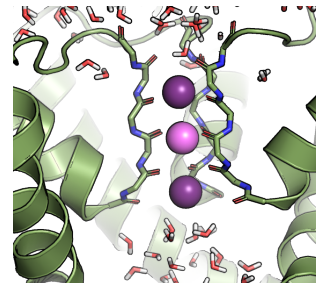


Figure 4.6: **Wild-type and mutant hERG inactivation.** (A) Steady-state inactivation plotted against the voltage of the test pulse. For experimental details see Methods. Solid lines correspond to a Boltzmann fit to the data ( $n = 3$ ; S.E.M.). (B) Voltage-dependence of tail-current amplitudes. Data were obtained using the pulse protocol shown in Figure 4.5 (IV).

The three mutations however had a dramatic effect on hERG channel inactivation (Fig. 4.5 II). In contrast to wild-type, which inactivated rapidly, the mutant N629Q hERG channels were devoid of inactivation ( $n = 8$ ). In the case of Y616F and F617Y hERG channels, we observed a strong inward rectification (Fig. 4.6). It indicated that the mutations had shifted the voltage-dependence of hERG steady-state inactivation to very negative test potentials. Steady-state inactivation was determined at different test potentials from the ratio of instantaneous current amplitude and current amplitude remaining 100 ms after the onset of the test potential. We plotted the normalized inactivation data as a function of voltage (Fig. 4.6). Fitting a Boltzmann function to the wild-type data, we estimated that the voltage of wild-type half-maximal steady-state inactivation ( $V_{1/2,inact}$ ) was  $-18.8 \pm 0.8$  mV ( $n = 3$ ; S.E.M.), in agreement with data in the literature [115, 121].  $V_{1/2,inact}$  for the Y616F mutant was so strongly negatively-shifted that we were unable to obtain sufficient data points for measurement.  $V_{1/2,inact}$  for the F617Y hERG mutant was negatively-shifted by about 100 mV. Using an open fit to our limited set of data we estimated  $V_{1/2,inact}$  for the Y616F hERG channel at  $-126.6 \pm 1.3$  mV ( $n = 3$ ; S.E.M.). Also, the F617Y mutation affected the inactivation time course ( $\tau_{inact}$ ). Fitting a single exponential to the inactivation time courses, we obtained at -20 mV for the



wild-type channel a  $\tau_{inact}$ -value of  $21.73 \pm 1.63$  ms ( $n = 4$ ) and for the F617Y mutant one of  $5.57 \pm 0.25$  ms ( $n = 4$ ; Fig. 4.5II).

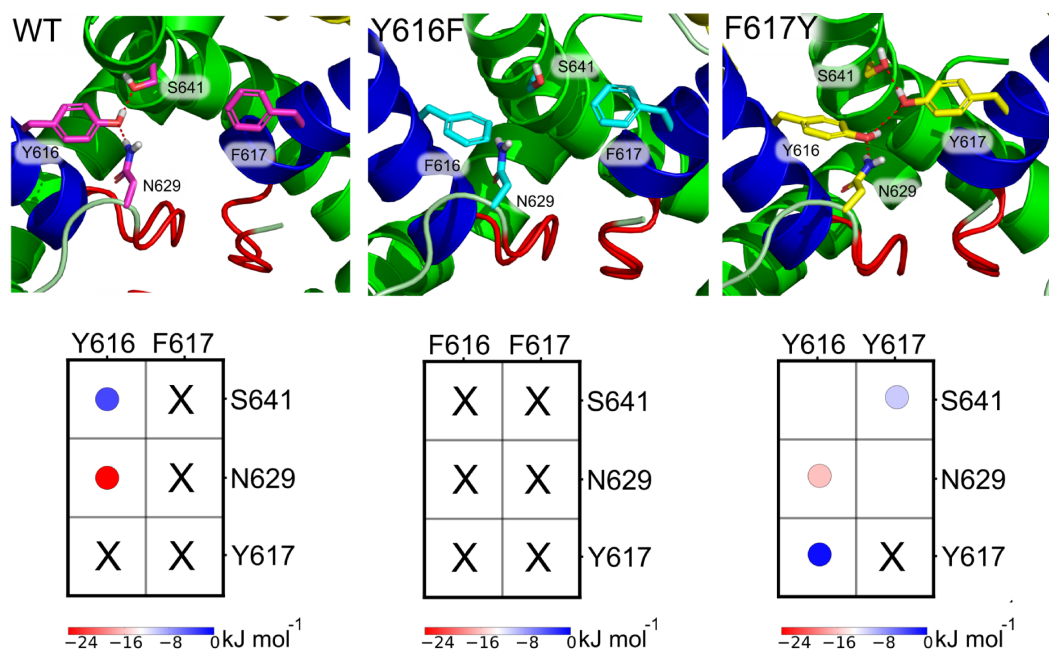


Figure 4.7: Comparison of the H-bond pattern in WT hERG and the mutants Y616F and F617Y. (Left) Typical structural arrangement of the H-bond network around N629 with H-bonds marked by broken red lines in the WT (top), Y616F (center) and F617Y mutant (bottom). (Right) Matrices of the presence and strength of H-bonds for WT (top) and mutant hERG (middle, bottom). A cross indicates that no H-bonds are formed between the respective residues.

The experimentally investigated set of mutants was further studied in extensive MD simulations. To examine changes of the suggested inactivation switch in either direction, the N629 side-chain was modeled in an intermediate position between G628 and S620. Hydrogen bonds formed in its vicinity were then investigated, and their interaction energies were calculated according to Espinosa et al. (1998) [122]. In the WT, a strong H-bond was observed between Y616 and N629 (Fig. 4.7, upper panel). This interaction was extended to form an H-bonding triad with S641, a position known from experiment to have a pronounced impact on inactivation [92,123]. Simulations of the mutants Y616F and F617Y showed a major alteration in this H-bonding network. The mutant Y616F completely removed the triad, while introduction of F617Y perturbed the triad by replacing the direct H-bonding interaction between Y616 and N629, both thereby influencing the position of N629 (Fig. 4.7, center and lower panel). Our results thus suggest that both mutations impact on inactivation by perturbing the finely-tuned H-bonding network around



N629 that keeps its side-chain in position for function as the inactivation switch.

#### 4.5.4 Structural links to modulation of cavity shape and effect of hERG agonists

Impairment of C-type inactivation is responsible for short-QT syndrome and plays a key role in drug-induced gain of function in hERG [104]. hERG agonists are of great potential therapeutic interest [124, 125], forming a possible basis for treatment of patients suffering from inherited long-QT hERG mutations [104]. We were therefore interested in the interplay between small molecule binding to the inner cavity of the hERG channel and C-type inactivation.

We focused on two recently described hERG agonists, PD-118057 [104] and ICA-105574 [112, 126]. Both molecules have been shown to interact predominantly with a hydrophobic binding pocket near residue F619 on the hERG pore helix [104, 112]. On the basis of our previous results, the inactivated state of hERG was modeled by simulating a conformation with a collapsed SF, while the open form was assumed to exhibit a conductive SF. In both cases, we carried out 100-ns MD simulations.

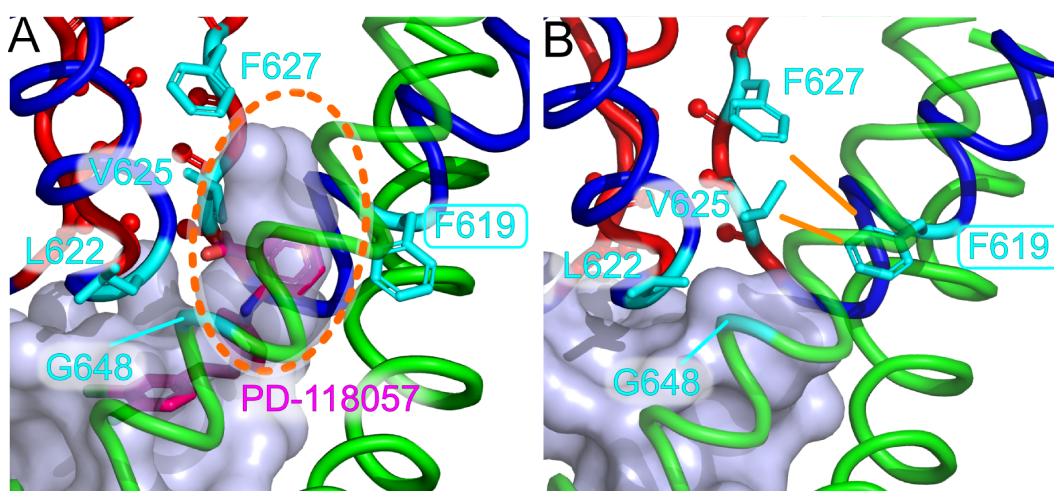
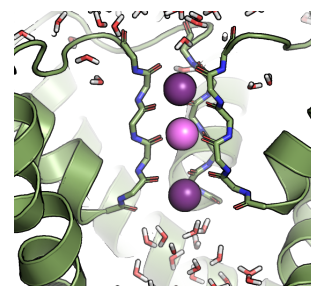


Figure 4.8: **Suggested mechanism of action of the hERG activator PD-118057.** The binding cavity for activators is present only in the active, conductive state of the SF, such that the active state becomes stabilized by activator binding. **(A)** The experimentally determined binding pocket for PD-118057 is located around residue F619 (orange ellipse) and extends to L622. **(B)** A cascade of conformational changes triggered by collapse of the SF leads to constriction of the binding pocket (orange lines) and rearrangement of L622.

The conformational change at the SF initially had a moderate direct spatial extent (initial RMSD in the SF:  $\sim 1$  Å). Intriguingly however, it had far-ranging subsequent consequences near the pore helix and the interface with S6 in the trajectories:



The subtle conformational change within the backbone of the SF (S624-G628) was gradually amplified by inducing side chain rotations, in particular those of V625 and F627. This reordering led to rotation of the directly neighboring residue L622 on the pore helix and the main drug binding site F619, one helical turn upward. In concert, these rearrangements in the activated open state were found to be capable of opening a side pocket, extending from the main cavity (Fig. 4.8 A,B), which was found to be wide enough to accommodate either PD-118057 and ICA-105574 in molecular docking calculations. In contrast, the pocket was smaller and only transiently present in the inactivated state, blocking their entry (Fig. 4.8 C).

A closer look at the residues found to be important for activator interaction reveals that both the location and extent of the side-pocket are in good agreement with the main interaction sites identified in Refs. [104] and [112] (Fig. 4.8 D,E). The residues shown to interact with ICA-105574 are however located at the lower entrance of the side-pocket and so a slightly different mode of binding is suggested (Fig. 4.8 E). We propose a mechanism, in which activator molecules belonging to this class are able to bind in this side-pocket in the activated open, but not in the inactivated state. Thus, by stabilizing the activated state, inactivation is putatively impaired by these molecules.

## 4.6 Discussion

Inactivation of hERG is of crucial physiological and medical importance, as it is instrumental in controlling the duration of the cardiac action potential. Our simulations suggest that the inactivated state of hERG resembles a collapsed SF conformation and propose a mechanism for hERG entry into inactivation, relying on the group N629 alternating between intra- and inter-subunit hydrogen bonds as a toggle. The toggle is influenced by a finely-tuned neighboring H-bond network. Non-inactivating mutants are observed to be unable to form an intra-subunit H-bond conformation and thus do not reach a collapsed SF state. To validate these findings, we conducted mutation studies and electrophysiology experiments which showed a dramatic effect of conservative mutations that alter the steric properties and H-bonding potential near the S620-N629 switch.

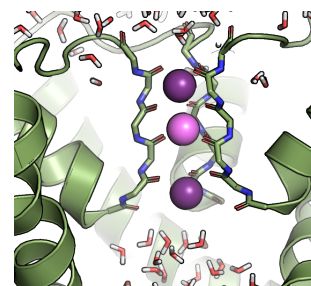
Recently, it has been shown that a similar collapse of the SF likely underlies slow inactivation in the prokaryotic K<sup>+</sup> channel KcsA, with a network of H-bonds around D80 controlling the state of the SF [37,51]. There are important functional differences between slow inactivation in KcsA and hERG inactivation. However, recent mutational studies highlight the mechanistic similarities between KcsA and K<sub>v</sub> channel inactivation, given the high level of functional and structural conservation in the K<sup>+</sup> channel pore domain [37,116]. Our work thus expands the findings on KcsA into the domain of voltage-gated K<sup>+</sup> channels. The tight interac-

tion between two side chains in the same subunit that form a strong H-bond (S620 and N629) may explain the strong inactivation tendency of hERG as compared to other  $K^+$  channels, where the homologous groups have a weaker H-bonding potential (e.g.  $K_v$  1.3, KcsA). The hydrophobic character of the immediate environment, possibly also the unusual sequence of the hERG SF (GFG instead of GYG), contribute to the strength of this H-bond and the rapid time course of hERG inactivation. Our results also have some bearing on a recent electrophysiological study on Kir1.1 [127], which indicated an inter-subunit salt bridge network strongly affecting inactivation of the inwardly rectifying Kir1.1 channel. Kir1.1 residues involved in these salt bridges (E118, R128, and E132) occupy sequence positions homologous to S620, V630, and T634 in hERG, suggesting a similar role of an inter-/intra-chain H-bond equilibrium controlling inactivation.

We suggest that the S620-N629 interaction constitutes the innermost element of a wide range of allosteric switches that can alter inactivation in hERG and the stability of the open state of the channel. Some of the wide-ranging rearrangements were elegantly demonstrated by Wang et al. [116]. More distant effects include sequence-distal interactions such as S641, mutations of which have been demonstrated to impact inactivation [116,123] and, possibly, domain motions encompassing regions as far as helices S6, S4, and the S4-S5 linker in early stages of inactivation [116]. In line with this, our mutations slightly affect hERG current-voltage-relations and deactivation time-courses. Our study shows an intricate network of hydrogen bonds that may have a profound effect on the workings of the inner switch and on the link between inactivation and activation gating [128].

The intensely studied mutant hERG channel hERG S620T and the double mutant G628C/S631C, which have shown inactivation-deficiency in earlier experimental studies [93,102,118], were investigated and displayed an inability to attain a collapsed SF state. The importance of the proposed switch may also become evident from comparison with the closely related hEAG1 channel, in which threonine occupies the location homologous to S620 in hERG (T432 in hEAG). Similar to the hERG S620T mutant, hEAG lacks C-type inactivation [129].

Unfortunately, a complete structural model of hERG including the turret loop region is presently not available, owing to its largely disordered character. Our investigation relies on the present consensus hERG model [94], such that more distant interactions including the turret section were not addressed here. Most cases of inherited short-QT syndrome are however elicited by the hERG mutation N588K in this turret region [105–107]. Sequence position 588 is located in a stretch of residues characterized by the fact that each group strongly affects inactivation when it is mutated (W585–G594) [99]. It had hence been suggested and later confirmed that this stretch forms an alpha-helical section within the turret loop, which immediately borders the SF [130,131]. According to these data, N588 is



located directly next to the SF mouth and thus to N629. We speculate that a lysine at this position could either interact unfavorably with the H-bonding network that controls inactivation or act like SF-binding lysines in channel toxins, which have been shown to induce recovery from inactivation in  $K^+$  channels by an interaction near the filter [54].

On a longer range, we found that the conformational change of the SF from the collapsed to the conductive state altered the shape of the hERG inner cavity. Our simulations showed that the hERG agonists PD-118057 and ICA-105574 are bound in a side pocket of the cavity near F619 that is large enough to accommodate the agonists, but only exists in the activated state. It had been previously established by experiment that PD-118057 and ICA-105574, drugs that inhibit inactivation and thus increase hERG current, bind near F619 and L622 [104, 112]. Such hERG agonists are considered a new approach for the treatment of long-QT associated arrhythmia. Our results provide a simple explanation for the activation of hERG by these agonists, which may also hold true for other hERG activators: The groups V625 and F627, part of the SF, are prevented from adopting their collapsed-SF positions by the action of this small molecule (Fig. 4.8 B,C), i.e. the SF cannot reach its inactivated conformation. In contrast to hERG blockers which bind inside the ion conduction pathway and reduce current [48], binding of activator molecules to the side-pocket does not negatively affect ion flux through the pore [104].

## 4.7 Acknowledgments

This work was partially funded by the Dutch TI Pharma project D2-101 (G.V., B.L.dG., U.Z.) and a grant from the Deutsche Forschungsgemeinschaft to O.P. (Po137/39-1).

## 5. Ion Permeation in $K^+$ Channels Occurs by Direct Coulomb Knock-On

This chapter has been published as **David A. Köpfer**, Chen Song, Tim Gruene, George M. Sheldrick, Ulrich Zachariae, Bert L. de Groot. Ion Permeation in  $K^+$  Channels Occurs by Direct Coulomb Knock-On *Science* 346, 352 (2014); DOI: 10.1126/science.125

### 5.1 Own contribution

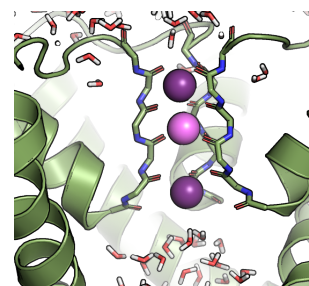
Molecular dynamics simulations were carried out by Chen Song (simulations VIII, IX XII and XIII Tab. 5.1) and me (all production simulations Tab. 5.1 and control simulations VI, VII, X, XI, XIV, XV, XVI in Tab. 5.2). I performed the analysis of the MD simulations. Chen Song performed the Brownian dynamics simulations. Tim Gruene carried out the crystallographic analysis.

### 5.2 One sentence summary

Atomistic molecular dynamics simulations, together with re-refinement of high-resolution x-ray structures, reveal that efficient ion permeation in potassium channels occurs via an electrostatic knock-on mechanism by direct ion-ion contacts.

### 5.3 Abstract

Potassium channels selectively conduct  $K^+$  ions across cellular membranes with extraordinary efficiency. Their selectivity filter exhibits four binding sites with approximately equal electron density in high- $[K^+]$  crystal structures, thought to reflect a superposition of alternating ion and water occupied states. Consequently, co-translocation of ions with water has become a widely accepted ion conduction mechanism for potassium channels. By analyzing over 1,300 permeation events from molecular dynamics simulations at physiological voltages, we



observe instead that permeation occurs via ion–ion contacts between neighboring  $K^+$ . Coulomb repulsion between adjacent ions is the key to high efficiency  $K^+$  conduction. Crystallographic data is consistent with directly neighboring  $K^+$  ions in the selectivity filter, and our model offers an intuitive explanation for the high throughput rates of  $K^+$  channels.

## 5.4 Introduction

Potassium ( $K^+$ ) channels play fundamental roles in almost all cell types. They are essential elements in cellular electric excitability and help maintain the resting potential in non-excitabile cells. Their universality is based on a unique combination of strong selectivity for  $K^+$  ions with near-diffusion limited permeation efficiency [1]. Common to all  $K^+$  channels is the highly conserved  $K^+$  selectivity filter (SF), which underlies both their exquisite  $K^+$  selectivity and high conduction rates. A wealth of  $K^+$  channel structural information has been acquired since 1998 [15]. The structures revealed that the SF is formed at the interface of four channel subunits, each contributing a linearly extended backbone of 5–6 residues (Fig. 5.1A, left), the carbonyl groups of which point into a fourfold symmetric narrow pore [15]. This arrangement generates four equidistant  $K^+$  binding sites ( $S_1$ – $S_4$ ; Fig. 5.1A, right) [15, 37, 49, 132].

Anomalous scattering data from the bacterial  $K^+$  channel KcsA from *Streptomyces lividans*, in whose SF  $K^+$  ions were replaced with  $Tl^+$ , was originally interpreted as a superposition of two states, each displaying occupation with two alkali ions alternating with water (Fig. 5.1B) [132]. This interpretation still forms the basis for the commonly accepted  $K^+$  conduction mechanism, which suggests co-transport of ions with water [6, 22, 40, 41, 132] (Fig. 5.2). Any possible closer grouping of  $K^+$  ions had been excluded owing to the expectation that the electrostatic repulsion between the ions would prohibit such an arrangement [41, 132], although it was noted that geometrically, the ions could fit in the filter side by side [41, 133]. The notion of  $K^+$ -water co-translocation has been transferred to other  $K^+$  channels [3, 134–136], and similar mechanisms have been reported in equilibrium [19, 42, 134, 137, 138] and non-equilibrium simulation studies [20, 139, 140]. In most of these, biasing restraints were applied on the filter and/or supra-physiological trans-membrane voltages were applied to elicit ion transfer [20, 139, 140]. However, alternative computational studies demonstrated that multiple pathways may exist, including mechanisms that exhibit close ionic contacts and display similar free energy barriers to  $K^+$  permeation [21, 137, 141]. It has thus remained unclear which mechanism of  $K^+$  permeation predominates under physiological conditions.

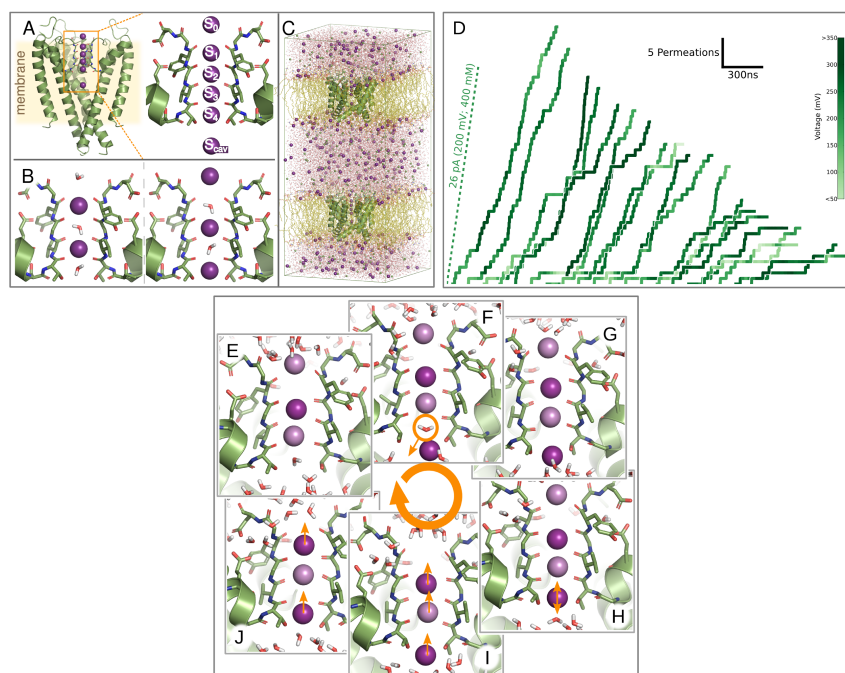
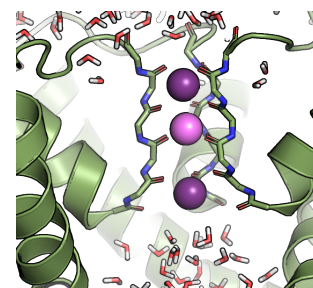


Figure 5.1: **Molecular dynamics simulations of voltage-driven  $K^+$  permeation in KcsA.** (A) X-ray structures of KcsA crystallized under high  $K^+$  concentrations display six ion binding sites at the SF (PDB ID: 1k4c, for clarity only two or three sub-units are shown). (B) The underlying electron density had been interpreted as a superposition of two alternating patterns within the SF ( $K^+$  /water/ $K^+$  /water and water/ $K^+$  /water/ $K^+$ ). (C) The simulation system consists of two membranes, each including open KcsA (shown: PDB ID: 3f5w), surrounded by water and ions, and exhibits a trans-membrane voltage gradient. (D) Permeation events as a function of time (each step represents the permeation of a single  $K^+$  ion) over 20 individual simulations at 400 mM KCl (set I, see Tab. tab:KK:productsim), and comparison with experimentally measured ion currents (dashed line, data from ref. (36)). The slope of each curve denotes computed or experimental current. The trans-membrane voltage measured in experiments and simulations is color-coded from light to dark green. (E–J) Observed mechanism and sequence of events during  $K^+$  translocation. The most frequent ion configuration under voltage contains two  $K^+$  ions at  $S_2$  and  $S_3$  and a more loosely bound ion at  $S_0$ , leaving a vacancy at  $S_1$  (E). Permeation starts when a  $K^+$  ion enters the cavity and binds to  $S_{cav}$  (F). Upon displacement of a water molecule (G), translocation of the central ions is triggered by fluctuations of the incoming ion between  $S_{cav}$  and  $S_4$ , coinciding with release of  $K^+$  from  $S_0$  into the solution (H). Ions at  $S_3$  and  $S_2$  advance in a fast, concerted transition (I), followed by the movement of ions at  $S_4$  and  $S_1$  (J), re-establishing the initial configuration (E).



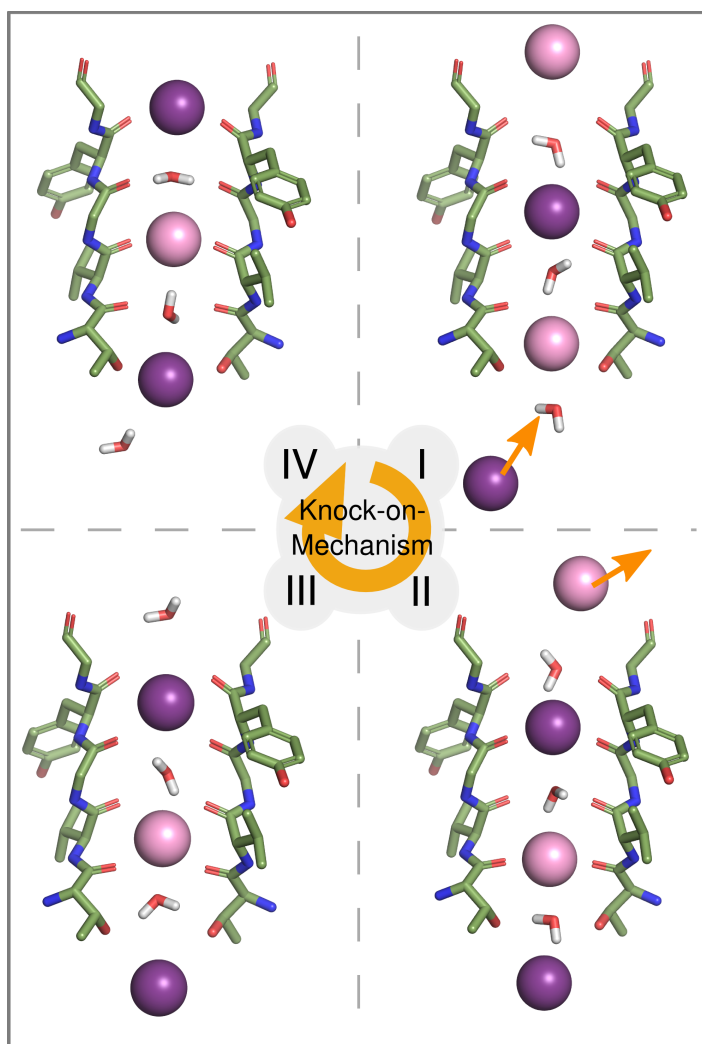


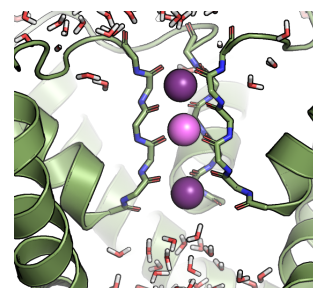
Figure 5.2: The originally proposed permeation mechanism, in which  $K^+$  and water molecules occupy the binding sites in the selectivity filter in an alternate fashion and translocate collectively (knock on). (I)  $K^+$  ions and water molecules occupy alternating sites in the SF, in the case shown, binding sites  $S_2$  and  $S_4$ . An arriving ion binds to  $S_{cav}$  and knocks on the column in the SF, (II) expelling the outermost ion into the bulk. (III) The SF enters its second stable conformation with ions bound to  $S_1$  and  $S_3$ . Eventually, this conformation is thought to relax into the initial conformation, translocating a co-transported water toward the extracellular side.



## 5.5 Materials and methods

### 5.5.1 Molecular dynamics simulations

The simulation systems we used were constructed from the PDB  $K^+$  channel crystal structures 3f5w (KcsA) [37], 3fb7 (KcsA) [37], 3ldc (MthK) and 2r9r ( $K_v$  1.2- $K_v$  2.1 'paddle chimera', [16]). As the KcsA structure 3f5w displays the largest opening at the helix bundle gate, we used it for the majority of our simulations. We also used a computationally opened variant of the closed bundle crossing KcsA structure 1k4c as control [142]. In the case of KcsA, the protein was protonated according to standard protonation at pH 7 except for E71, which was protonated in agreement with previous studies [143]. The protein was inserted into a lipid bilayer surrounded by explicit water molecules and KCl. To equilibrate the system, we position-restrained all heavy atoms with a force constant of 1000 kJ mol<sup>-1</sup> nm<sup>-2</sup> to the reference structure (initial structure 3f5w), except for the selectivity filter motif (TTVGYG) where the high [ $K^+$ ] conformation found in 1k4c [49] was used as a reference to create an open activated conformation. After 20 ns equilibration, the system was duplicated along the z direction and an ionic imbalance of 2  $K^+$  ions between the compartments was kept constant by the computational electrophysiology method [67], resulting in a trans-membrane voltage of approximately 200 mV. Initially,  $K^+$  ions were positioned in the selectivity filter as found in the crystal structures (see Tab. tab:KK:productsim and tab:KK:validsim). The control simulations were set up in an analogous way as indicated in Tab. tab:KK:validsim. We used different setups in our simulations, which varied in the lipid type (POPC or DMPC), the ion concentration, as well as the force fields, water and ion models (for details, see Tab. tab:KK:productsim). Our production simulations were performed with the AMBER99sb force field [78]. Two ion models, developed by Joung et al. and Dang et al., respectively [144, 145], were utilized in our study with the AMBER99sb force field. All simulations were conducted using a modified version of Gromacs 4.6 [84], electrostatic interactions beyond a cutoff of 1 nm were treated by PME [83, 86], and the cutoff of vdW interactions was set to 1 nm. Temperature and pressure were kept constant at 320 K and 1 bar with the v-rescale thermostat [86] and a semi-isotropic Berendsen barostat, respectively [85]. All bonds were constrained with the LINCS algorithm [76] and virtual sites were used for protein hydrogen atoms to allow for a 4 fs integration time step [77]. To avoid unwinding of the S6 helix, additional distance restraints were added to the backbone hydrogen bonds. To keep the cavity in an open-hydrated state, distance restraints were applied to the F103 residues as well as the ends of the S6 helix. In addition, we also used the CHARMM36 [146] force field in a set of control simulations. In these simulations, instead of distance restraints, we employed restraints on the



transition vector corresponding to the open-close collective motion of the helices (which was obtained from principal component analysis), to prevent the channel gates from closing. We used similar parameters as in the above AMBER simulations, with the exceptions that the cutoff of vdW was set to 1.2 nm and a shift function was used to smoothly turn off the vdW interactions from 0.8 to 1.2 nm.

Table 5.1: **Simulation details for production MD simulations.** Production simulations (I-V) varied in lipid composition and ion concentration.

Simulation set	I	II	III	IV	V
Structure	KcsA 3f5w with 1k4c SF	KcsA 3f5w with 1k4c SF	KcsA 3f5w with 1k4c SF	KcsA 3f5w with 1k4c SF	KcsA 3f5w with 1k4c SF
force field	amber99sb	amber99sb	amber99sb	amber99sb	amber99sb
Lipid	432 POPC Berger et al.	432 POPC Berger et al.	432 POPC Berger et al.	356 DMPC Berger et al.	356 DMPC Berger et al.
Water	29052 SPC/E	29610 SPC/E	29610 SPC/E	18272 SPC/E	18272 SPC/E
Ion	400mM 312 K <sup>+</sup> 320 Cl <sup>-</sup> Joung et al.	200mM 190 K <sup>+</sup> 198 Cl <sup>-</sup> Joung et al.	10mM 15 K <sup>+</sup> 23 Cl <sup>-</sup> Joung et al.	400mM 230 K <sup>+</sup> 238 Cl <sup>-</sup> Joung et al.	200mM 116 K <sup>+</sup> 124 Cl <sup>-</sup> Joung et al.
SF starting pattern (S <sub>0</sub> - S <sub>cav</sub> )	KKKKKK	KKKKKK	KKKKKK	KKKKKK	KKKKKK
Independent simulations	20	15	10	10	10
Total simulation time ( $\mu$ s)	15.1	4.1	4.7	5.1	2.7
Total permeations	496	136	28	267	83
Voltage (mV)	210 $\pm$ 70	230 $\pm$ 80	260 $\pm$ 20	370 $\pm$ 140	440 $\pm$ 110

## Control simulations

We carried out a number of additional control simulations as listed in Tab. 5.2.

### K<sup>+</sup> concentration

Simulations carried out at different K<sup>+</sup> concentrations showed little effect on the population of the ion occupancy states in the SF (see Fig. 5.8). In accordance with experimental results, the current decreased as fewer ions reached the cavity per time unit. This, however, had no effect on the permeation mechanism involving direct ionic contacts we observed.

### KWKW configuration

The canonical KWKW pattern in the SF most frequently leads to an impermeable state without conductance (simulations VI, VII, XIII). During some of the simulations from set VII, water was expelled from the SF, after which a sustained ionic current was recovered. All permeation events thereafter followed the reported permeation mechanism with direct ionic contacts.

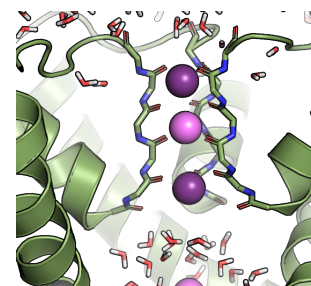
Table 5.2: **Simulation details for control MD simulations.** For control simulations (VI-XVI), the major modifications compared to the production simulations are indicated in bold face.

Simulation set	VI	VII	VIII	IX	X	XI
Structure	KcsA 3f5w with 1k4c SF	KcsA 3f5w with 1k4c SF	KcsA 3f5w with 1k4c SF	<b>KcsA 3fb7</b>	KcsA 3f5w with 1k4c SF	KcsA 3f5w with 1k4c SF
force field	amber99sb	amber99sb	amber99sb	amber99sb	amber99sb	amber99sb
Lipid	356 DMPC Berger et al.	432 POPC Berger et al.	356 DMPC Berger et al.	398 DMPC Berger et al.	432 POPC Berger et al.	432 POPC Berger et al.
Water	18272 SPC/E	29052 SPC/E	18272 SPC/E	25120 SPC/E	<b>29052 TIP3P</b>	<b>29052 TIP4P</b>
Ion	400 mM 230 K <sup>+</sup> 238 Cl <sup>-</sup> Joung et al.	400 mM 312 K <sup>+</sup> 320 Cl <sup>-</sup> Joung et al.	<b>400 mM</b> <b>230 K<sup>+</sup></b> <b>238 Cl<sup>-</sup></b> <b>Dang et al.</b>	<b>600 mM</b> <b>470 K<sup>+</sup></b> <b>486 Cl<sup>-</sup></b> <b>Dang et al.</b>	400 mM 312 K <sup>+</sup> 320 Cl <sup>-</sup> Joung et al.	400 mM 312 K <sup>+</sup> 320 Cl <sup>-</sup> Joung et al.
SF starting pattern (S <sub>0</sub> - S <sub>cav</sub> )	<b>WKWKWK</b>	<b>WKWKWK</b>	KKKKKK	KKKKKK	KKKKKK	KKKKKK
Independent simulations	4	6	5	5	5	5
Total simulation time (μs)	1.1	1.4	1.5	1.7	1.2	1
Total permeations	0	31*	70	27	80	42
Voltage (mV)	210±70	180±70	220±40	240±90	200±80	370±60
Simulation set	XII	XIII	XIV	XV	XVI	
Structure	KcsA 3f5w with 1k4c SF	KcsA 3f5w with 1k4c SF	<b>KcsA 1k4c</b> with opened gate	<b>MthK 3ldc</b>	<b>Kv1.2 2r9r</b> with 1k4c SF	
force field	<b>charm36</b>	<b>charm36</b>	amber99sb	amber99sb	amber99sb	
Lipid	378 DMPC charmm	378 DMPC charmm	428 DMPC Berger et al.	432 POPC Berger et al.	POPC Berger et al.	
Water	20892 TIP3P	20892 TIP3P	29678 SPC/E	28693 SPC/E	24688 SPC/E	
Ion	400 mM 270 K <sup>+</sup> 278 Cl <sup>-</sup> charm36	400 mM 270 K <sup>+</sup> 278 Cl <sup>-</sup> charm36	100 mM 148 K <sup>+</sup> 148 Cl <sup>-</sup> Joung et al.	300 mM 311 K <sup>+</sup> 287 Cl <sup>-</sup> Joung et al.	600 mM 470 K <sup>+</sup> 454 Cl <sup>-</sup> Joung et al.	
SF starting pattern (S <sub>0</sub> - S <sub>cav</sub> )	KKKKKK	<b>WKWKWK</b>	KKKKKK	KKKKKK	KKKKKK	
Independent simulations	5	5	10	10	10	
Total simulation time (μs)	1	1.3	1.7	3.9	2.5	
Total permeations	29	0	33	39	21	
Voltage (mV)	560±120	340±66	90±50	220±60	230±120	

\*all permeation events occurred after direct ionic contacts were recovered.

## Ion parameters

These simulations probed the sensitivity of our results to the employed ion model. As a variant from the most recent Joung et al. [144] ion parameters, we switched the parameterization to parameters according to Dang et al. [145] (sets VIII and IX) Both ion parameter sets were developed to more closely match experimental observables such as dehydration enthalpy. The results closely match those with the ion parameters from Joung et al.; all permeation events occurred with direct K<sup>+</sup>-K<sup>+</sup> contacts and no water permeated.



### Force field

Simulation sets XII and XIII were carried out using the CHARMM36 force field and with a change in the water model to TIP3P. Compared to the AMBER simulations with the SPC/E water model, two differences were observed: Firstly, the channel showed a stronger tendency to close at the lower helices, so we added an additional restraint to ensure an open conformation. Secondly, a higher trans-membrane voltage of 600mV was required for ions to permeate and even then the observed currents were generally lower. The lower currents were somewhat expected as the dehydration energy of ions in CHARMM is usually larger than experimental values [147]. However, despite these differences, all observed ion permeation events occurred with direct  $K^+ - K^+$  contacts. During sustained currents in simulation set XII no water was permeated and as in the AMBER99sb force field, adding water to the SF (as in simulation set XIII) was found to disrupt ion permeation.

### Channel structure

For additional extended simulations, we used two alternative crystal structures of KcsA: PDB id 3fb7, which is considered an open activated conformation (simulation set IX) and the closed activated structure (PDB id 1k4c), of which we used a structure that had been progressed toward the opened configuration in an extended MD simulation [142]. In both cases, we found an identical ion permeation mechanism as in the simulations based on PDB id 3f5w (see Fig. 5.3). In addition, we ran simulations under the same conditions using the eukaryotic  $K_v$  1.2- $K_v$  2.1 channel chimera (PDB id 2r9r) and the high resolution MthK (PDB id 3ldc) structure used previously for our crystallographic re-refinement. Here, the overall permeation mechanism was slightly different at the level of stable configurations in the SF (e.g. in MthK  $S_4, S_3$  and  $S_1$  were most prominently occupied), but both channels showed continuous current (see Fig. 5.3) with ions in adjacent sites of the SF 'knocking-on' each other, and water was absent from the SF.

### High voltage calculations

In addition, we carried out simulations with a high trans-membrane voltage of 1 V. In these simulations, the KcsA structure experiences instabilities, so a position restraint on the filter had to be applied to maintain its conformation. Interestingly, in these less realistic high-voltage simulations,  $K^+$  and water molecules were seen to permeate in an alternating pattern.

### Low temperature simulations

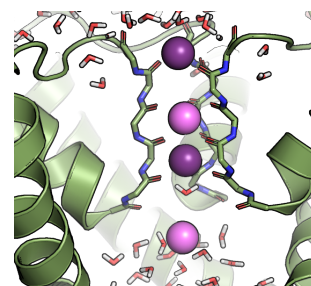
We carried out simulations with KcsA (PDB id: 1k4c) and MthK (PDB id: 3ldc) in water at a  $[K^+]$  of 400 mM, without electrical potential and decreasing temperatures to match more closely the crystal conditions. At temperatures of 200 K and below the four  $K^+$  ions remained stably bound in the SF during the whole simulation (5 independent runs 20 ns each). With increasing temperatures up to 300 K the ion occupancy included configurations closer to those observed under physiological voltages with increasing probabilities for vacancies at  $S_1$  and  $S_4$ .

### 5.5.2 X-ray crystallography analysis

As crystallographic models represent the average of all unit cells in the crystal, the occupancy of the ion sites in crystallographic models would be less than one if water molecules were present between  $K^+$  in the SF. In a scenario with an equal mixture of KWKW/WKWK, an effective occupancy (see eq. 5.1) of 0.5 would be expected for each site. In this scenario, vacancy sites instead of water molecules would result in occupancies lower than 0.5. Our analysis resulted in occupancies close to 1.0. This signifies that, in the crystal structures,  $K^+$  ions can assume (and actually do assume) neighboring sites inside the SF. The results of all occupancy refinements are summarized in Tab. 11.2 and 11.2. Data Preparation: Data and coordinates for PDB ids 3ldc, 2qks, and 1r3j were downloaded from [www.pdb.org](http://www.pdb.org). Data were converted from mmCIF- to mtz-format with CIF2MTZ [148]. The cif-file 1r3j-sf.cif contains two data blocks. The second one, r1r3jAsf, has unmerged Friedel pairs, i.e. the anomalous data. In this case CIF2MTZ was used with its subcommand "BLOCK r1r3jAsf". In case of 3ldc and 2qks, the mtz-files were converted to hkl-format with MTZ2HKL [149], in case of 1r3j, the mtz-file was converted to sca-format with MTZ2SCA [149] because of the different ways the Friedel pairs are stored in the mtz-files. Anomalous differences from 3ldc and 1r3j were extracted with XPREP (Bruker AXS, 2014). Coordinates were converted to SHELX-format with SHELXPRO [150]. Dispersive corrections at the published wavelengths were calculated with SHELXLE [151] according to Kissel and Pratt [152], listed in Tab. 11.4.  $R^{\text{free}}$  reflections for cross validation [153] were conserved from the deposited data.

### Refined and effective occupancy

According to the previous model,  $K^+$  ions were thought unlikely to be present at adjacent sites contemporaneously. Shared ion/water occupancies were not explicitly modeled with SHELXL. Rather, the scattering from a mixture of ion/water was approximated by the scattering from the ion alone. Figure S5 displays the va-



lidity of this approximation. To quantify the minimal ion occupancy (and maximal water occupancy) in the filter, we introduce effective ion occupancies to account for the possibility that ions and water each partially occupy a binding site. In this analysis we consider a site not fully occupied with  $K^+$  or  $Tl^+$  to be mutually exclusively occupied with water. The effective occupancy  $o_{\text{eff}}$  shown in Tab. 11.2 and 11.3 was hence calculated from the SHELXL refined occupancy  $o_{\text{ref}}$  according to

$$O_{\text{ref}}f^0(K^+) = O_{\text{eff}}f^0(K^+) + (1 - O_{\text{eff}})f^0(H_2O) \quad (5.1)$$

$$\iff O_{\text{eff}} = \frac{O_{\text{ref}}f^0(K^+) - f^0(H_2O)}{f^0(K^+) - f^0(H_2O)} \quad (5.2)$$

a site that is filled 50% of the time with water and 50% with a potassium ion a refined occupancy of 0.75 would be obtained (due to the combined electron density for water and potassium), and an effective ion occupancy of 0.5. Note that if, alternatively, transient vacancies are the reason underlying partial ion occupancies (more in line with our simulation results), the effective occupancies would be identical to the reported refined occupancies. Any effective occupancies larger than 0.5 in adjacent sites are direct evidence for neighboring ions in the selectivity filter.

### Refinement 1r3j

Tab. 11.5 shows the statistics for the data used for refinement of 1r3j in this study. Tab. 11.6 shows the statistics for the anomalous data of 1r3j. The PDB only stores merged data so that some quality indicators such as Rint or data multiplicity are not available. The downloaded model was refined with SHELXL [150] without occupancy refinement for several hundred cycles to ensure convergence. After convergence, the resulting model was refined in SHELXL with individual occupancy refinement for all four  $Tl^+$  ions. Anomalous data was taken into account in all refinement runs. Errors and correlation (Tab. 11.1) between parameters were calculated with SHELXL with one cycle of full-matrix least-squares refinement after removal of any restraints [154].  $Tl^+$  ions were refined anisotropically because this reduces the correlation between occupancy and  $U_{ij}$  from 0.9 to 0.8. The refinement of 1r3j employed 13,073 restraints and 112,104 unique reflections for 17,437 parameters, i.e. a nominal data-to-parameter ratio of 7.2. 5,983 reflections were held back for cross validation. We refined the structure from  $R1 = 33.7\%$ ,  $R_{\text{free}} = 33.7\%$ ,  $wR2 = 65.9\%$  and  $Goof = 6.34$ ; for the deposited structure to  $R1 = 21.0\%$ ,  $R_{\text{free}} = 26.2\%$ ,  $wR2 = 45.8\%$  and  $G_{\text{oof}} = 3.38$ . Note that R-values cannot be compared between different refinement programs so that the reported initial values do not match those reported in the PDB.

### Refinement 3ldc

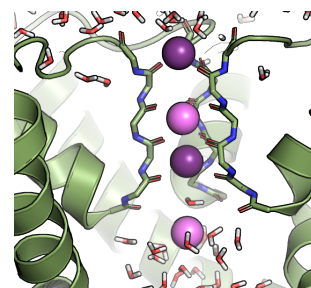
The model for 3ldc (PDB id) was refined with SHELXL analogously to 1r3j. The program ANODE [155] (see also below), revealed that the  $K^+$  ion A5 at site  $S_{cav}$  in 3ldc shows no anomalous signal. It was modeled as  $Na^+$  ion. The refinement of 3ldc employed 2,697 restraints and 27,397 unique reflections for 2,685 parameters, i.e. a nominal data-to-parameter ratio of 11.2. 3,150 reflections were held back for cross validation. We refined the structure from  $R1 = 33.2\%$ ,  $R_{free} = 35.0\%$ ,  $wR2 = 69.7\%$  and  $Goof = 7.29$ ; for the deposited structure to  $R1 = 22.5\%$ ,  $R_{free} = 25.4\%$ ,  $wR2 = 51.9\%$  and  $Goof = 2.42$ . As with 1r3j,  $K^+$  ions were refined anisotropically because this reduces the correlation between occupancy and  $U_{ij}$  from 0.9 to 0.8.

### Refinement 2qks

The structure 2qks (PDB id) was refined with REFMAC5 [156] in addition to SHELXL. This provides results from an additional refinement method. The deposited PDB file contains so-called "LINK" records for the  $K^+$  ions. These are distance restraints to surrounding (oxygen) atoms. Their presence leads to a deviation of the  $K^+$  ions from their special position. After removal of the LINK records, the ions remained in the density on the four-fold symmetry axis. The structure was refined in three rounds. The first round reset the structural model with 100 refinement cycles into convergence according to the modern refinement methods available with REFMAC5. In the second round, occupancy refinement for all  $K^+$  ions was additionally allowed. The refinement resulted in  $R = 19.0\%$  and  $R_{free} = 22.8\%$ . The data consist of 43990 reflections, 2180 of which were retained for  $R_{free}$  cross-validation. The resulting occupancies are listed in Tab.11.4.

In order to see if the results are artificially connected to B-value bias, we carried out a third round of refinement after setting the B-values of all atoms in the model to  $60 \text{ \AA}^2$ , the occupancy of all four  $K^+$  ions in the SF of chain A to 0.2 and their B-values to  $30 \text{ \AA}^2$ . Those in the SF of chain B were (arbitrarily) set to 0.08 ( $K^+$  B408), 0.16 ( $K^+$  B409), 0.32 ( $K^+$  B410), and 0.64 ( $K^+$  B411) and their B-values to  $30 \text{ \AA}^2$ . The results are listed in Tab.11.4. REFMAC5 does not carry out full-matrix least-squares refinement, so that analytical standard deviations are not available. The resulting occupancies are listed in Tab.11.4 as entry 2QKS\*. Although the occupancies together with the B-values are lower, they are considerably greater than 0.5 and thus are consistent with our interpretation of the previous results. The total number of restraints applied by REFMAC5 is 125,801. The model contains 4919 atoms which leads to 19676 parameters plus 8 parameters for the occupancies of the two times four ions in the SF. This results in a nominal data to parameter ratio of 6.4.

For comparison we also carried out refinement with SHELXL with results shown



in the same table. The refinement of 2qks employed 19,768 restraints and 41,810 unique reflections for 19,521 parameters, i.e. a nominal data to parameter ratio of 3.2. 2,180 reflections were held back for cross validation. For this refinement  $R1 = 24.9\%$ ,  $R_{\text{free}} = 30.3\%$ ,  $wR2 = 54.3\%$  and  $\text{Goof} = 6.15$ . These high numbers are due to several unmodelled regions in the electron density which could be due to the detergent or other chemicals used for crystallization. The maximum likelihood method applied in REFMAC5 is more robust under these circumstances. For the SHELXL refinement, the potentially incomplete model, the relatively poor data to parameter ratio, and also the lack of anomalous data are reasons for the large variations in the figures presented in Tab. 11.4. The presented error estimates were calculated without additional restraints, so that the data to parameter ratio equals the number of unique reflections divided by the number of parameters. For the 2qks dataset this gives:  $41810 / 19521 = 2.1$ , whereas for 1r3j this ratio equals  $112104 / 17437 = 6.4$ , and for 3ldc we obtain  $27397 / 2685 = 10.2$ .

### Anomalous peak strength

ANODE [155] was used to calculate the anomalous peak strength in the data for 1r3j and 3ldc. They are listed in Tab. 11.7 for 1r3j and in Tab. 11.8 for 3ldc, respectively. In 3ldc the anomalous signal is weakest for  $S_3$ . Naïvely, this may be interpreted as reduced occupancy, but we would like to offer a different interpretation: If the potential well binding an ion to  $S_3$  is less pronounced due to the nature of the oxygen atoms mimicking a hydration shell, the ion will have greater flexibility and thus fluctuate more strongly. Crystallographically this is expressed as a larger atomic displacement parameter reducing the (anomalous) signal. The relative occupancies for 1r3j were determined with SHELXD. The input file was created with XPREP using default settings and 5000 trials.

### 5.5.3 Brownian dynamics simulations

We designed a simplified permeation model to test whether ion–ion contacts could be a more efficient permeation pattern than ion–water from a fundamental physical point of view. In this simple model, we only considered two physical interactions that are directly related to the knock-on mechanism: electrostatic and van-der-Waals interactions between the ions and water and particles interacting with an external repetitive energy potential describing a model SF. In this way, we constructed a quasi-1D system, which consists of only four  $K^+$  ions, whose motion was restrained on the z-axis by applying two harmonic potentials ( $v=0.5kr^2$ ,  $k=3.0 \times 10^4 \text{ kJ mol}^{-1}\text{nm}^{-2}$ ) on the x and y axes. An external energy potential of the form:



$$V_{ext}(z) = A \cdot \frac{\tanh(z+w) \cdot fs + 1}{2} \cdot \frac{\tanh(z-w) \cdot fs + 1}{2} \cdot \frac{1}{2} \left( \cos\left(\frac{(z-w) \cdot 2\pi p}{2w}\right) - 1 \right)$$

where  $A=15$ ,  $w=0.96$ ,  $p=6$ ,  $fs=1.0 \times 10^4$ , was applied to  $K^+$  to modulate the ion densities to mimic the ion distribution in the filter, as shown in Fig. 5.5 and 5.6. Then, a constant force was applied to the  $K^+$  along the  $z$  direction to model the effect of a trans-membrane voltage. Using the above setup, we performed Brownian dynamics (BD) simulations with the HOOMD-blue software [157] (61 hoomd), to obtain the permeability of the ions under different constant forces (voltage). The electrostatic interaction between ions/water was described by

$$V_{elec}(r) = q_i q_j \frac{\text{erfc}(r_{ij})}{r_{ij}}$$

and the and the vdW interaction was described by

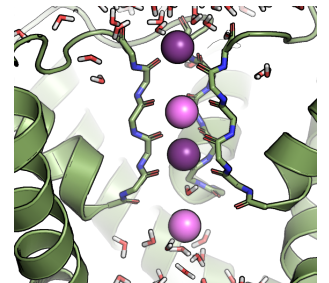
$$V_{LJ}(r) = 4\epsilon \left[ \left(\frac{\sigma}{r}\right)^{12} - \left(\frac{\sigma}{r}\right)^6 \right]$$

The vdW parameters of  $K^+$  were set to be the same as in our MD simulations and taken from either the Dang et al. [145] or Joung et al. [144] parameter set. A time step of 0.01 ps was used for the BD simulations. The simulation temperature was set to 320 K.  $g$  was set to 2720, so that  $K^+$  had a diffusion coefficient of  $0.98 \times 10^{-9} \text{ m}^2 \text{ s}^{-1}$ , about half of its value in bulk water. A dielectric constant of 1 was used for all the BD simulations. For each applied field, six independent 1  $\mu\text{s}$  simulations were performed to yield average conductance and standard deviation. We gradually increased the applied force to model trans-membrane voltages increasing from 0 to 300 mV.

The same procedure was performed for two alternative systems, where in addition to four  $K^+$ , two and four water molecules were added, respectively (Fig. 5.5 and 5.6). The parameters of water were taken over from the rigid SPC/E model.  $g$  of water oxygen and hydrogen were set to 2021 and 126, respectively, so that water had a diffusion coefficient of  $1.27 \times 10^{-9} \text{ m}^2 \text{ s}^{-1}$ , about half of its value in bulk.

## 5.6 Results and discussion

Enabled by the recent availability of  $K^+$  crystal structures with an open gate [37] and methods to simulate ion flux driven by trans-membrane ion gradients [67], we set out to investigate the molecular mechanism of ion transfer across the  $K^+$  channel SF from first principles. We performed atomistic molecular dynamics (MD) simulations of KcsA [Protein Data Bank (PDB) IDs: 3f5w, 3fb7, 1k4c], under



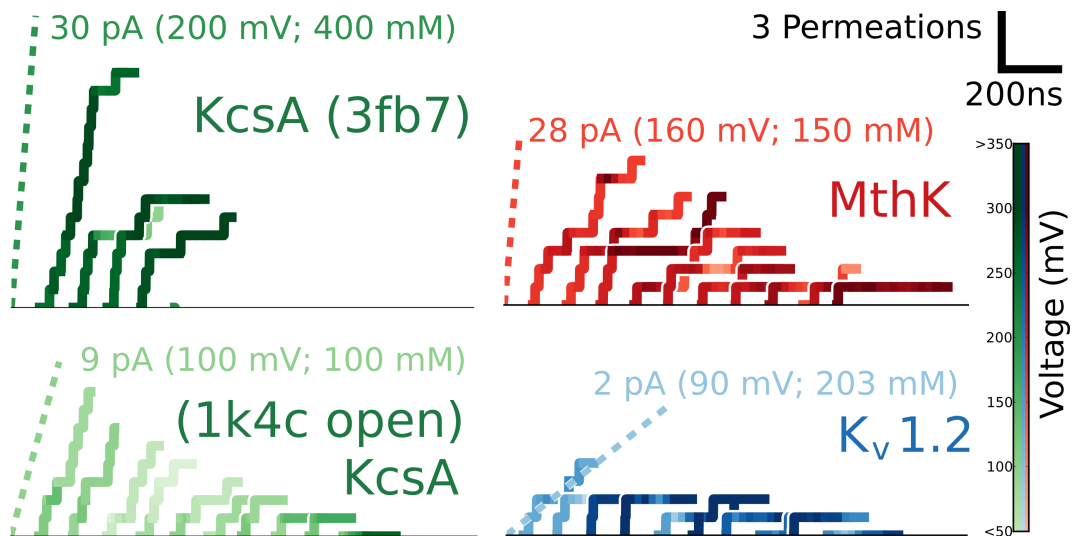
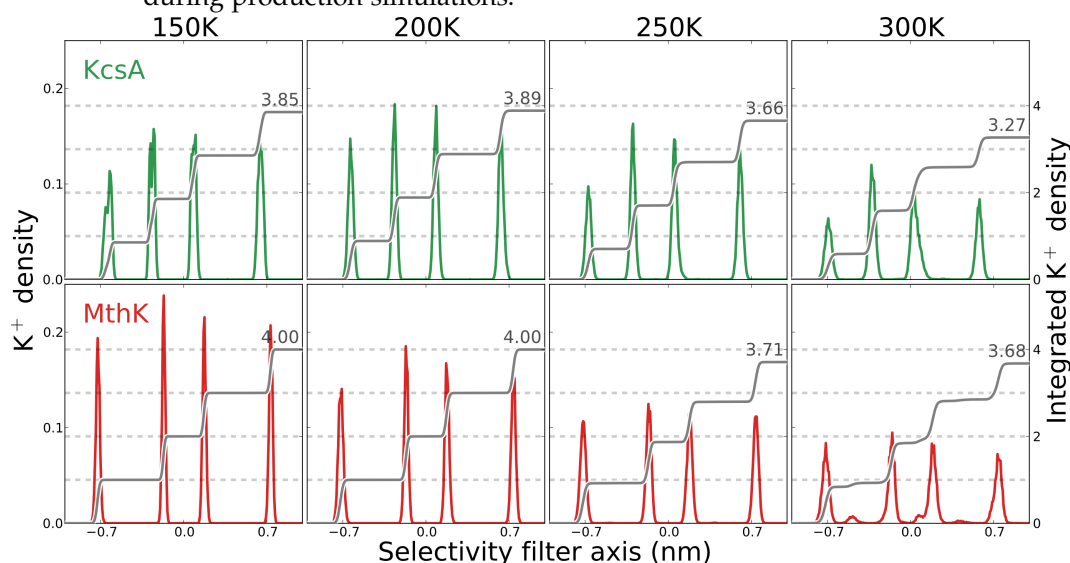


Figure 5.3: **Permeation events as a function of time for different  $K^+$  channels.** Simulations of KcsA (green) started from the crystal structure PDB id 3fb7 (top left, simulation set IX) and a conductive form of PDB id 1k4c that had previously been driven toward an opened state at the bundle crossing in an MD simulation using essential dynamics [143] (bottom left, simulation set XIV). The reported experimental current is displayed as dashed lines [34]. Simulations of the archaeal MthK channel PDB id 3ldc (red, top right, simulation set XV, experimental currents [158]) and the eukaryotic  $K_v$  1.2 channel variant PDB id 2r9r (blue, bottom right, simulation set XVI, experimental currents [38]). Each step represents the permeation of a single  $K^+$  ion, the trans-membrane voltage recorded in experiments or simulations is color-coded as shown in the color bar on the right.

sustained trans-membrane potentials, evoked by  $K^+$  ion gradients, to study the molecular basis of  $K^+$  conduction efficiency in the physiological voltage range (Fig. 5.1C). The simulations were repeated in the archaeal MthK channel from *Methanobacterium thermoautotrophicum* (PDB ID: 3ldc) and the eukaryotic  $K_v$  1.2- $K_v$  2.1 chimeric channel (PDB ID: 2r9r) (Fig. 5.3). In total, we recorded over 1300 spontaneous  $K^+$  permeation events within  $50 \mu s$  simulation time. At KCl concentrations of 400 mM, 200 mM and 10 mM, we recorded the number of permeating ions as a function of time, where the slope of the curves reflects ion current (Fig. 5.1D). The limiting simulated currents under positive potentials are in good agreement with experimentally reported values (up to a factor of 2, similar to the experimental range of variation). We found that sustained currents were restricted to states displaying adjacent  $K^+$  ions in the SF. These invariably involved a  $K^+$  ion pair at binding sites  $S_2$  and  $S_3$  in the SF. One ion bound near  $S_0$ , fre-

quently exchanging with ions from the bulk solution (Fig. 5.1E), such that  $S_1$  was left vacant. Individual outward permeation events were initiated by intracellular  $K^+$  ions entering into the internal channel cavity at binding site  $S_{cav}$ . Translocation of the central ions in the SF at  $S_3$  and  $S_2$  started when a water molecule at  $S_4$  left to generate a vacancy (Fig. 5.1F, G).

Figure 5.4:  $K^+$  ion density (KcsA: green, MthK: red; left axis) and the integration of ion density (grey lines; right axis) along the selectivity filter axis at different temperatures from MD simulations. In the low temperature regime (i.e.  $\leq 200$  K, at crystallization conditions), 4  $K^+$  ions stably bind to the SF of the  $K^+$  channels at a  $[K^+]$  of 400 mM, while an increase in temperature to physiological conditions recovers ionic configurations found in conductive channels during production simulations.



At the core of the permeation mechanism is a fast, concerted motion of the three ions at binding sites  $S_{cav}$ ,  $S_3$  and  $S_2$ , triggered by positional fluctuations of the incoming  $K^+$  ion between  $S_{cav}$  and  $S_4$  (Fig. 5.1H). These motions repeatedly reduce its distance to the ion pair at  $S_3$  and  $S_2$ . A subsequent 'knock-on' between the ion at  $S_4$  and the  $S_3$ - $S_2$  ion pair ultimately leads to a progression of the central ion pair to  $S_2$  and  $S_1$  (Fig. 5.1I), and to further ion transfers from  $S_1$  to  $S_0$  and from  $S_4$  to  $S_3$  (Fig. 5.1J). These final rearrangements complete the transition by re-establishing the initial occupancy pattern of the SF (Fig. 5.1E). We observed the direct knock-on mechanism in simulations of three KcsA crystal structures (PDB IDs: 3f5w, 3fb7, 1k4c), MthK (PDB ID: 3ldc), and the voltage-gated channel chimera  $K_v$  1.2- $K_v$  2.1 (PDB ID: 2r9r), independently of the force fields and water models used (Tab. 5.1, 5.2, and Fig. 5.3).

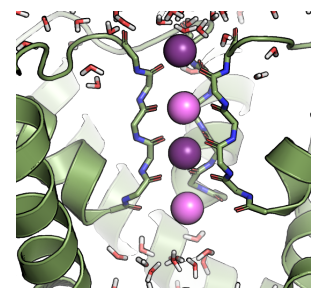
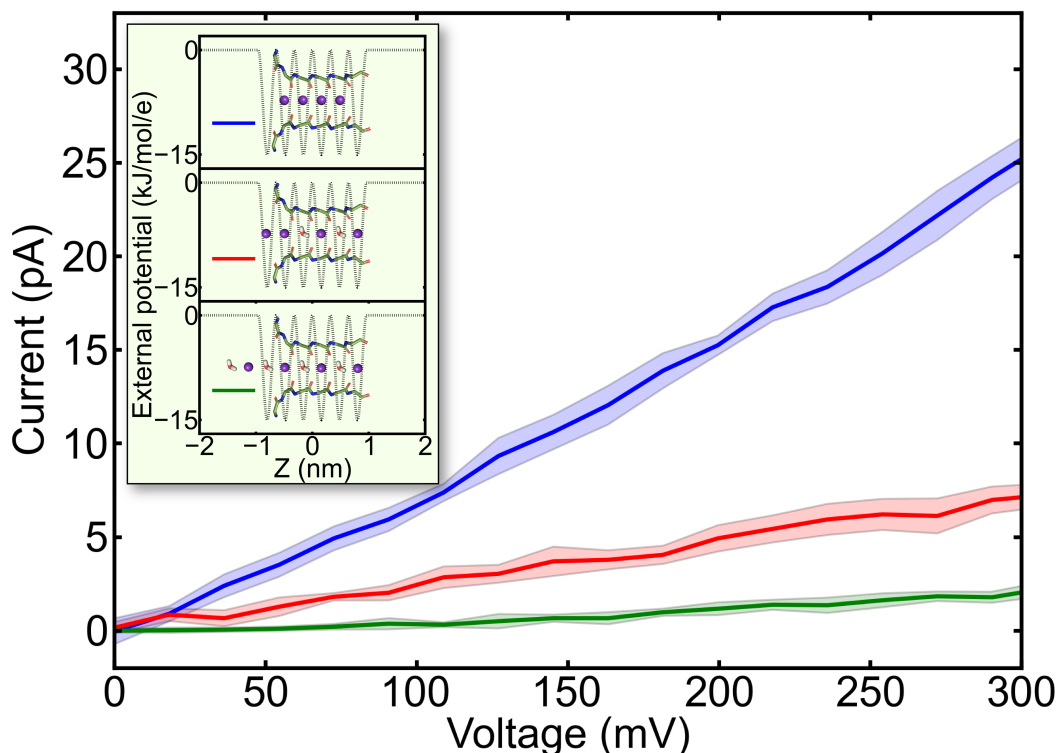


Figure 5.5: **Brownian dynamics diffusion of  $K^+$  ions and water across a repetitive well potential.** Potential energy minima represent ion or water binding sites in the SF (insets). Approximately equal binding site affinity for each species, and hence potential depth, is implicitly assumed in the accepted ion–water co-translocation model. An electric field was applied from left to right. The highest ionic current is seen when  $K^+$  ions are bound in adjacent binding sites (blue line). When direct ion–ion contacts are only occasionally allowed (red line), the current decreases by 80%. The canonical  $K^+$  /water/ $K^+$  /water pattern reduces the maximal current by an order of magnitude (green line).



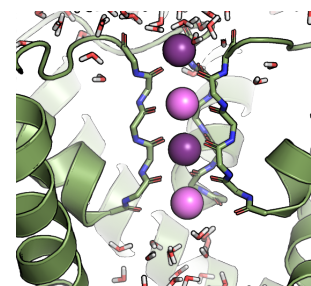
The finding that direct ion contacts underpinned the most efficient  $K^+$  permeation route in  $K^+$  channels in our simulations contrasts with the commonly accepted transport mechanism, based on alternating ion/water occupation inside the SF. Similar direct cation–cation contacts have so far mainly been detected in concentrated salt solutions [159]. The accepted mechanism has predominantly been inferred from channel crystallographic data, among which the anomalous data of  $Tl^+$  ions in the KcsA SF (PDB ID: 1r3j) played a particularly important role [132]. We were, therefore, interested in whether our results are compatible with the experimental data. As the original interpretation of the anomalous electron density map may contain potential drawbacks such as a degree of dependence

on the quality of the refined model from which phases are calculated, we used the program SHELXD [151] to determine  $Tl^+$  occupancies in KcsA solely against anomalous data. This analysis established the relative occupancies to be equal between all four ions within experimental error. The absolute occupancy was refined by SHELXL [151], as listed in Tab. 5.3. In addition,  $K^+$  occupancies were refined for MthK (PDB ID: 3ldc, [18]) and Kir3.1 (PDB ID: 2qks, [160]; see Tables 5.3, 11.2 and 11.3). We consistently find high values close to unitary occupancy that are consistent with the interpretation that close contacts between alkali ions occur in the SF. These contacts were identified as key for efficient conduction in our MD simulations. Water molecules do not seem to be necessary to separate alkali ions in the filter in order to shield them from repulsion. As previously suggested, and as directly observed in our simulations under trans-membrane voltage, ion conduction in  $K^+$  channels ‘in action’ relies on frequent transitions between substates of different ion occupation, whereas open-activated channel states under crystalline conditions are thought to be characterized by the presence of electron density at all four SF positions (31). Accordingly, without applied voltage and at reduced temperature, the SF occupancy seen in our simulations converges to that observed in the crystal structures (PDB IDs: 1k4c, 3ldc) (Fig. 5.4).

Table 5.3: **Occupancy refinement of  $Tl^+$  in the KcsA structure PDB ID 1r3j and  $K^+$  in the MthK structure PDB ID 3ldc, respectively.** The absolute occupancy (abs. occ.) was determined with SHELXL, which allowed for an estimation of the absolute error. Values greater than one are caused by the correlation between occupancies and B-values. As an independent cross-validation we calculated the relative occupancies (rel. occ.) based solely on the anomalous signal using SHELXD.

Binding site	KcsA, PDB ID: 1r3j refinement of $Tl^+$			MthK, PDB ID: 3ldc refinement of $K^+$	
	res. id	abs. occ.	rel. occ	res. id	abs. occ.
S <sub>1</sub>	C401	$1.02 \pm 0.04$	1.0	A1	$0.92 \pm 0.07$
S <sub>2</sub>	C402	$0.93 \pm 0.03$	0.9	A2	$0.80 \pm 0.07$
S <sub>3</sub>	C403	$0.92 \pm 0.04$	0.9	A3	$1.00 \pm 0.09$
S <sub>4</sub>	C404	$0.99 \pm 0.04$	1.0	A4	$1.00 \pm 0.09$

We next investigated whether the basic physical principles of ion translocation in single file predetermine close ion-ion contacts to drive efficient permeation. We modeled the fundamental ion translocation event as diffusion in a periodic one-dimensional potential, reflecting the sequence of ion/water binding sites in the SF (see Fig. 5.5). By testing various occupation patterns and a range of membrane voltages, we found that configurations with direct contacts between ions consistently gave rise to markedly higher transfer rates than water-separated patterns.



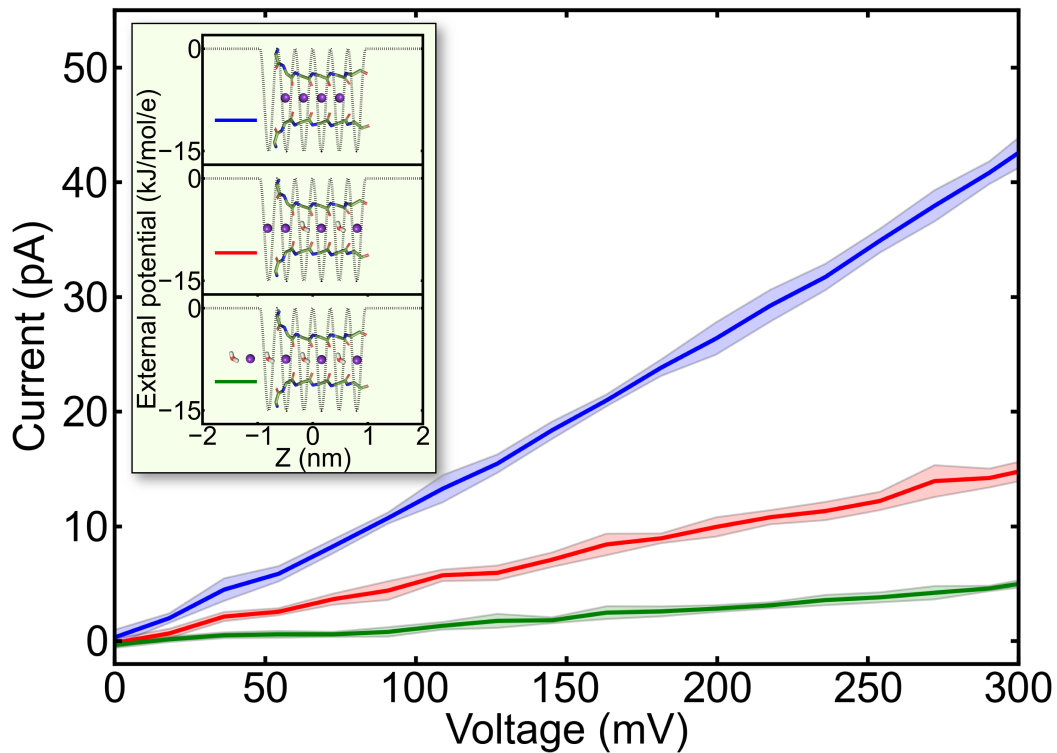


Figure 5.6: **Control Brownian dynamics simulation with ion parameters taken from Dang et al. [145]** Qualitatively, the same results were obtained as in Fig. 2, where Joung et al. parameters were used [144]. Direct ion contacts lead to the highest conductance while the presence of water molecules suppresses conduction.

These results were independent of the ion and water models used and of the details of the potential (see Fig. 5.6). Under physiologically relevant voltages, fully ion-occupied systems showed a conductance of around 80 pS, whereas those with alternating ion–water occupancy displayed only little permeation, further decreasing with increasing water content (Fig. 5.5). Hence, a simple physical model of ion transfer through a confined pore with multiple binding sites already predicts ion–ion contacts to enhance, and the presence of uncharged species to impede, ion permeation.

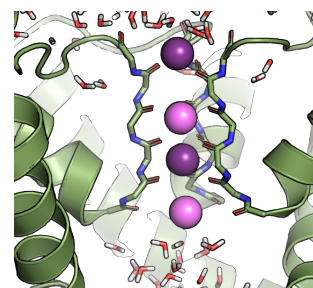
Together with the results from our MD simulations, the data suggest that water is not co-translocated with  $K^+$  to a large degree in functional, open-activated KcsA. This is seemingly in conflict with the ion:water co-transport ratio derived from measurements of water translocation through KcsA [45,161–163]. However, these experiments were based on the application of high osmotic gradients. Water per-

meation as a result of an applied osmotic pressure is likely to lead to ion-depleted SF states in which only occasionally, individual ions are dragged along by permeating water molecules, while bound ions are reported to completely block water flux [162,163]. Such ion-depleted, and water-permeable, filter states are therefore markedly different from the ion-conductive states at higher ion occupancy considered crystallographically and in our MD simulations. The authors of this study explicitly state that their model is only valid in the absence of direct ionic contacts, which is not the predominant scenario we observed. In addition, it has been shown that substantial water flux through KcsA occurs mainly in its inactivated, non-K<sup>+</sup> conductive state [45,162,163], while co-translocation of water is below the detection limit in its open-activated state in K<sup>+</sup> concentrations above 200 mM.

The agreement between the multiple approaches we used to study ion flux in K<sup>+</sup> channels suggests a consensus mechanism of ion permeation across the SF. Figure 5.7 displays a schematic potential landscape in the SF according to the main observations made in our simulations (Fig. 5.7A, gray). In the resting state under physiological membrane voltage, two K<sup>+</sup> ions bind stably to S<sub>2</sub> and S<sub>3</sub> (Fig. 5.7A, purple). The height of the energy barrier (red) prevents transfer of K<sup>+</sup> from S<sub>2</sub> to S<sub>1</sub>. As K<sup>+</sup> enters into S<sub>4</sub>, Coulomb repulsion with the central ions leads to their relative energetic destabilization (Fig. 5.7B). This Coulomb interaction also lowers the permeation barrier between S<sub>2</sub> and S<sub>1</sub> (Fig. 5.7C). As a result, productive translocation of the ion at S<sub>2</sub> can occur (Fig. 5.7D). Subsequently, translocation from S<sub>3</sub> to S<sub>2</sub> lowers the potential energy of the ion at S<sub>4</sub>, while, simultaneously, the energy of the ion at S<sub>1</sub> is increased (Fig. 5.7E, red arrows). Owing to the new potential energy surface, the initial ion configuration is then recovered by transfer from S<sub>4</sub> to S<sub>3</sub> and exit of the ion at S<sub>1</sub> from the SF (Fig. 5.7F). This cycle constitutes a full conduction step. Notably, the free energy required to destabilize binding at S<sub>2</sub> ultimately stems from the binding energy of the incoming ion, best seen during the transition of the central ion (Fig. 5.7E, red arrows).

## 5.7 Conclusion

The proposed mechanism predicts an important experimental characteristic of K<sup>+</sup> channels. As the rate of K<sup>+</sup> ions leaving the SF at the extracellular side is determined by the rate with which incoming intracellular ions arrive at the filter (see flip-book at the right bottom side of this thesis), our model inherently implies K<sup>+</sup> channels to be diffusion-limited as long as an ion pair occupies the inner SF binding sites. We therefore recorded the occupancy of the inner SF sites under varying K<sup>+</sup> concentration. Indeed, we found that ions occupy these positions over a broad range of concentrations from 10mM to 400 mM (Fig. 5.8). Taken together, our model thus not only accounts for the diffusion control of K<sup>+</sup> channels, but



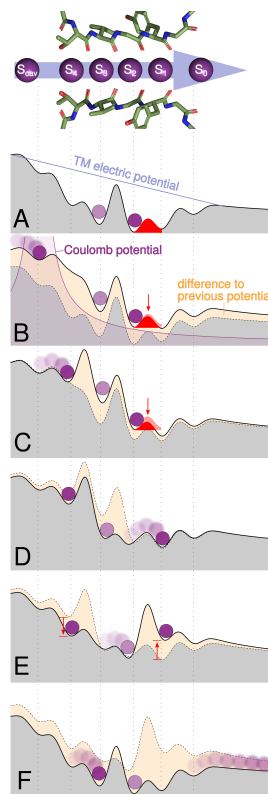


Figure 5.7: **Energetic basis and mechanism of ion permeation in the KcsA selectivity filter.** (A) Potential landscape (gray) of the steady-state situation with  $K^+$  simultaneously bound in  $S_2$  and  $S_3$  (purple) and a trans-membrane (TM) electric potential attracting cations toward the extracellular face (blue). (B) An incoming  $K^+$  ion binding to  $S_{cav}$  alters the potential of the ions at  $S_2$  and  $S_3$  as a result of Coulomb repulsion (magenta), raising their free energy with respect to the bulk and lowering the barrier for the ions at  $S_3$  and  $S_2$ . (C and D) Subsequent binding of the incoming ion to  $S_4$  (C) finally reduces the barrier sufficiently for the ion at  $S_2$  to advance to  $S_1$  (D). (E) The strong destabilization of the ion at  $S_1$  is simultaneous with an increase in stabilization of the incoming ion at  $S_4$  (red arrows), triggered by the transfer of the central ion to  $S_2$ . (F) In the last step, the ion at  $S_4$  binds to  $S_3$  while the ion at  $S_1$  leaves the SF, thereby recovering the original state.

also explains the wide linear regime of  $K^+$  channel conductance above 10 mM  $K^+$  concentration [41], which is a prerequisite for robust  $K^+$  channel function under variable external conditions. Summarizing, we propose a new model for ion transfer in  $K^+$  channels at physiological voltages. Our permeation model relies on repulsive Coulomb interactions between adjacent ions in the SF as the main driver for conduction near the diffusion limit, as illustrated in Fig. 5.7. In reinvestigat-



ing several  $K^+$  channel structures, we found direct ionic contacts to be compatible with the available crystallographic data. The results presented above demonstrate that these direct contacts are not energetically prohibitive. Rather, they serve to enhance ion flux to the maximum attainable speed over a broad range of concentrations.

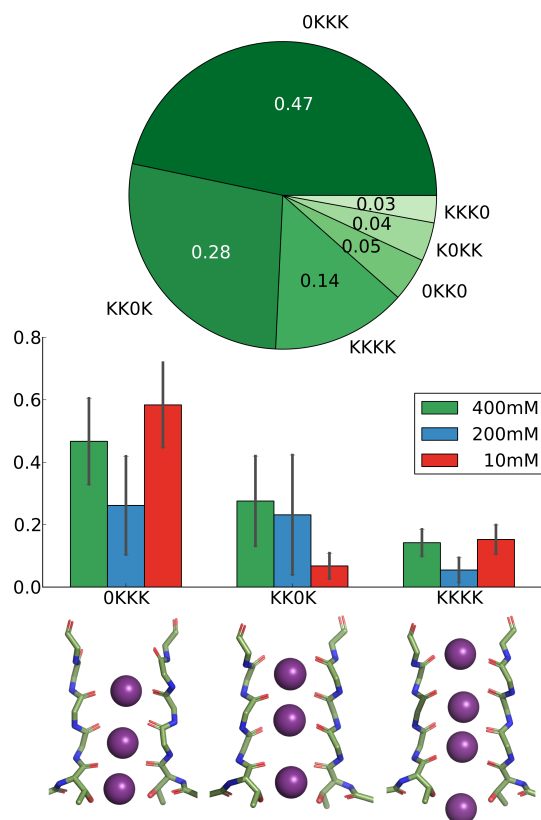
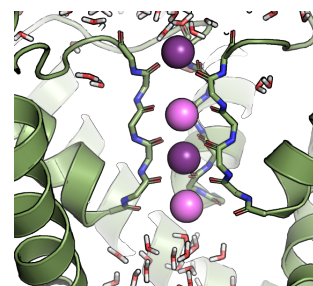


Figure 5.8: **Population of ionic configuration states in the selectivity filter.** Top panel: Pie chart of all observed states with a population  $> 0.02$  in KcsA simulations of set I (400 mM; 200 mV), the naming of states corresponds to  $K^+$  ion binding at sites  $S_1$  through  $S_4$ , 0 denotes a vacancy. Middle panel: Population distribution as a function of concentration of the three most populated states. The majority of states contain direct ion-ion contacts under all investigated concentrations. Bottom panel: Representative SF snapshots of the three most populated states. Independent of the ion concentration the two most populated states account for about 60% of all ion configurations. The lower current due to the smaller number of ions arriving at the cavity at lower ion concentrations explains the increasing trend of 0KKK and decreasing trend of KKOK with reduced concentration.



## 5.8 Acknowledgments

We thank Han Sun and Sören Wacker for simulations of  $K_v$  1.2 and Rastko Sknepnek for assistance with HOOMD-blue. We are grateful to Helmut Grubmüller, Mark Sansom, Timo Graen and Kornelius Zeth for helpful discussions. DK is supported by the International Max Planck Research School for Biology and Complex Systems. CS is supported by a Marie Curie Intra-European Fellowship. TG is supported by the “Volkswagen Stiftung” via the Niedersachsenprofessur awarded to GMS. UZ acknowledges funding from the Scottish Universities’ Physics Alliance.

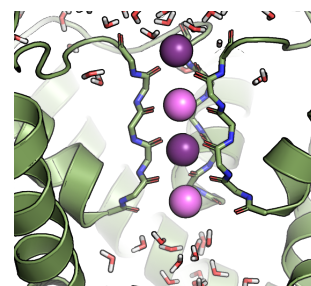
## 6. Selectivity Filter Flexibility is Essential for the K<sup>+</sup> Channel Permeability

### 6.1 Introduction

Potassium (K<sup>+</sup>) channels are essential to all kingdoms of life as they mediate cell homeostasis and active processes such as nerve signaling. The core structural element of these membrane integral, tetrameric proteins is the highly conserved selectivity filter (SF). It constitutes the narrowest pathway at the interface of the four subunits towards the extracellular side of the channel, through which the ions can only pass in a single file stripped of their water shell (see Fig. 6.1). In the widely used prokaryotic K<sup>+</sup> channel KcsA, the SF is composed of four parallel stretches of the 4 amino acids Thr75, Val76, Gly77 and Tyr78, suspended by the small  $\alpha$ -helical pore-helices (PH) and embedded into a complex network of hydrogen bonds. The backbone carbonyl-oxygen atoms of the SF-forming amino acids face in towards the channel lumen where they form layers between the four corresponding amino acids which mark the borders of the K<sup>+</sup> binding sites S<sub>0</sub> to S<sub>4</sub>.

The SF's function in the channel is two-fold: 1) it serves as gate, that in response to voltage and current closes the channel, a process called C-type inactivation [37, 45, 53–55] and 2) implements the channel's ion specificity of K<sup>+</sup> over other physiological relevant ions such as Na<sup>+</sup>, while at the same time, achieving permeation rates close to the diffusion limit [1, 39, 164–168]. Both these functions have been the focus of mutation studies, MD simulations, and crystallographic assays, but their mechanistic nature still remains a topic of broad discussions.

Along with the first resolved crystal structure of the bacterial K<sup>+</sup> channel KcsA in 1998, a first structure based model for the K<sup>+</sup> ion selectivity was proposed [15]. Doyle and collaborators proposed the "snug fit" model from the observation that the SF backbone carbonyl-oxygen atoms coordinate the bound K<sup>+</sup> ions at the same distances as the water shell for K<sup>+</sup> found in bulk water. In this model, it was proposed that the SF carbonyl moiety distances would be suitable only for ions with an atomic radius like K<sup>+</sup>, whereas the coordination of larger or smaller ions



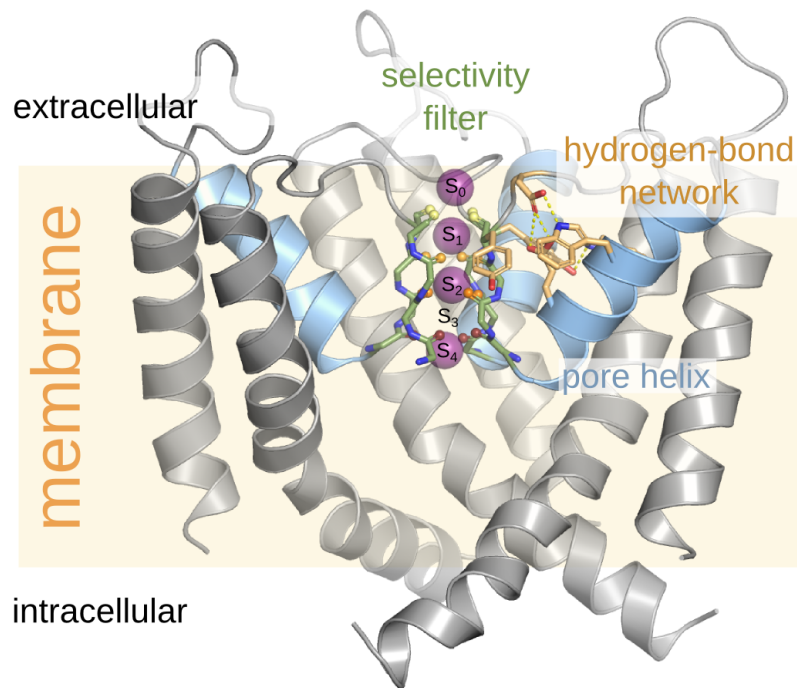


Figure 6.1: **Structure of the open KcsA K<sup>+</sup> channel.** For clarity, only three subunits of the tetramer are shown. The SF (green) is formed by layers of backbone carbonyl-oxygen atoms (yellow to red spheres) facing inward onto the channel axis. In between these carbonyl-layers (orange colors), lie the K<sup>+</sup> binding sites S<sub>0</sub> to S<sub>4</sub>, where the K<sup>+</sup> ions (purple spheres) bind. The SF is supported by the pore helices (blue) and supported by a network of hydrogen bonds (yellow).

would be less favorable and therefore prevent their passage by a high energetic barrier.

The "snug fit" was questioned on the grounds that both the temperature factors in the crystal structure [15] and MD simulations [23] showed thermal fluctuations of the SF on the Ångström length scale. These fluctuations are larger than the coordination distance difference in bulk water between K<sup>+</sup> and Na<sup>+</sup> ( $\Delta d = 0.4 \text{ \AA}$  [169]) and therefore selection by a pure distance criterion seemed unlikely. In a systematic MD study, Noskov et al. probed how limiting these thermal fluctuations would alter the selectivity of K<sup>+</sup> channels. Using free energy perturbation with MD simulations, they found, contrary to the idea of the "snug fit" model, that decreasing the flexibility and therefore enforcing the exact distances renders the SF less specific for K<sup>+</sup> ions.

Here, we revisit the question how the flexibility of the SF is relevant to the function of the K<sup>+</sup> channel. First, we will look into the motions of the SF during

spontaneous permeation of  $K^+$  ions during unrestrained MD simulations to understand the motions associated with ion permeation. In a second step we will test how limiting the flexibility influences the channel conductance. Finally, we will assess the changes inflicted by the limited flexibility to gain insights into the role of the SF during the permeation process.

## 6.2 Methods

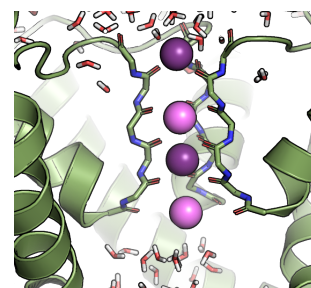
### 6.2.1 Simulation setup

The system was prepared by inserting the KcsA crystal structure with a fully opened gate (PDB id: 3F5W) into a system with 216 palmitoyl-oleoyl-glycero-phosphocholine (POPC) lipids, 14526 water molecules, 156  $K^+$  ions, and 160  $Cl^-$  ions (400 mM KCl) using the program `g_membed`. The collapsed SF region ("TTV-GYG") of 3F5W was replaced by the ordered structure found under high  $[K^+]$  (PDB id: 1K4C) with  $K^+$  ions located at the binding sites  $S_0$ - $S_{cav}$ . The N- and C-terminal ends of the protein were capped with N-methylamide and acetyl moieties, and the last four amino acids of either end of the  $\alpha$ -helix were kept from unraveling by strengthening the hydrogen bonds of the secondary structure with additional harmonic restraints. The system was equilibrated for 100 ns with position restraints ( $1000 \text{ kJ mol}^{-1} \text{ nm}^{-2}$ ) on all heavy atoms of the protein and the  $K^+$  ions bound to the SF. Afterwards, the system was doubled along the Z axis to yield a double membrane system where an ionic imbalance of  $2e^-$  was maintained using the computational electrophysiology setup [67] which gave rise to a trans-membrane voltage of about 200 mV.

The simulations were carried out using the MD simulation program Gromacs 4.6 [84] with the computational electrophysiology extension [67] using the AMBER99sb [78] force field with the SPC/E water model. All bonds were treated with the LINCS algorithm [76] and virtual-sites were used for all hydrogen atoms [77], allowing for an integration time step of 4 fs. Parameters for the lipids were chosen according to Berger et al. [110]; parameters for the ions were chosen according to Joung et al. [144]. Temperature and pressure were kept constant at 310 K and 1 bar by the *v*-rescale thermostat [86] and the Berendsen barostat [85], respectively. To prevent the channel from closing at the lower helix bundles, an additional distance restraint between all pairs of S5 helix bundles was introduced according to the distance in the open crystal structure (PDB ID: 3F5W) [37].

### 6.2.2 Restraining the flexibility

The flexibility of the SF was restrained by a harmonic position restraint on the main chain atoms (C,  $C_\alpha$ , N, O) of the SF-forming residues Thr 74 to Gly 79. Two



position restraint reference structures were obtained from the crystal structure under high  $K^+$  concentration (PDB id: 1K4C [15]) and by averaging and symmetrizing the structure of the SF during unrestrained simulations.

### 6.2.3 Determining the electrical properties from the MD simulation

The trans-membrane potential  $\Phi$  was determined numerically by twice integrating the Poisson-equation  $\Delta\Phi = -\rho/\epsilon_0$  over the time averaged charge distribution  $\rho$  along the z-axis. Due to accumulating numerical errors, these calculations typically show an offset between the top and the bottom of the simulation box despite the equality of the potential at these points given by the periodic boundary conditions.  $\Phi$  was therefore corrected by subtracting the linearized offset. From  $\Phi$ , the trans-membrane voltage was calculated by taking the difference between the potential in the bulk water phase of compartment A and B. The current was calculated by counting the number of permeating ions ( $\Delta N$ ) during the time  $\Delta t$  of the MD simulation. As the simulation contained only monovalent ions, the current can be calculated as  $I = \frac{\Delta N e^-}{\Delta t}$ , with  $e^-$  as the elementary charge.

## 6.3 Results and discussion

### 6.3.1 SF flexibility during spontaneous ion permeations

Using an open conductive structure of the prokaryotic KcsA channel, combined with a protocol for simulating electric gradients, we were able to simulate many spontaneous  $K^+$  permeation events (as presented in chapter 5). In 20 independent unrestrained simulations (15  $\mu s$  total simulation time), we observed about 500 spontaneous transitions of  $K^+$  ions at a trans-membrane voltage of 200 mV.

We focus our analysis on the backbone carbonyl-oxygen atoms of the SF-forming residues Thr 75, Val 76, Gly 77, and Tyr 78 that separate the  $K^+$  binding sites  $S_0$  to  $S_4$  (see Fig. 6.2A). These carbonyl-oxygen atoms constitute the narrowest passage in the ion pathway and—due to their strong partial charge of  $-0.5e^-$  (as parametrized in the standard amber99sb force field)—strongly interact with the bound  $K^+$  ions. We monitored the distance of each carbonyl-oxygen from the ion pathway axis, which can be regarded as the pore radius at that point, where the ions have to “squeeze through” to advance from one binding site to the next (see Fig. 6.2). Figure 6.2B shows a jump in the distance around the time of an  $K^+$  ion permeation event (black lines for individual events, orange colored lines for the average). On average this jump is very subtle, on the order of about 0.2 Å, but it significantly correlates with the time of the permeation event (see histograms in Fig. 6.2B).

When we compare the average radii before the permeation event with the situation after the permeation event, we find the extracellular most layers of Tyr 78 and

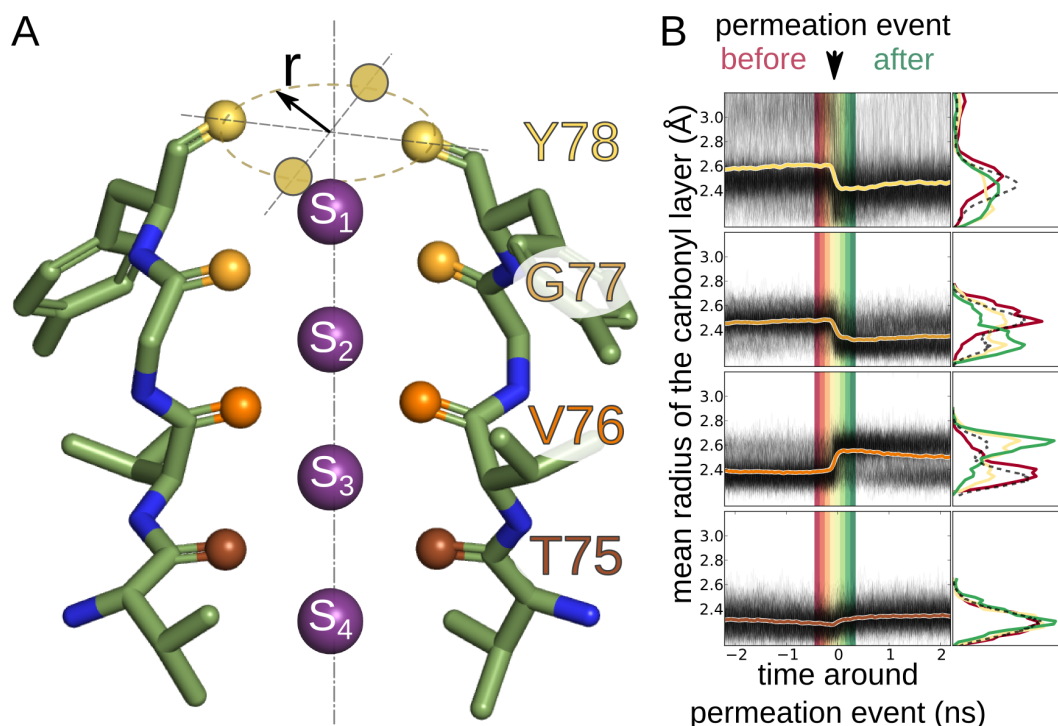
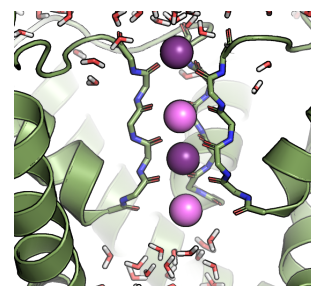


Figure 6.2: Mean radius around the time of an ion permeation for each SF backbone carbonyl-oxygen layer. (A) Structure of the SF-forming residues (only two of the four strands are shown) with indication of the interspersed binding sites  $S_0$ - $S_4$  for  $K^+$  ions (purple spheres). The backbone carbonyl-oxygen atoms for each layer are highlighted by red to yellow spheres. For the layer of Tyr78 the construction of the mean radius is indicated. (B) The mean radius of all  $\sim 500$  permeation events (thin black lines) and the overall average (thick red to yellow lines) for the corresponding residue centered around the permeation event. Histograms to the left side show the distribution of the radii over all times (black broken line), before the permeation event (red), directly at the permeation event (yellow) and after the permeation event (green).

Gly77 to tighten and Val76 to widen. In contrast, the radius of Thr75 remains almost constant over the whole process, but reaches a distinct minimum at the time of permeation. The distribution of those radii (black dashed lines in Fig. 6.2B) display a bimodal distribution for the carbonyl-layers formed by Gly77 and Val76, indicating two distinct states. These two states correspond exactly to the configuration found just before the permeation event (red distributions), where Val76 is narrow and Gly77 is widened and right after the permeation event, where the width of these radii inverts (green distributions). From the height of these bimodal distribution, we learn that the SF spends most of its time in the state prior to a per-



meation. This observation is in agreement with the notion of the diffusion limited channel, in which the diffusion of  $K^+$  ions to the SF is slower than the transition itself, such that the channel spends most of its time “waiting” for an ion to arrive.

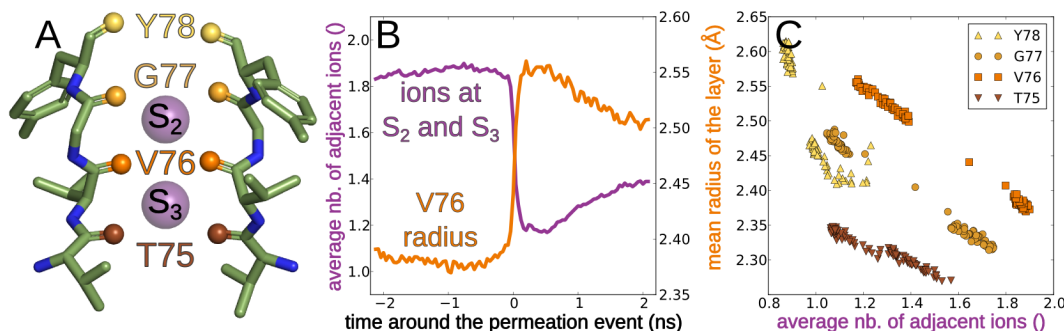


Figure 6.3: **The average radius of each carbonyl-layer strongly correlates with the number of adjacent ions.** (A) Structure of the SF with the carbonyl-oxygen layers colored in yellow to red and ions bound around Val76 to S<sub>2</sub> and S<sub>3</sub> indicated by purple spheres. (B) The average carbonyl-oxygen radius (orange) and number of adjacent ions at S<sub>2</sub> and S<sub>3</sub> plotted for the example of Val76 show a strong correlation. (C) plotting the number of adjacent ions against the mean carbonyl radii for all carbonyl-layers shows the same correlation—the more surrounding ions the smaller the average radius.

The tightening of the carbonyl-oxygen layers during ion permeation contradicts a simple picture in which the ions need to squeeze through the tightest constriction in the channel. In such case, one would expect a brief widening as the ions pass, quickly relaxing into the resting position. To explain the observed shifts in the radius, we looked at the interactions of the layers with neighboring ions. Figure 6.3B shows how the total number of adjacent ions at S<sub>2</sub> and S<sub>3</sub> (see Fig. 6.3A) changes over the course of a permeation event (purple line) for the example of Val76. This average number of adjacent ions is directly correlated with the average radius of the layer. This observation holds for all of the SF-forming amino acids as shown in Fig. 6.3C. This result suggests that the carbonyl-oxygen atoms do not need to move aside; on the contrary, they are forced between the extremely close and highly charged  $K^+$  ions.

To fully understand the concerted changes of the radii during ion permeation, we must look at the average permeation event. Such a typical permeation event has been described in chapter 5 in Fig. 5.1, where the actual fast translocation of the ions is depicted in panels I and J. Figure 6.4 shows the typical ion configuration before and after this major transition of the ions. As discussed above, the key to understanding the radius changes lies in the number of surrounding  $K^+$  ions. Before the permeation event, sites S<sub>2</sub> and S<sub>3</sub> are occupied, while S<sub>1</sub> and S<sub>4</sub> are vacant.



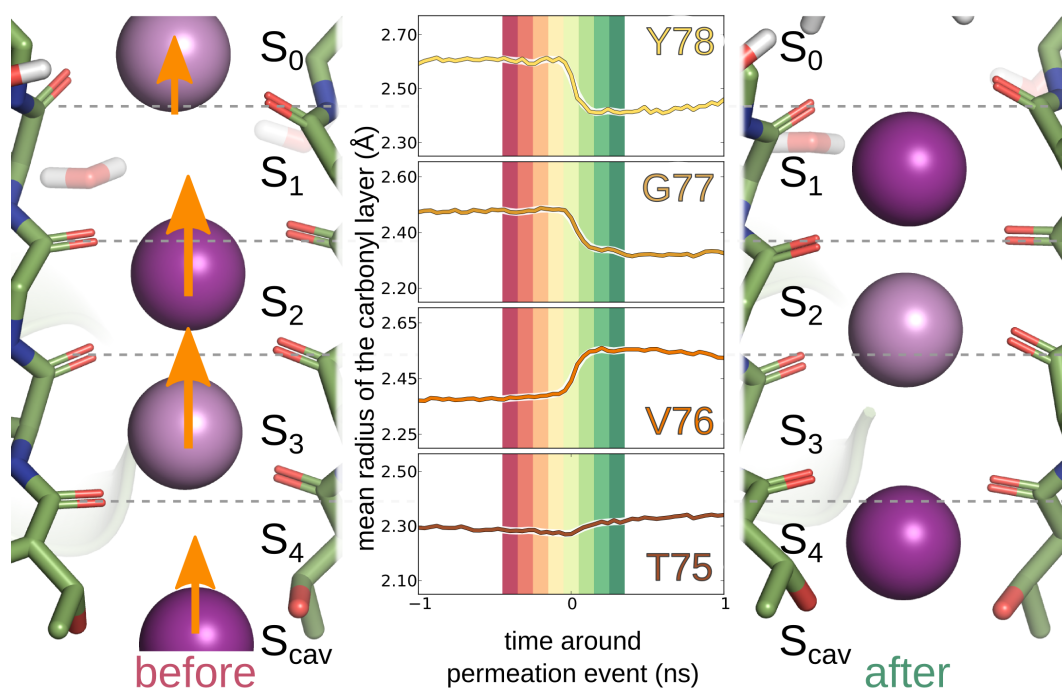
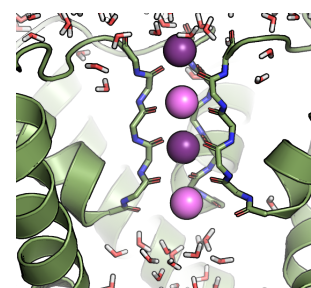


Figure 6.4: **The concerted changes in the carbonyl-layer radii can be understood in light of the ionic configuration changes during a typical permeation event.** The left structure depicts the situation before the permeation event, the right structure after the permeation event. The central panel shows the average changes of the carbonyl-layer radii during the permeation event.

This ionic configuration is stabilized by the negatively charged carbonyl-oxygen atoms of Val76 moving inwards between the central ion pair. This configuration leaves the carbonyl-oxygen atoms of Thr75 and Gly77 adjacent to only one  $K^+$  ion at  $S_3$  and  $S_2$ , respectively. For Tyr78 we often find an ion bound to the extracellular binding site  $S_0$ , which frequently exchanges with the bulk. This exchanging ion has Tyr78 surrounded by one ion most of times, but also gives rise to occasional configurations without direct ionic contacts.

The fast step of the typical permeation event is triggered by an ion from the cavity binding to  $S_4$ , advancing the centrally bound ions to  $S_2$  and  $S_1$  as shown in Figure 6.4. This configuration shows Gly77 surrounded by two ions, which consequently leads to a contraction of the carbonyl-layer radius, whereas Val76 is left with only one adjacent ion at  $S_2$  and therefore the carbonyl-layer radius widens. The almost unaltered average radius of Thr75 agrees with the constant number of one neighboring ion at the adjacent binding sites. Before the permeation event one ion is typically bound to  $S_3$  just above this layer, whereas after the permeation



event we find one ion bound below the layer at  $S_4$ . At first glance the situation of Tyr78 should be similar to that of Thr75. However, here we find the largest discrepancy between the radius before and after the permeation event. This effect goes back to the weak binding of ions to  $S_0$  at high positive membrane potentials. Ions bound to  $S_0$  prior to the permeation event are partially solvated and show frequent exchange with the bulk. This weak binding reduces the average occupancy of  $S_1$  as well as the average distance of the ion from Tyr78, which in turn widens when no ions are present. In contrast, the ion bound to  $S_1$  right after the permeation event is sharply localized causing the Tyr78 carbonyl-layer to constrict.

### 6.3.2 Effects of artificially restraining the SF flexibility

Having quantified the changes occurring during spontaneous ion permeation, we tested whether these subtle changes in the sub-Ångström regime have an impact on the  $K^+$  channel's main function, the conductance of  $K^+$  ions. Using the Computational Electrophysiology setup, we added a series of harmonic restraints on the SF main chain atoms. To reduce bias, we used two different references for the position restraints as shown in Fig. 6.5A: the crystal structure with the ordered conformation of the SF (PDB id: 1K4C, green structure) and the average, symmetrized structure of the SF over all free simulations (blue structure). In total, we ran  $40\mu s$  (2 references  $\times$  6 independent simulations  $\times$  7 restraint strengths  $\times$  450 ns of simulation time) and recorded about 500 permeation events.

The restraint effect on the SF flexibility is depicted exemplarily for Val76 for the unrestrained case as well as for a medium and strong restraint in Fig. 6.5B. As expected, we find an increasing localization of the carbonyl moiety both axially and laterally. To quantify the flexibility, we calculated the root mean square fluctuations (RMSF) of all SF-forming backbone carbonyl-oxygen atoms as a function of the restraint strength, as shown in Fig. 6.5C. Up to a restraint strength of  $100\text{ kJ mol}^{-1}\text{ nm}^{-2}$ , the flexibility shows no strong deviation from the flexibility observed during free simulations (black solid line: average, broken line: SEM). Beyond  $200\text{ kJ mol}^{-1}\text{ nm}^{-2}$ , we observe an approximately linear decrease in the RMSF with the force constant of the restraint. The strongest restraint of  $1600\text{ kJ mol}^{-1}\text{ nm}^{-2}$  reduces the flexibility of the free system by about 2/3. However, in absolute numbers the difference is only  $0.15\text{ \AA}$ .

Despite these very subtle effects on the order of a tenth of an Ångström, the effects on the channel conductance are remarkable as shown in Fig. 6.5D: In the regime beyond  $200\text{ kJ mol}^{-1}\text{ nm}^{-2}$ , where we found a linear decrease in the flexibility, we also find a gradual decrease in conductance that almost reaches zero at around  $800\text{ kJ mol}^{-1}\text{ nm}^{-2}$ , independent of the reference structure. Notably, we also

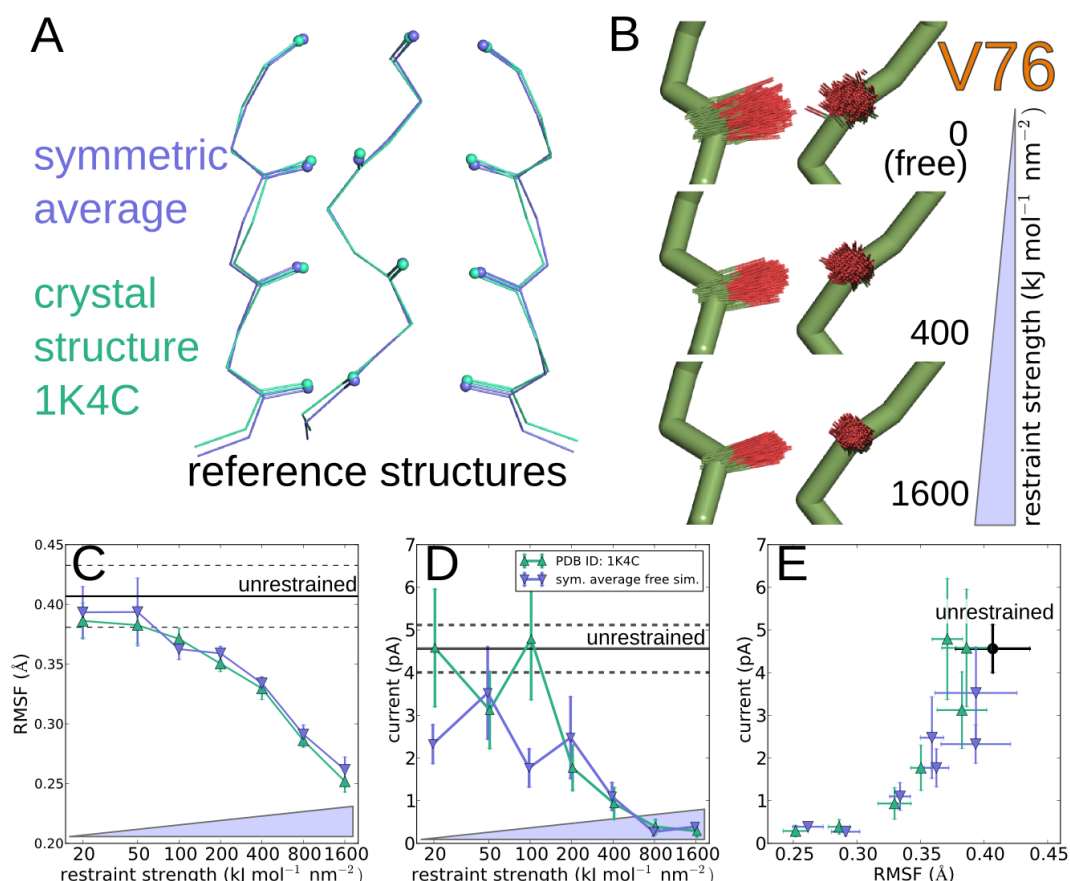
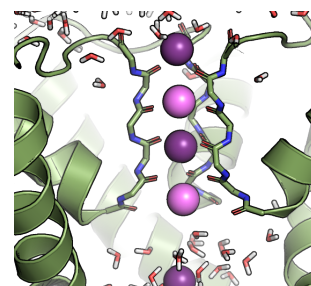


Figure 6.5: Position restraints on the main chain atoms of the SF are used to restrict the flexibility of the SF. (A) Reference structures used for the position restraint: crystal structure of the ordered conformation (PDB id: 1K4C, green) and an averaged and symmetrized structure from the unrestrained simulations (blue). (B) Carbonyl-oxygen atom positions of 300 randomly chosen structures of to neighboring Val 76 at different restraint strengths. (C) Harmonic restraints have a direct impact on the average RMS fluctuations of all SF-forming backbone carbonyl-oxygen atoms. Errors are given as SEM from all independent simulations. (D) The relation between the restraint strength and the observed current. (E) Relation between the carbonyl-layer fluctuations and the observed currents.

find an unusually low conductance for simulations with low restraints towards the symmetrized average structure of the free simulations. As we have seen that the restraint hardly affects the flexibility at those low restraints, and we do not see the same effect for the other reference structure, this result is quite unexpected. This discrepancy might simply be due to statistical fluctuations in the ion permeation events, as they tend to occur in bursts that cause high fluctuations in the measured



currents, especially for sparse statistics. It is also possible that we are looking at a real effect on the permeation barrier induced by the reference structure. In case future analysis can confirm such an effect, we might gain deeper insights into the mechanics governing the ion permeation. Finally, correlating the RMSF and the current shows a direct relationship between these two observables (see Fig. 6.5E).

This high sensitivity of the SF to subtle changes in its flexibility helps us to understand why channel mutants introducing minor changes in the vicinity of the SF have such a strong impact on its conductance. In most cases, these mutants also show a profound impact on the C-type inactivation kinetics. Today, the most widely accepted model for this state has been the so called collapsed conformation, crystallographically resolved under low  $K^+$  concentrations, which displays a distinct rearrangement of the Val 76 and Tyr 78 backbone carbonyl-oxygen atoms. Seeing that already extremely small changes in the flexibility suffice to render the SF non-conductive, one can speculate that the inactivation process under physiological conditions would not necessarily need such large rearrangements.

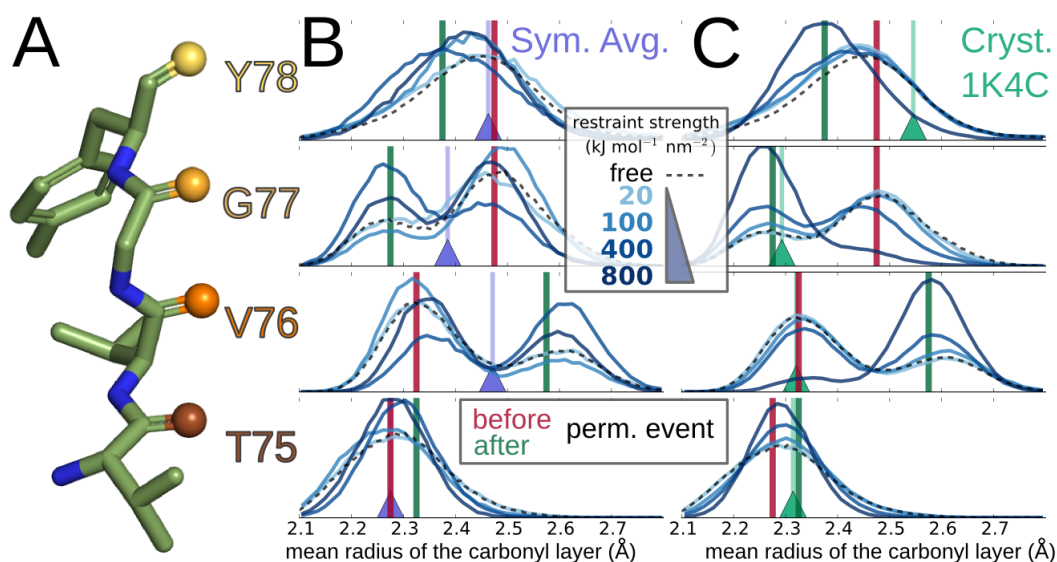
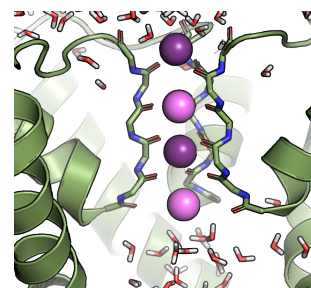


Figure 6.6: **The restraints change the equilibrium distributions of the backbone carbonyl-oxygen-layer radii.** (A) Structure of the SF with the positions of the SF carbonyl-oxygen atoms which correspond to the distributions to the right. (B) and (C) Distributions of the carbonyl-layer radii corresponding to (A) for unrestrained simulations (black broken line) and for increasingly strong restraints to (B) the symmetrized average structure (light blue to dark blue) and (C) to the crystal structure. Triangles depict the corresponding radii in the reference structures; the red and green lines show the most frequently encountered radius before and after the permeation event, respectively (corresponding to the peaks of the distributions in Fig. 6.2).

Finally, we analyzed the impact of the position restraint strength on the carbonyl-layer radii as shown in Fig. 6.6. Here, we can observe the deviations in the radius distributions from the unrestrained simulation (black dashed lines) as induced by an increasingly strong position restraint (bright to dark blue lines) for the two reference structures (1K4C: left column; symmetrized average: right side). In correspondence with the RMSF measurements, we find the radii distributions unaffected by the lowest restraint of  $20 \text{ kJ mol}^{-1} \text{ nm}^{-2}$  and also only slightly influenced by  $100 \text{ kJ mol}^{-1} \text{ nm}^{-2}$  restraints. At tighter restraints, we observe significant changes in the distributions. For Thr 75, these are most straightforward: the higher the restraint, the narrower and higher is the approximately gaussian shaped distribution of the radii. In all the other distributions, the shift in the distribution caused by the restraint is not as obvious. As for Thr 75, one might have expected the distribution to narrow around the reference structure (indicated by the triangles). Instead, we find the exact opposite in some cases, most strikingly in Val 76 with the symmetrized average structure as a reference. This discrepancy indicates how much the carbonyl-layers are coupled among each other. Indeed, we find that the layers do not simply adhere to the imposed restraint, but the whole SF structure needs to find an energetic compromise, which still needs to respect the two states corresponding to the situation before and after the permeation event. This compromise is most directly observed in the mentioned case of the highest restraint of  $800 \text{ kJ mol}^{-1} \text{ nm}^{-2}$  towards the crystal structure, where globally the restraints drive the structure towards the conformation found after a permeation event (green lines), but which locally drives the carbonyl-oxygen atoms of Val 76 far away from the restraint.

The SF therefore shows signs of a frustrated system, where not all parts of the system can be in an energetic minimum at once. In this picture, the pre- and post-permeation-event states would be metastable interconverting in a seesaw like fashion. The free energy gained by one state would be paid by the other and vice versa, which fits well with the proposed mechanism in chapter 5 where we postulated in Fig. 5.7E exactly such a seesaw mechanism for the ions. The necessary link for such a mechanism that couples the carbonyl moieties could be translated through the backbone of the SF itself, but also—which seems more likely—by the interspersed sitting ions in the filter, which determine either a conformation resembling the pre- or post-permeation filter. The restraint therefore seems to lock the SF in one conformation by increasing the energetic barrier of the transition, explaining why we still see similar populations for the radii even at higher restraints, but almost no current.

The observed interaction between the carbonyl-oxygen radii contributes to the discussion of selectivity. Based on the observation that  $\text{Na}^+$  acts as a voltage dependent blocker for medium high voltages (around 70 mV) [39], we propose that



at these voltages, where  $\text{Na}^+$  is able to enter the SF, the smaller  $\text{Na}^+$  bound to the potassium binding sites will constrict the surrounding carbonyl-layers stronger than a  $\text{K}^+$  ion would. According to our findings, this would lock the SF in one of its two conformations and therefore impede the ion flow.

## 6.4 Conclusions

From analyzing the motion of the SF during spontaneous ion permeation events, we have learned that the ion-coordinating carbonyl-oxygen atoms should not be viewed as obstacles that ions need to push aside, but they rather move between the closely packed ions to shield their electrostatic repulsion. These interactions explain why the SF actually constricts during the passage of ions like the peristaltic motions of the colon and—not as one might have intuitively thought—widen the passage through a saloon door. We have found that the SF takes on two distinct conformations, one before the ion permeation event and one just after the event. We have seen that the SF seems to behave like a frustrated system when interconverting between these two states.

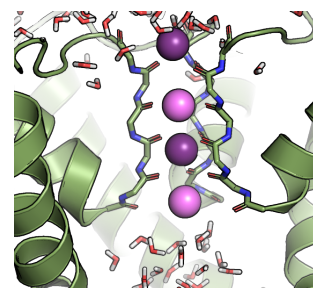
By restraining the SF flexibility, we find that already subtle changes on the order of 0.1 Å have a drastic impact on the channel conductance, locking the SF in one of its conformations. Understanding this high sensitivity is key in understanding the high impact of conservative mutants in the vicinity of the SF and might help to understand the inactivation mechanism as well as the channel's strict ion selectivity.

## 7. Outlook I: $K^+$ Versus $Na^+$ Selectivity of KcsA

### 7.1 Introduction

One of the key characteristic features of ion channels is their preference in conductance for a specific ionic species [1,12,28].  $K^+$  channels have evolved to specifically allow the passage of the comparably big  $K^+$  ions while blocking the passage for smaller ions such as the physiologically highly relevant  $Na^+$  ions [28,164]. For the prokaryotic  $K^+$  channel KcsA, the ratio of  $Na^+ : K^+$  permeability has been conservatively estimated to be lower than 0.006 under physiological conditions with 10 mM  $K^+$  and 100 mM  $Na^+$  extracellular, and 100 mM  $K^+$  intracellular ion concentrations from reversal potential measurements [34]. A fair comparison of the channel selectivity with equal intracellular concentrations for  $K^+$  and  $Na^+$  is experimentally not feasible, as intracellular  $Na^+$  has shown to be a very efficient voltage-dependent blocker [38,39,164].

The question how  $K^+$  channels are able to efficiently conduct the larger  $K^+$  ions while being almost impermeable to the smaller  $Na^+$  ions has long since occupied physiologists. As early as 1959 Mullins et al. proposed that the channel would optimally mimic the hydration shell of  $K^+$  while the ion passes through the channel and that these geometries would be unfavorable for  $Na^+$  ions [170]. This theory still remains as a viable possibility even in the years after 1998, when the first crystal structure of the prokaryotic KcsA  $K^+$  channel was published [15]. In general two types of models are still lively discussed: In the first group of models, mainly thermodynamical arguments are put forth, postulating a difference in the binding free energy between  $Na^+$  and  $K^+$  in the binding sites of the SF. A prominent member of this group is the so called snug-fit-model, that based on the binding distances of the backbone carbonyl atoms in the SF in crystal structures, proposes that  $Na^+$  would have a high energy penalty to bind to these sites as opposed to bulk water [15]. Along similar lines it has been proposed that eight coordinating carbonyl-oxygen atoms will energetically favor  $K^+$ , whereas it would be unfavorable for  $Na^+$  [171]. Furthermore, there is a number of MD based free energy cal-



culations that have estimated the difference in the free energy of binding between  $K^+$  ions and  $Na^+$  ions to be on the order of  $20 \text{ kJ mol}^{-1}$  [19,23,172].

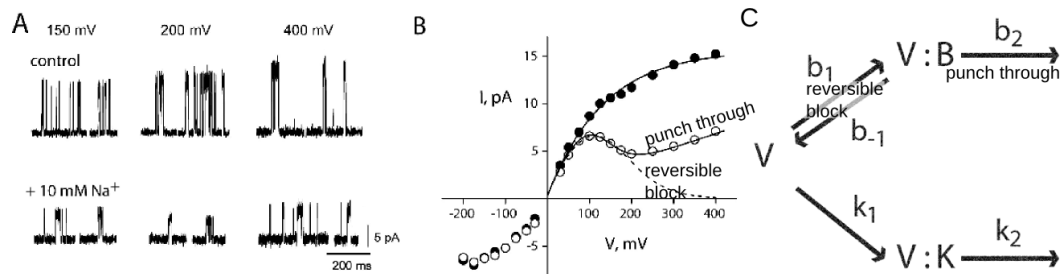


Figure 7.1: Effect of intracellular  $Na^+$  on the conductance of the KcsA  $K^+$  channel (figures from Nimigean, and Miller, *Gen Physiol* 2002) [39]. (A) Single channel recordings of KcsA at different voltages before (top) and after (bottom) addition of 10 mM  $Na^+$ . (B) IV curve of the peak currents at symmetric 100 mM  $K^+$  (black dots) and after addition of 10 mM  $Na^+$  (white dots). (C) Kinetic model to describe conductance in the presence of intracellular  $Na^+$ .  $V$  is the vestibule binding site at the entrance to the SF,  $B$  is the blocker (in our case  $Na^+$ ), and  $K$  stands for  $K^+$ . The lower path describes  $K^+$  binding to the vestibule ( $k_1$ ) and eventually being conducted through the channel ( $k_2$ ) and the upper pathway describes  $Na^+$  binding ( $b_1$ ) and unbinding ( $b_{-1}$ ) to the vestibule and eventually also to be translocated through the SF ( $b_2$ ); all modeled with voltage dependent rate constants. A model without  $b_2$  is the basis for the dashed line in (B) which fits well to values below 200 mV and marks the regime where  $Na^+$  does not enter the SF, whereas the solid lines incorporate the  $b_2$  into the model and show the effects of  $Na^+$  entering and permeating through the SF, which Nimigean et al. have termed “punch through”.

In the second group of models the focus lies on kinetic arguments, with the general idea that the energetic barrier  $Na^+$  ions need to cross to enter the SF (or another section along the ionic pathway) is higher than the energetic barrier for  $K^+$  ions [173]. Using such a kinetic model, Nimigean et al. were able to model the phenomenon of an intracellular  $Na^+$ -block and even the eventual recovery from this block at higher voltages [164,174,175]. In their kinetic model, they propose competitive binding between  $K^+$  and  $Na^+$  just below the SF in the cavity, where  $K^+$  rapidly advances further through the SF, whereas  $Na^+$  faces a large entry-barrier and stalls the permeation until it unbinds through the cavity. Using this model they are able to explain the behavior of a voltage dependent  $Na^+$  block up to about 200 mV after which a recovery of conductance is observed. They explain the recovery from this  $Na^+$  block at higher electric potentials with  $Na^+$  overcoming the barrier and actually entering the SF where it is eventually and slowly—compared to the fast  $K^+$  transitions—translocated to the extracellular side.

In previous chapters 5 and 6, we have shown how MD simulations in combi-

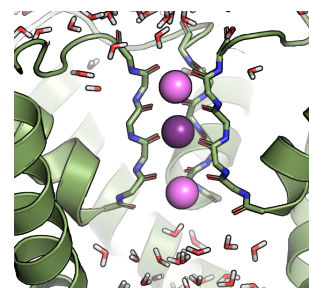


nation with the computational electrophysiology setup are able to simulate ion permeation through  $K^+$  channels at close to physiological conditions and yield experimental observables like electrophysiological currents and crystallographically determined ion occupancy. Here, we will apply the same technique under ionic conditions including  $Na^+$ , to test if the simulations will be capable of reproducing the ion selectivity of  $K^+$  channels. Such free simulations with their spontaneous ion permeation events will give us the opportunity to test many of the hypotheses—both, based on thermodynamics and kinetics—that have been put forth over the years. At the current state of this analysis, we will show preliminary results on the effects of  $Na^+$  on the channel conductance and we will test the hypothesis if the entrance to the SF implements the  $K^+$  selectivity. Finally, we will also take a look at the energy landscape obtained from Boltzmann inversion to see if we can find evidence for the thermodynamically based selectivity models.

## 7.2 Methods

Simulations were set up as described earlier in chapters 5 and 6 from the open KcsA crystal structure (PDB id: 3F5W) embedded into a patch of 216 POPC lipids and 14526 water molecules combined with 400 mM KCl (312 K, 320 Cl ions) using the program `g_membed`. The SF (TTVGYG) was replaced by the ordered structure found under high  $[K^+]$  (PDB id: 1K4C) and the whole system was thoroughly equilibrated for 100 ns with position restraints on all heavy atoms of the protein as well as the ions in the SF (binding sites  $S_0$ - $S_{cav}$ ). All simulations were run using the MD simulation software Gromacs 4.6 with the `amber99sb` forcefield, Berger et al. parameters for the lipids, Joung et al. parameters for the ions and the SPC/E water model. The pressure was maintained at 1 bar and the temperature at 320 K using the Berendsen barostat [85] and v-rescale thermostat [86], respectively.

A double membrane setup as needed for the computational electrophysiology setup was created by doubling the system along the Z axis. The membrane voltage of around 200 mV was maintained by imposing a constant ionic imbalance of  $2e^-$  with the computational electrophysiology scheme [67]. The different  $Na^+$  concentrations were generated by exchanging 156 and 234  $K^+$  ions from the bulk for set II and III, respectively (see Tab. 7.1). The average bulk concentrations were calculated for every frame by determining the number of ions in a rectangular volume 2 nm away from either membrane and dividing by that volume. Errors for concentrations and current are given as standard error of the mean from all independent simulations.



## 7.3 Results and discussion

### 7.3.1 Impact of Na<sup>+</sup> on the current

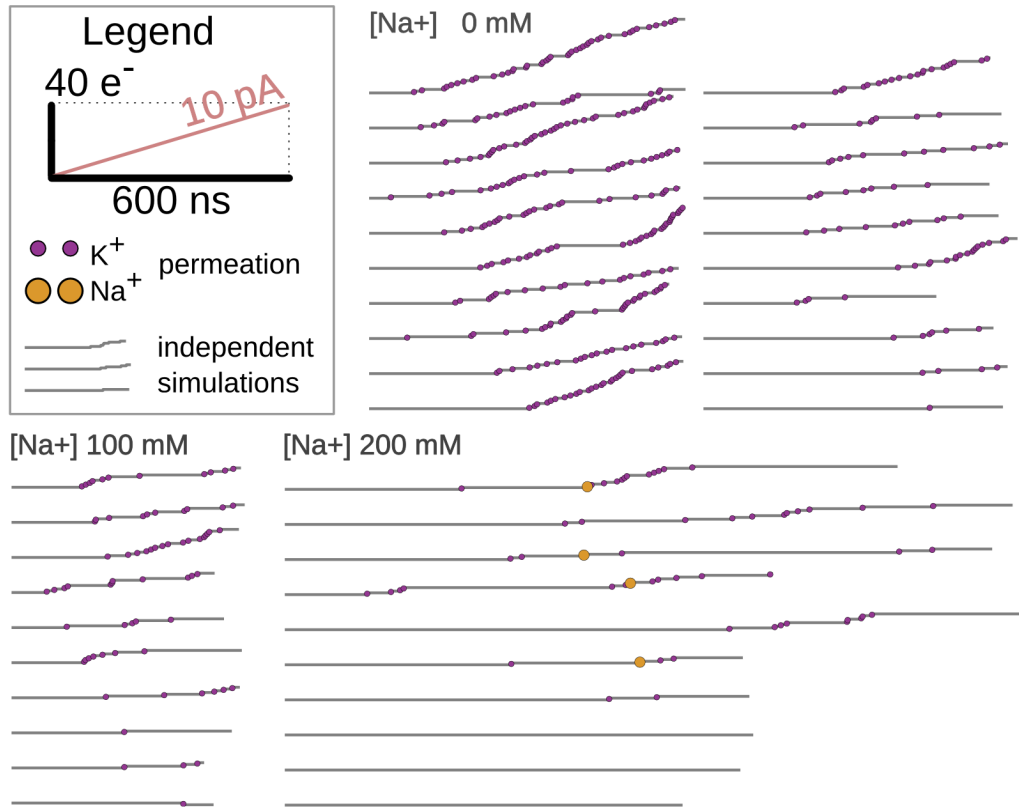


Figure 7.2: Ion permeation events observed for three different Na<sup>+</sup> concentrations at about equal ionic strength of 300-400 mM. References for the time and charge axes are given in the legend. Each line within the three sets of different Na<sup>+</sup> concentrations represents an independent simulation with a purple circle for each K<sup>+</sup> and a yellow circle for each Na<sup>+</sup> permeation event.

To study the impact of Na<sup>+</sup> on the ionic current through K<sup>+</sup> channels, we modified the initial setup, which had previously proven successful in simulations of the K<sup>+</sup> current through the prokaryotic KcsA at about 200 mV. Apart from the already used data set of about 20 independent simulations covering a total of 15  $\mu$ s with 379 ion permeation events (set I in Tab. 7.1), we ran additional simulations with a total of 5.5  $\mu$ s at 100 mM (set II) and 14.9  $\mu$ s at 200 mM Na<sup>+</sup> (set III) each set with 10 independent simulations and observed 69 and 57 ion permeation events, respectively. These ion permeation events are visualized in Fig. 7.2 for all simu-

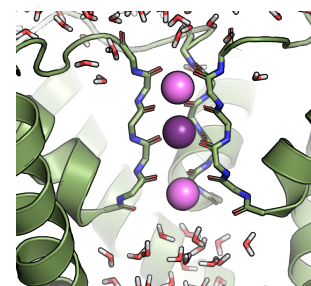
lations with indication of the permeating ion type. The most striking result is a decrease in the overall conductance with increasing  $\text{Na}^+$  concentration as summarized in Fig. 7.3. We find that each addition of 100 mM  $\text{Na}^+$  about halves the current through the channel. Such a decrease in current with an increasing  $\text{Na}^+$  concentration is in qualitative accord with the experimentally observed intracellular  $\text{Na}^+$  block where adding 10 mM  $\text{Na}^+$  has a similar effect on the channel conductance at 200 mV [39]. It remains open why simulations with 100 mM  $[\text{Na}^+]$  show the same effect on the current as 10 mM in the experiment. We speculate that this discrepancy might be an artifact of the starting conditions going back to insufficient sampling. A slight indication for that is visible in the distributions of the permeation events as shown in Fig. 7.2. The first half of the simulations contains visibly fewer permeation events than the second half, suggesting that the system did not reach full convergence, despite the high computational effort. This slow convergence towards a more conductive state, in turn, suggests that the crystal structure based starting conditions of our simulations are not the optimally conductive state. We will therefore dedicate future efforts to finding a structural explanation for the fast permeation regime which hopefully offers deeper insight into the molecular machinery of the channel.

Table 7.1: **Simulation results summary for KcsA at 200 mV and an ionic strength around 350 mM with varying concentration of  $\text{Na}^+$ .**

Simulation set	I	II	III
ionic strength (mM)	409±13	361±8	326±9
$\text{K}^+$ concentration (mM)	409±13	263±5	139±4
$\text{Na}^+$ concentration (mM)	0	98±6	186±7
# independent simulations	20	10	10
total simulation time ( $\mu\text{s}$ )	15.12	5.46	13.91
# total permeation events (Na)	379 (0)	69 (0)	57 (4)
current (pA)	4.0±0.5	2.0±0.4	0.66±0.17
$\text{Na}^+$ current (pA)	0.0	0.0	0.05±0.02

### 7.3.2 Ion specificity at the entrance to the SF

Our simulations qualitatively reproduce the channel specificity of  $\text{K}^+$  ions over  $\text{Na}^+$ : During the simulations with 100 mM  $\text{Na}^+$ , we do not observe a single  $\text{Na}^+$  permeation, despite the 1:2 ratio of  $\text{Na}^+:\text{K}^+$  in the bulk, and even in the more extreme case with 2:1  $\text{Na}^+:\text{K}^+$  in the bulk, we still find  $\text{K}^+$  ions favored by 1:13 in the permeation events. Experimentally, the conductance ratio has been measured to be lower than 0.006 (about 1:170) via reversal potential measurements. However,



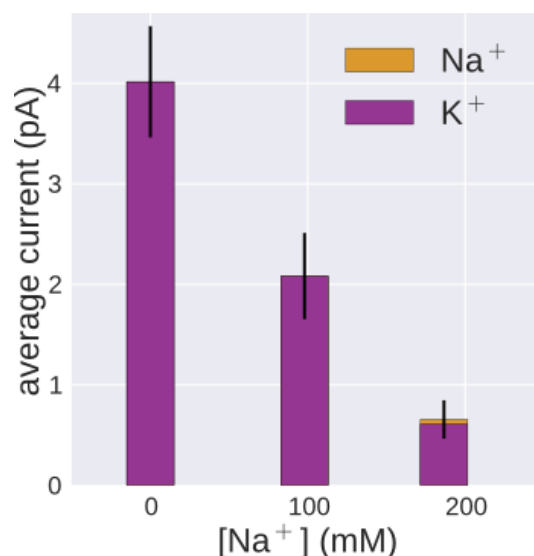


Figure 7.3: **Average current through the K<sup>+</sup> channel as a function of the Na<sup>+</sup> concentration.** The current through the K<sup>+</sup> channel about halves, as the Na<sup>+</sup> concentration increases by 100 mM. Despite a Na<sup>+</sup> to K<sup>+</sup> ion ratio of 1:2 in the bulk at 100 mM Na<sup>+</sup> and 2:1 at 200 mM, the current through the channel is strictly dominated by K<sup>+</sup> only.

the ionic conditions (100 mM K<sup>+</sup> and no Na<sup>+</sup> in the internal solution and 10 mM K<sup>+</sup> and 100 mM Na<sup>+</sup> in the external solution) differ strongly from the ones used in the simulation setup which aggravates a direct comparison to our results. We can, however, say that our current data with Na<sup>+</sup> concentrations as high as 100 mM does not contradict these experimentally measured ratios. Here, we expect longer simulation timescales to eventually show Na<sup>+</sup> transitions, which would allow to determine the actual Na<sup>+</sup> to K<sup>+</sup> selectivity ratio.

Next we wanted to test the hypothesis if the intracellular entrance to the SF inside the cavity is responsible for the ion selectivity. There have been also speculations that the water filled cavity itself might possess an intrinsic specificity for K<sup>+</sup> ions [39] but most theories hypothesize that the discrimination of impermeable ions is implemented before entering the single-file regime in the SF [164], as subsequent discrimination would entail unbinding from the SF and re-hydrating the Na<sup>+</sup> ion against the electric gradient. To test for an ionic preference of the cavity, we monitored the probability of finding either ion species at the intracellular entrance to the SF as indicated by the red cylinder in Fig. 7.4A. If a preference would exist, we would expect the ratio of probability to find either Na<sup>+</sup> or K<sup>+</sup> to differ from the corresponding probability ratio of finding either ion in bulk. As shown in Fig. 7.4B (left panel), the ratio of Na<sup>+</sup> to K<sup>+</sup> closely matches the ratio found in the

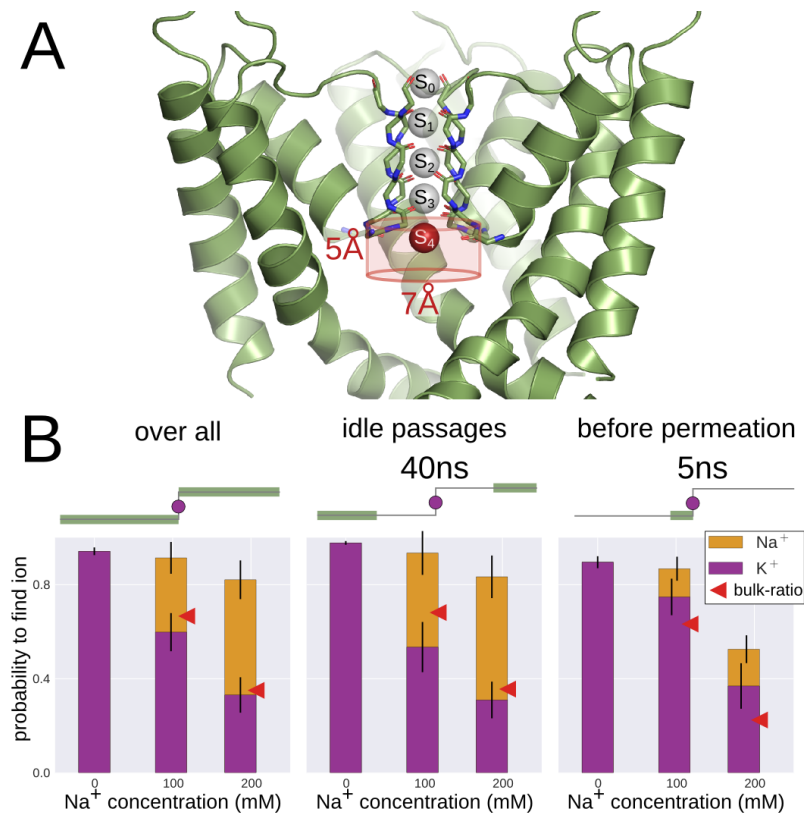
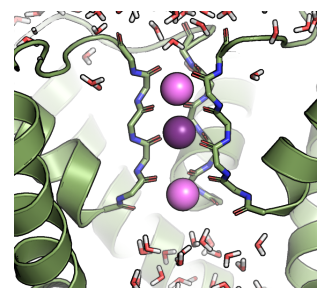


Figure 7.4: **Ion occupancy of the lower vestibule.** (A) The red cylinder represents the entrance to the intracellular entrance of the SF. (B) For each Na<sup>+</sup> concentration we visualize the occupancy distinct by ion type. The red triangles indicate the ratio between Na<sup>+</sup> and K<sup>+</sup> ions as found in bulk (in cases of Na<sup>+</sup> and K<sup>+</sup> mixtures). These occupancies were determined for frames (indicated in green) from: all simulations without any limitation (right side), during idle times (at least 20 ns away from any future or past permeation events, middle) and 5 ns before a permeation event (left).

bulk solution (red arrows) with maybe a slight preference for Na<sup>+</sup>. We speculate that the slight preference for Na<sup>+</sup> goes back to the Na<sup>+</sup> ions getting trapped at this site, whereas K<sup>+</sup> ions are translocated through the SF. These stuck ions increase the apparent Na<sup>+</sup> concentration, whereas the cavity itself is non-selective.

We then used our simulations to test if Na<sup>+</sup> at the entrance to the SF is the source of the intracellular, voltage dependent Na<sup>+</sup> block as proposed by Nimmigen et al. [38, 39]. This hypothesis states that Na<sup>+</sup> and K<sup>+</sup> compete for a common binding site at the entrance of the SF, where bound K<sup>+</sup> rapidly enters the SF whereas bound Na<sup>+</sup> faces a large barrier. Na<sup>+</sup> bound to this site may then either stall the permeation process until it unbinds and diffuses away through the cavity



which would correspond to the reversible-block-regime as depicted in Fig. 7.1, or may even overcome that barrier and enter into the SF where  $\text{Na}^+$  ions transit to the extracellular side with a slow timeconstant which corresponds to the punch-through-regime. In the reversible-blocker-regime, one would therefore expect a decrease in the overall current and an increase in the  $\text{Na}^+$  occupancy during times with no permeation events, as long as no  $\text{Na}^+$  ions enter the SF. For simulations at 100 mM  $\text{Na}^+$  concentration we know that  $\text{Na}^+$  did not enter the SF and as shown in Fig. 7.4B (middle panel), we indeed find an increased probability to encounter a  $\text{Na}^+$  ion during idle times. As opposed to that, in the punch-through-regime, one would also expect a decrease in the overall current. However, as the rate limiting step of the permeation process now rests on the slow timescales of  $\text{Na}^+$  translocation through the SF, one would not expect a difference between the ionic occupancy ratio at the SF entrance as compared to the bulk because the faster exchange timescales of ions at the SF entrance. This description fits well with the observations of simulations under 200 mM  $[\text{Na}^+]$ , where we observe  $\text{Na}^+$  permeation events which clearly speaks for the punch-through-regime. As seen in Fig. 7.4B, we do not observe a significant deviation from the ionic ratio found in bulk.

The complementary test of the entrance-discrimination-hypothesis is to monitor the probability of encountering a  $\text{K}^+$  ion shortly before a permeation process. The ions propagate through the SF as one column in the “knock-on” process, where the newly arriving ion initiates the permeation event. If  $\text{Na}^+$  ions are thought to stall the permeation process,  $\text{K}^+$  ions must in comparison accelerate the process and therefore should be more frequently found at the entrance to the SF just before the ions advance, independent of the blocker-regime. As shown in Fig. 7.4B (right panel) such an increased probability of finding a  $\text{K}^+$  ion as compared to the bulk ratio of  $\text{Na}^+:\text{K}^+$  just before a permeation event is indeed the case for the two analyzed concentrations.

The current analysis therefore qualitatively corroborates the kinetic model in both the reversible-block and the punch-through-regime. Next steps would be to obtain estimates for the rates from the simulations and compare those to experiments. So far our analysis have not made use of the ability to trace every ion’s pathway as would be possible from the MD trajectories, but so far has looked only at populations. We should be able to gain a more systematic and detailed picture when we look at the dwell time of the ion at each binding site as a function of the surrounding ionic configuration. Such an analysis might be done using a Markov-state-model, where the states are defined as the ionic configuration of defined sites along the channel. From such a model we would be able to systematically assess frequently visited states, and the timescales of their transitions. Before we commence this kind analysis however, we must first understand if it is applicable

to our problem, as the present simulations do not sample an equilibrium but a steady-state, so that the requirement of a detailed balance will not be met.

### 7.3.3 Density profiles of the SF

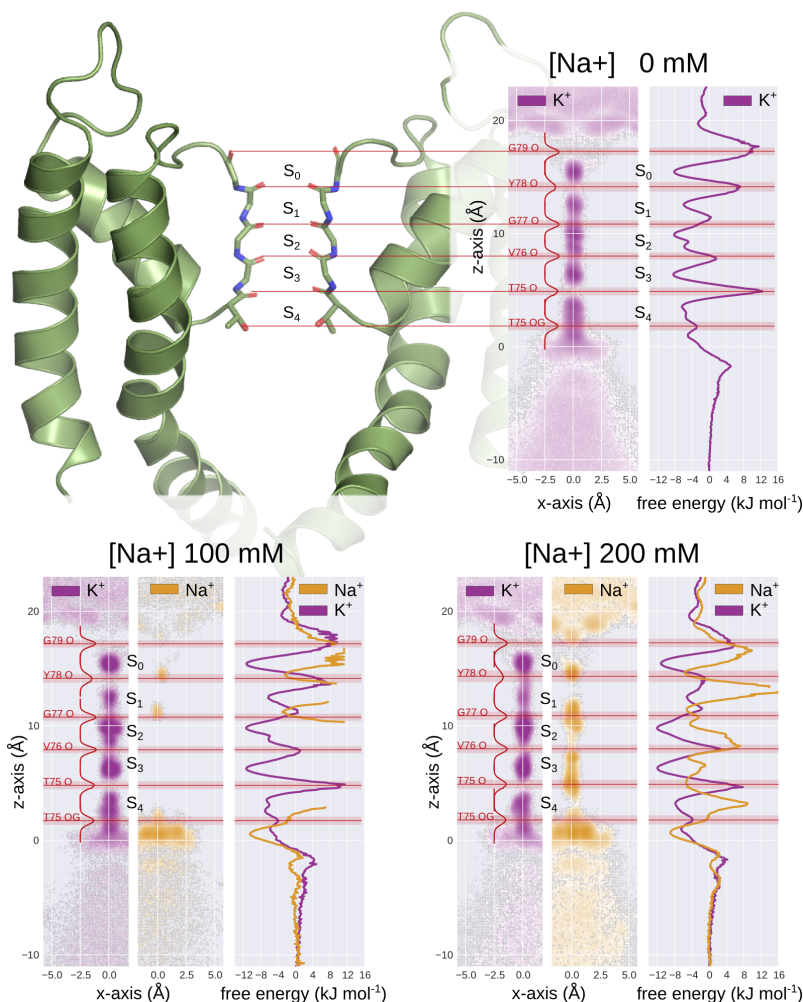
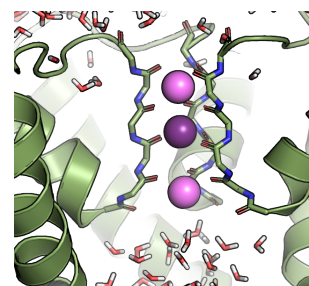


Figure 7.5: **Logarithmic ion density of  $K^+$  (purple) and  $Na^+$  (yellow) along the filter axis for different  $Na^+$  concentrations.** Red lines indicate the positions and distributions of the SF-forming carbonyl-oxygen atoms. Right of each panel shows the logarithmic density of the corresponding ion type in the x-z-plane through the SF and the cavity. The left panels show the logarithmic density of the corresponding ion type along the channel axis in units of  $kJ\ mol^{-1}$ .

As the previous analysis of the ions entering the SF was based on the kinetics of  $Na^+$  vs.  $K^+$  binding, we now evaluated our simulation results in terms of a



thermodynamic picture, by looking at the density distributions of the ions in the SF. With simulation times on the 10  $\mu\text{s}$  scale and several  $\text{K}^+$  ion transitions for each  $\text{Na}^+$  concentration, the sampling should be sufficient to generate a meaningful free energy landscape from the densities. However, as the simulations do not strictly sample an equilibrium (but rather a steady state), we have to consider the magnitude of the perturbation from the electric gradient on the resulting “free energy profiles”: The electric gradient of 200 mV would give rise to a skew of the potential landscape for a permeating ion of about  $20 \text{ kJ mol}^{-1}$  (0.2 eV). Seeing that this potential drops across the whole channel ( $\sim 30 \text{ \AA}$ ) and the distance between two adjacent binding sites is about  $3 \text{ \AA}$ , the perturbation in energy between two binding sites can be estimated to about  $2 \text{ kJ mol}^{-1}$ , which is about a factor of 5 smaller than the average barriers found between the binding sites. In the following analysis we will assume that the imposed electric potential can be regarded as a perturbation on the free-energy landscape. However, we are aware that this might be a source of systematic errors.

Figure 7.5 visualizes (left sides of each panel), the logarithmic densities of  $\text{K}^+$  and  $\text{Na}^+$  ions projected on a plane through the SF and cavity. In accord with crystal structures and previous work [15, 42, 176], we find the  $\text{K}^+$  ions (purple) to bind between the carbonyl-layers (red lines and distributions), whereas  $\text{Na}^+$  (yellow) tends to bind in plane with the carbonyl-layers as previously described by Thompson et al. [164]. This preference for a 8-fold coordinated binding site in the case of  $\text{K}^+$  as opposed to a 4-fold coordination for the smaller  $\text{Na}^+$  ions is in accordance with the theory that selectivity is instantiated via an optimal number of coordinating ligands [171]. As a side note, the different binding locations of  $\text{Na}^+$  and  $\text{K}^+$  question the validity of MD based binding free energy calculations, obtained from exchanging  $\text{K}^+$  and  $\text{Na}^+$  ions at a given binding site inside the SF. Based on these results, it is clear that a  $\text{Na}^+$  ion would display a much higher binding free energy when forced into the same position as a  $\text{K}^+$  ion.

The right hand side of each panel in Fig. 7.5 is the corresponding free energy landscape as generated by Boltzmann-inversion from the densities along the channel axis. All free energies are given with respect to the bulk ( $=0 \text{ kJ mol}^{-1}$ ). For the  $\text{K}^+$  ions (purple curves) we find consistent profiles for all three simulation sets, with the deepest minima for  $S_2$ ,  $S_3$  and  $S_0$  at around  $-10 \text{ kJ mol}^{-1}$  and slightly higher free energies of about  $-6 \text{ kJ mol}^{-1}$  for sites  $S_1$  and  $S_4$ . The highest barriers are consistently found between  $S_4$  to  $S_3$  and  $S_0$  to bulk on the order of  $+10 \text{ kJ mol}^{-1}$ , which suggests that entering and exiting the SF is the rate limiting step for the  $\text{K}^+$  permeation. Such barriers are in agreement with previous simulations, estimating the free energy of permeation to be between 8 and  $12 \text{ kJ mol}^{-1}$  [42].

For  $\text{Na}^+$ , the convergence of the free energy profiles is less favorable. As we do not observe any  $\text{Na}^+$  transitions at 100 mM  $\text{Na}^+$ , this is not surprising. For

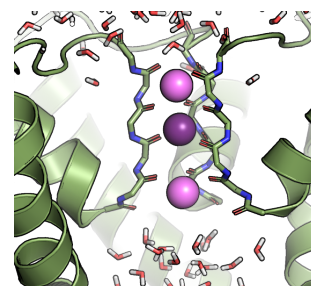


the simulation set with 200 mM Na<sup>+</sup>, however, we have observed four full Na<sup>+</sup> transitions so far and found a corresponding continuous density in the SF. The free energy profile associated with this density suggests—contrary to what we found in the kinetic analysis in the previous section for—that the barrier for Na<sup>+</sup> to enter the SF is similar to the one found for K<sup>+</sup>. Furthermore, based on the current data, the highest barrier for Na<sup>+</sup> of around +15 to +20 kJ mol<sup>-1</sup> would be expected at S<sub>1</sub> and thus, more towards the extracellular side of the SF. This is in contrast to the previous kinetic analysis, where we found a high barrier for Na<sup>+</sup> to enter the SF. The difference in binding free energy between Na<sup>+</sup> and K<sup>+</sup> at their respective binding sites is about 8 kJ mol<sup>-1</sup> and would—in the most simple picture, account for a population difference of around 1:25 which is in reasonable agreement with the observed conductance ratio of 1:13 during the simulations. This ratio is far below the experimentally predicted lower limit of 1:170, but it is expected to decrease as the ratio of Na<sup>+</sup> to K<sup>+</sup> concentrations in the bulk approach physiological concentrations.

The discrepancies in explaining the selectivity between the kinetic and thermodynamic model derived from the same simulation data suggest that the simple interpretation of the free energy landscapes might be insufficient. Apart from the general validity of these landscapes in light of the high electric gradient, we will need to find a better framework in which these landscapes can be interpreted. We have started to address this problem in Chapter 5 in Fig. 5.7 where we look at the changes of the energy landscape of three K<sup>+</sup> ions during the course of a permeation event. Also there, the highest apparent barrier in the resting state (between S<sub>2</sub> and S<sub>3</sub>) does not limit the rate, but rather the barrier between S<sub>2</sub> and S<sub>1</sub>. We need to consider that these landscapes do not represent the energetics for a single ion but change—considering their high charge and close proximity—drastically as the configuration of the surrounding ions changes. Here we will need a systematic approach that takes these conformational changes into account if we want to understand the energetics of the permeation.

## 7.4 Conclusion

Using free MD simulations with an applied voltage, we are able to reproduce the K<sup>+</sup> channel specificity of K<sup>+</sup> over Na<sup>+</sup> on the molecular level. By looking at the probability ratios of finding ions at the intracellular entry to the SF, we rejected the postulated ion-specificity of the cavity, but found good agreement with the kinetic model of Nimigean et al. both for the reversible-block and the punch-through-regime. However, the free energy landscapes derived from the ion densities seem to contradict these preliminary results. Here, we strongly believe that a more complex framework is needed for a conclusive analysis of these energy profiles,



that takes the ion configurations into account.

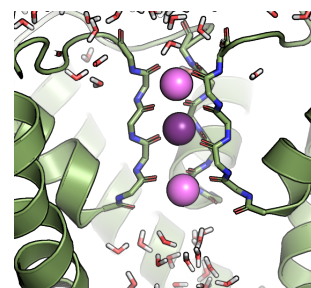
## 8. Outlook II: Coupling Between Inactivation and Gating in KcsA

### 8.1 Introduction

Ion channels are at the core of innumerable physiological responses in living cells. This functionality rests on the channel's ability to switch its conductance in response to external stimuli [1, 2, 28]. To fulfill their role in complex signaling processes, channels have evolved with a variety of different switching mechanisms that enable more complex and more finely tuned responses than a single switch would allow. In  $K^+$  channels the most frequently encountered mode of switching between a conductive and non-conductive state is gating—a process during which helical bundles at the intracellular side of the channel straighten and interweave to block the ionic pathway (see Fig. 8.1).

Another important mechanism in many  $K^+$  channels is the so called C-type inactivation, which typically closes the channel after prolonged conductive periods [37, 45, 46, 53–55]. With single point mutations the structural origin of this switch could be pinpointed to the SF [53]. The most famous mutant in this context is the E71A KcsA mutant [53], which completely lacks an inactivated state. On the structural level, this deficiency goes back to an important hydrogen bond directly behind the SF that causes Asp 80 just on the extracellular mouth of the SF to flip towards the bulk as shown in Fig. 8.2 [52].

The current consensus structural model of inactivation goes back to two states the SF could be crystallized in: one representing the conductive state where the backbone carbonyls form regular spaced binding sites (PDB ids: 1K4C and 3FB7) [15, 37] and structures recorded at low  $K^+$  concentrations representative of the inactivated state, where the backbone carbonyl-oxygen atoms of the central amino acids are tilted sideways (PDB ids: 1K4D and 3F5W) [37, 49] (see also chapter 4 and Fig. 4.2A,B). Yet, in a recent study, Devaraneni et al. have created a KcsA variant capable of inactivation, despite synthetic amino acids in the SF that prevent structural rearrangements analogous to those under low  $K^+$  conditions [50]. Thus, the question of what the inactivated state looks like still remains under discussion.



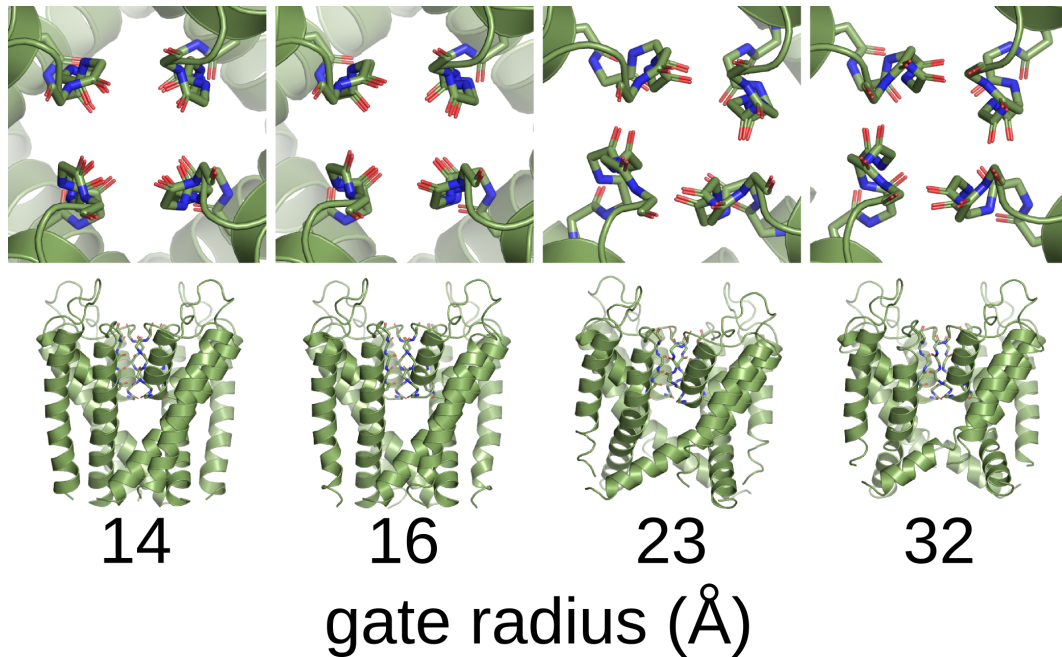


Figure 8.1: **Series of crystal structures with varying degree of gate opening** [37]. **Top row:** view along the ion permeation pathway from the extracellular side into the SF. A well stacked configuration is found when the gate is closed, whereas the SF configuration tilts sideways in structures with an opened gate. **bottom row:** Cartoon representation of KcsA with different degrees of gate opening (PDB ids: 3FB5, 3FB6, 3F7V, 3F5W).

Electrophysiological studies have long since established that gating and inactivation are coupled phenomena [37,45,46,53–55]. For instance, KcsA is only able to recover from inactivation when its gate is closed. Structural evidence for this coupling is presented by a series of KcsA structures with different degrees of gate opening [37] (see Fig. 8.1), where the SF adopts a state as found under high  $K^+$  concentrations when the gate is closed and a distorted SF comparable with crystal structures under low  $K^+$  concentrations when the gate is open.

Here, we set out to study inactivation and its link to gating by comparing simulations of the WT capable of inactivating with simulations of the non-inactivating E71A mutant under physiological conditions. As channel inactivation is a response to prolonged currents through the SF, we used the computational physiology setup to mimic inactivation-inducing conditions. We used functional mode analysis (FMA) [68], a tool to find structural changes that correlate best with an external observable, to find the states that would best distinguish WT from E71A.

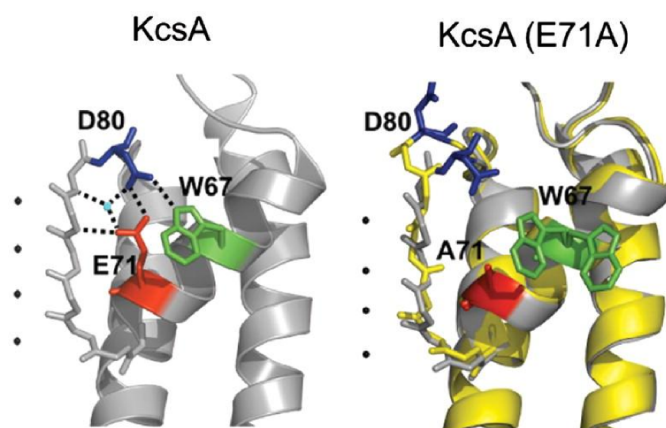
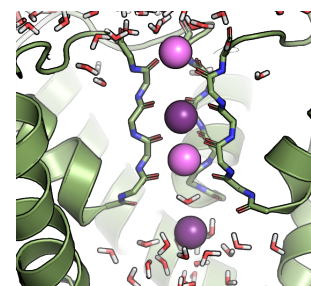


Figure 8.2: **Comparison between crystal structures of KcsA WT and E71A mutant.** We see how E71 forms a hydrogen bond with D80 directly behind the SF in the WT. In the E71A mutant (yellow structure), this bridge can no longer be formed which leads to D80 flipping outwards (blue) into the extracellular bulk and causing rearrangements in the SF (image taken from Cheng et al. 2011 [52]).

## 8.2 Methods

The simulations were created as described in chapters 5, 6 and 7 from the open KcsA crystal structure (PDB id: 3F5W [37]) embedded into a patch of 216 POPC lipids and 14526 water molecules combined with 400 mM KCl (312  $K^+$ , 320  $Cl^-$  ions) using the *g\_membed* program [109]. The SF (TTVGYG) was replaced by the ordered structure found under high  $K^+$  concentration (PDB id: 1K4C [15]) and the whole system was thoroughly equilibrated for 100 ns with position restraints on all heavy atoms of the protein as well as the ions in the SF (binding sites  $S_0$ - $S_{cav}$ ). All simulations were run using the MD simulation package Gromacs 4.6 [84] with the *amber99sb* forcefield [78], Berger et al. parameters for the lipids [110], Joung et al. parameters for the ions [144] and the SPC/E water model. The pressure was maintained at 1 bar and the temperature at 320 K using the Berendsen barostat [85] and *v-rescale* thermostat [86], respectively. A double membrane setup as needed for the computational electrophysiology setup was created by doubling the system along the Z axis. The membrane voltage of around 200 mV was maintained by imposing a constant ionic imbalance of  $2e^-$  with the computational electrophysiology scheme [67]. The mutant was created from the WT using the homology modeling software package Modeller 8.9 [177] and exchanged for the WT in the previously described system, with an additional 100 ns equilibration before production runs. To prevent unraveling of the tips of the S5 and S6 helices the backbone hydrogen bonds of the last 4 amino acids were strengthened by an additional distance re-



straint. Furthermore, a distance restraint between the lower ends of the S6 helix was introduced to prevent the channel from closing. FMA was carried out using an in-house implementation based on the partial least squares (PLS) algorithm [68] (details explained in the results section).

### 8.3 Results and discussion

As inactivation takes place after prolonged currents through the channel, we chose ion concentrations of 400 mM and a trans-membrane voltage of 200 mV as a compromise between obtaining high ionic currents while staying in a regime close to physiological conditions. In addition to the 20 independent simulations with a total simulation time of the 15  $\mu$ s of KcsA WT (also used in chapters 5, 6 and 7), we conducted an additional 10 simulations with a total of 8.7  $\mu$ s of simulation time with the E71A mutant under the same conditions. Even with this stretch towards inactivation-favoring conditions, we can not expect a full transition to the inactivated state, as this process typically takes seconds. However, we might still expect to gain insights into the mechanism from the structural changes induced by this conservative mutation.

#### Functional mode analysis to distinguish between WT and E71A mutant

The PLS based FMA-model was constructed using the main chain atoms of both WT and E71A, resulting in the same number of atoms for both channels. Half of the frames from the E71A mutant simulations (2243 frames), taken from the first five independent simulations and the same number of frames from the WT simulations, were used for the training. For the external observable, the PLS-algorithm uses to distinguish the supplied frames by, we assigned +1 to the WT structures and -1 to the mutant structures, resulting in a vector with a zero average.

Models based on very few PLS-vectors could be used to distinguish between WT and mutant structures as shown in Fig. 8.3A (green curve). For cross validation, we used the remaining frames, which were not part of the training and found an optimal correlation coefficient of 0.85 using four PLS-vectors as shown in Fig. 8.3A (blue curve and yellow line). Figure 8.3B and C show the prediction for training (green) and validation (blue), respectively with this optimal number of PLS-vectors. We found that the training clearly separates the two structures on the continuous linear vector that best separates WT and E71A structures. Using a threshold criterion between the two extremes to predict WT and E71A structures, we achieve a 0.93 success rate.

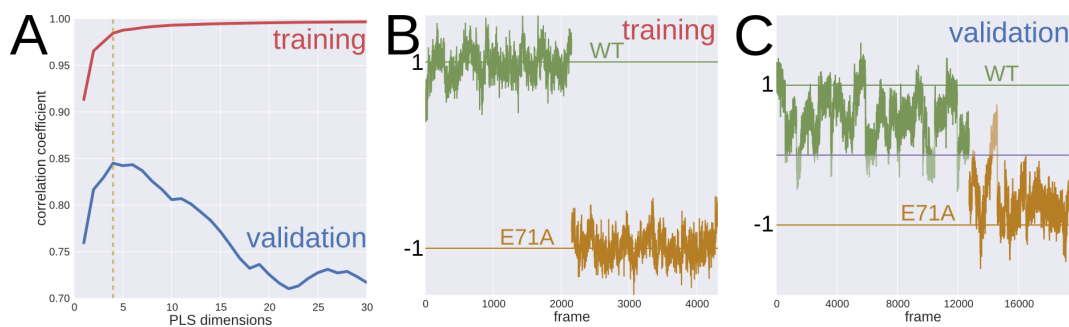
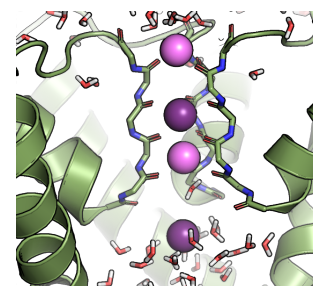


Figure 8.3: The partial least squares analysis is able to distinguish structures from the WT and E71A mutant with a correlation coefficient of 0.85. The model was trained on 2200 frames from both WT and the E71A. For cross-validation, we used the model to predict the assignment to WT or E71A of the remaining 16000 frames that were not part of the training and originated from independent simulations. **(A)** Varying the number of PLS-vectors shows that already few vectors suffice for the training to converge to a correlation of one. For the subsequent analysis we used 4 PLS-vectors maximizing the correlation for the cross validation (yellow broken line). **(B)** Projection of the training set: 2243 frames of the WT simulations (green), and E71A simulations (orange), onto the PLS-model where 1 is the value assigned to WT frames and -1 to E71A frames. **(C)** Projection onto the PLS-model of the remaining frames of WT and E71A mutant simulations that were not part of the model training. Using a threshold at 0 (blue line) the model distinguishes WT from E71A structures with 0.93 accuracy (false positives and negatives are shaded).

### 8.3.1 Link between inactivation and gating

The differences between the states that—according to the FMA—maximally distinguish between WT and the E71A mutant are highly interesting. They suggest a correlated rearrangement of the SF and the lower helix bundles as one might expect for the coupling of inactivation and gating. The key mediating element of these rearrangements are the pore helices (PH) which, in the mutant, tilt by about  $10^\circ$  into the plane of the membrane as shown in Fig. 8.4A. This tilt causes an upward shift of the SF by  $1.2 \text{ \AA}$  which constricts the SF at its intracellular side and causes a widening at its extracellular side (see Fig. 8.4B). Moreover, the PH-tilt also correlates with a rotation of the neighboring S6-helix. As a result of this rotation, Gly99 (in the middle of the S6-helix) directly faces the PH in structures associated with E71A whereas in the WT associated structure it is tilted outwards. This Gly99 has been termed the “hinge of the S6-helix” as it represents a point crucial for the bending of the S6 helix that ultimately underlies the gating mechanism. We therefore speculate that an axial rotation of this joint could prevent bending of the helix in the same way as lying on one’s back one can dangle the lower leg



from the edge of a bed but not anymore when turned sideways. The most direct way of assessing the impact on gating would be to directly measure the opening of the lower bundle. However, in the current simulation setup a distance restraint was implemented to counteract the closing of the channel, which would prevent meaningful results of this analysis. In future simulation setups, this point has to be considered.

These preliminary leads are promising. However, there are many open questions that will require substantial analysis. First, we must verify how large the effect of PH-tilting and Gly 77 rotation actually is during the simulations. If we do find these changes to be significant, we can start assessing how strong the correlation between PH-tilting, SF rearrangement and Gly 99 rotation is. We would then be most interested in the causal relation of these rearrangements and plan to address this question by enforcing each of these changes separately using an essential dynamics restraint and monitor the resulting changes at the other locations.

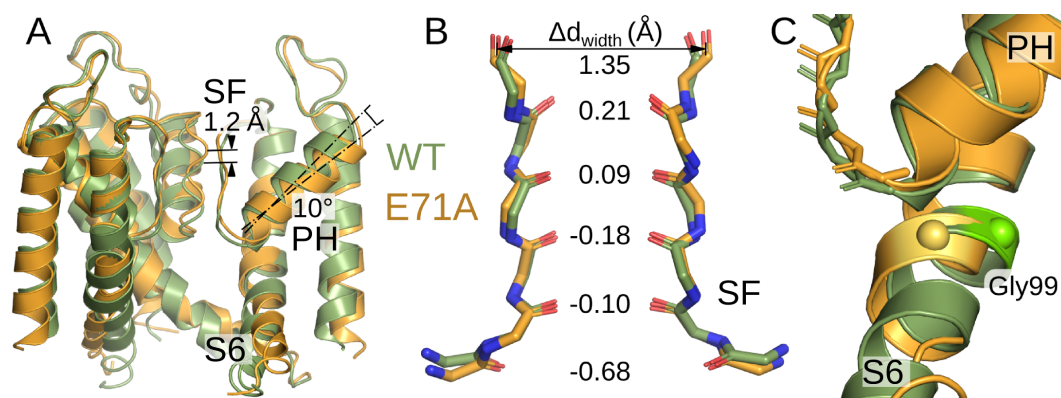


Figure 8.4: **Structures representing the largest difference between the WT and E71A mutant as predicted by FMA.** (A) Direct comparison of the most representative structure of the WT (green) with the most representative structure of the E71A mutant (orange). Three major differences are the upward shift of the SF, tilt of the PH and rearrangements in the middle and lower part of the S6 helix. (B) From the difference between WT and E71A carbonyl distances we see that the mutant widens at the extracellular mouth and tightens at the intracellular side. (C) Gly 99 rotates along the S6 helix such that it is facing the lower tip of the pore helix (PH) in the structure associated with the E71A mutant, whereas it is facing outwards in the WT.



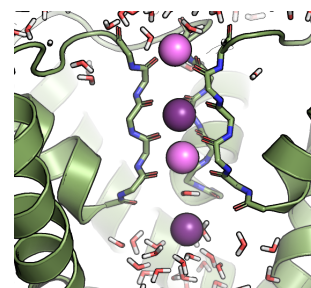
### 8.3.2 Mechanism of the inactivation process

As described above, the FMA has revealed structural rearrangements of the SF. At first glance, these changes on the order of 0.1 Å may seem subtle, however, as shown in chapter 6, even very subtle changes in the SF geometry can have a drastic effect on the ion conductance of the channel. Knowing that these changes mark the strongest difference between the inactivating WT and the non-inactivating E71A mutant offers room for speculation what this inactivated state might look like. Still observing significant currents during the simulations speaks against an inactivated state in the WT, although an onset of inactivation might offer an explanation why the observed currents are still a factor 2-4 below the experimentally observed values. The observed difference might then nonetheless hint at the direction of inactivation. Seeing how even extremely subtle changes in the hydrogen bond network strongly alter the SF conductance, as we have shown in hERG in chapter 4, it would be very much surprising if the observed shift of the entire SF by 1.2 Å would not influence the SF conductance. As we have shown in chapter 6, a tight coordination of the ions with negatively charged coordinating backbone carbonyl-oxygen atoms is essential to allow the highly charged  $K^+$  ions to be closely coordinated. We therefore propose as a working hypothesis that a further steepening of the PH angle would widen the SF at the intracellular side, further spreading the coordinating carbonyl-oxygen atoms. The resulting absence of a tight coordination at the intracellular entrance would then prevent arriving ions from being accommodated at the lowest binding site and therefore stall the permeation process.

To test this hypothesis, we will analyze the present data for a potential correlation between the PH angle and the observed current. Furthermore, we will conduct simulations monitoring the current in channels with an enforced tilt angle of the PH.

## 8.4 Conclusions

Our FMA-based comparison between simulations of the KcsA WT and the non-inactivating E71A mutant has alluded to an intriguing mechanism. This mechanism connects rearrangements of the SF to an axial rotation of the “gating-joint” of the S5 helix mediated via a tilt of the PH. We propose that this PH tilting is the missing link in a mechanistic picture coupling inactivation and gating. Furthermore, we believe that the subtle rearrangements in the SF are a promising vantage point for further analysis targeted at unveiling the nature of the inactivation process.



## 9. Summary and Conclusions

Throughout this thesis we have focused on a deeper understanding of the SF, which is responsible for many of the fascinating features that render  $K^+$  channels invaluable parts in all living cells. This narrowest passage composed of only 4-6 amino acids at the interface of the four subunits is not only the source of inactivation, it also implements the remarkable ion selectivity while allowing almost barrier-less passage for permeable ions such as  $K^+$ . Using MD simulations, we were able to study the motions and interactions of this structure with a temporal and spatial resolution unmatched by experimental techniques while at the same time thoroughly assessing the quality of our models to experimental results.

### 9.1 Ion permeation through the SF

The first group of questions addressed in this thesis dealt with how the SF mediates the transition of  $K^+$  ions. Here, arguably the largest advancement was to show how the  $K^+$  ion pass through the SF with direct ionic contacts and without interspersed water molecules as shown in chapter 5. Based on a comparison to crystallographic data with state of the art tools, we propose that these direct ionic contacts do not only exist, but are the actual driving force behind the fast ion permeation process. As this prospect is in contrast to the earlier consensus in the field, our findings should lead to an alternative interpretation of crystal structures and MD based free energy calculations which had been based upon the assumption of interspersed water molecules.

Using this established protocol for simulating ionic currents, we revealed how the SF mediates these fast transitions by analyzing the concerted structural changes that coincide with the transition of ions. In chapter 6, we show how the SF-forming backbone carbonyl-oxygen atoms play an active role in this process by moving in between the closely packed and highly charged ions. As shown by our results, their role has to be understood as chaperones guiding the permeating ions rather than acting like swinging doors that have to be pushed aside as the ions move past them. This idea of an active stabilization of the ions by the selectivity filter will help our understanding of how alterations of the structure affect the conductance

and selectivity.

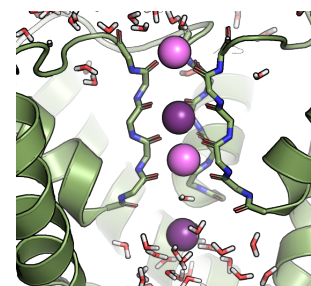
The so far final step in our endeavor to understand the ion permeation through the SF was presented in chapter 7, where we tested if our MD simulations are capable of reproducing the channel selectivity of  $K^+$  ions over  $Na^+$  ions. Indeed, our results show a clear preference for  $K^+$  during prolonged simulations with KcsA. The present analysis indicates that  $Na^+$  ions are less likely to enter the SF as compared to  $K^+$  ions. If they do enter at high voltages, they significantly stall the channel conductance. As far as we can presently tell, these findings are in good agreement with an established kinetic model and suggest that  $Na^+$  ions face a large entry barrier to the SF. However, opposed to these results, a complementary analysis based on “free energy landscapes” as calculated from the density profiles of the ions suggests no such barrier for  $Na^+$  ions. Further effort will therefore be dedicated to resolve this discrepancy, which after all, should be targeted primarily towards the right interpretation of the results, as the effect of ion selectivity is undoubtedly present in the simulations. We are convinced that these simulations, with their temporal and spatial resolution on the one hand, and direct comparability to the experiments on the other hand, will be an excellent tool to test a large number of established models and should give deep insights into the secrets of the  $K^+$  channel function.

Overall, we conclude that MD simulations are a valuable tool to advance our understanding of the ion permeation process. They were capable of bridging the gap between the structural information from crystallography and results about the dynamics from electrophysiology and giving new insights on the mechanics of the ion permeation contributing to complete our picture of  $K^+$  channels physiology and functionality.

## 9.2 Changes of the SF structure

The second group of questions was concerned with changes of the SF structure and how these changes affect the SF conductance. In chapter 4, we laid out, how delicately the SF is embedded into the structure of the channel suspended in a far reaching system of hydrogen bonds. We have shown how sensitive the structure reacts to changes of this environment by varying one particular interaction directly behind the SF. Altering this interaction, we were able to switch the SF between its ordered state and a structure resembling the disordered state. Furthermore, our simulations could predict the impact on the channel inactivation kinetics of conservative mutations altering the hydrogen bond network around the SF. All in all, these findings should prove useful in the search for a mechanistic picture of inactivation.

The most direct account of SF changes impacting on the channel conductance



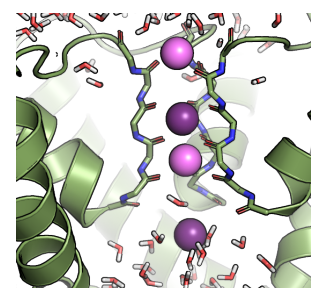
was given in chapter 6. We found that during the ion permeation process, the SF takes on two distinct poses, which differ only on a sub Ångström-scale and correspond to two ionic conformations encountered during the permeation process. We demonstrated how the sensitive balance of these two states, which is necessary for efficient ion conductance, can be disturbed by systematically restricting the flexibility of the SF. Such a reaction to even small perturbations fits well with the experimentally observed sensitivity to small changes in the vicinity of the SF. Here, even very conservative mutations can strongly alter the inactivation kinetics and ion selectivity as we have shown in chapter 4. This sensitivity is exploited in the large  $K^+$  channel family and offers a vast array of different channel kinetics that go back to minor alterations of the channel sequence.

In the very last chapter 8 we widened our analysis to include the whole pore region of the  $K^+$  channel. We set out to find mechanistic evidence for the known coupling between the gating of the S6 helices and the SF associated C-type inactivation. Using functional mode analysis to assess the main structural differences between the WT and the non-inactivating E71A mutant, we found a tilt of the pore helices capable of coupling the raising and lowering of the SF and also an axial rotation of the S6 helix. Although this structural difference between the WT and the mutant is very significant, further tests will need to demonstrate if these changes are capable of coupling gating and C-type inactivation.

## 10. Outlook

In this thesis we have demonstrated how MD simulations can be used to combine the static structural data from crystal structures with the dynamic functional data from electrophysiology. This connection grants insights into the atomistic mechanisms constituting the remarkable features of  $K^+$  channels such as fast ion permeation at high ion selectivity. This approach of structural modeling has been pursued since the first resolved crystal structures were available, but especially recent advances in computing power allow simulations on timescales relevant to  $K^+$  channel physiology. Here, our contribution was to show how MD simulations can model the passage of ions through the SF under physiological conditions, simply by applying a trans-membrane voltage. These types of simulations allow a direct comparison with the the experimental single channel recordings to validate the results. We have already demonstrated how the simulations are capable of modeling core functional principles of the channel such as the ion selectivity.

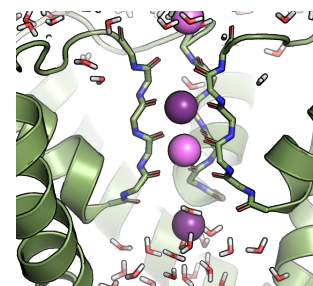
Now, with ever increasing computational power, and growing experience with the channel structures, we should be able to address long standing hypotheses. These tests are not limited to the selectivity and different modes of gating but could also be applied to investigate the interactions with small molecules and eventually even other proteins that are of medical interest. There are high hopes that a deep and profound understanding of the channel mechanics will help in the development of very specific drugs and ultimately in the treatment of a wide array of today's untreatable diseases.



## Bibliography

- [1] Bertil Hille. *Ion Channels of Excitable Membranes*. Sunderland, MA: Sinauer, third edition, 2001.
- [2] Rainer Klinke, Hans-Christian Pape, Armin Kurtz, and Stefan Silbernagl. *Physiologie*. Thieme, Stuttgart; New York, NY, auflage: 6., vollständig überarbeitete auflage edition, November 2009.
- [3] Gary Yellen. The voltage-gated potassium channels and their relatives. *Nature*, 419(6902):35–42, September 2002.
- [4] J. I. Schroeder, R. Hedrich, and J. M. Fernandez. Potassium-selective single channels in guard cell protoplasts of *Vicia faba*. *Nature*, 312(5992):361–362, November 1984.
- [5] F J Maathuis, A M Ichida, D Sanders, and J I Schroeder. Roles of higher plant K<sup>+</sup> channels. *Plant Physiology*, 114(4):1141–1149, August 1997.
- [6] A. L. Hodgkin and R. D. Keynes. The potassium permeability of a giant nerve fibre. *The Journal of Physiology*, 128(1):61–88, April 1955.
- [7] Julius Bernstein. Untersuchungen zur Thermodynamik der bioelektrischen Ströme. *Archiv für die gesamte Physiologie des Menschen und der Tiere*, 92(10-12):521–562, November 1902.
- [8] Kenneth S. Cole and Howard J. Curtis. Electric Impedance of the Squid Giant Axon During Activity. *The Journal of General Physiology*, 22(5):649–670, May 1939.
- [9] A. L. Hodgkin and A. F. Huxley. Action Potentials Recorded from Inside a Nerve Fibre. *Nature*, 144:710–711, October 1939.
- [10] E. Neher and B. Sakmann. Single-channel currents recorded from membrane of denervated frog muscle fibres. *Nature*, 260(5554):799–802, April 1976.

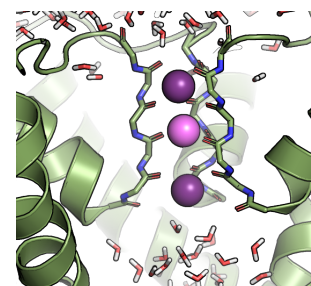
- [11] Lily Yeh Jan and Yuh Nung Jan. Cloned Potassium Channels from Eukaryotes and Prokaryotes. *Annual Review of Neuroscience*, 20(1):91–123, 1997.
- [12] M. C SANGUINETTI and P. S SPECTOR. Potassium Channelopathies. *Neuropharmacology*, 36(6):755–762, June 1997.
- [13] William A. Coetzee, Yimy Amarillo, Joanna Chiu, Alan Chow, David Lau, Tom McCORMACK, Herman Morena, Marcela S. Nadal, Ander Ozaita, David Pountney, Michael Saganich, Eleazar Vega-Saenz De Miera, and Bernardo Rudy. Molecular Diversity of K<sup>+</sup> Channels. *Annals of the New York Academy of Sciences*, 868(1):233–255, 1999.
- [14] S. Grissmer, A. N. Nguyen, J. Aiyar, D. C. Hanson, R. J. Mather, G. A. Gutman, M. J. Karmilowicz, D. D. Auperin, and K. G. Chandy. Pharmacological characterization of five cloned voltage-gated K<sup>+</sup> channels, types Kv1.1, 1.2, 1.3, 1.5, and 3.1, stably expressed in mammalian cell lines. *Molecular Pharmacology*, 45(6):1227–1234, June 1994.
- [15] Declan A. Doyle, Joao Morais Cabral, Richard A. Pfuetzner, Anling Kuo, Jacqueline M. Gulbis, Steven L. Cohen, Brian T. Chait, and Roderick MacKinnon. The Structure of the Potassium Channel: Molecular Basis of K<sup>+</sup> Conduction and Selectivity. *Science*, 280(5360):69–77, April 1998.
- [16] Stephen B. Long, Xiao Tao, Ernest B. Campbell, and Roderick MacKinnon. Atomic structure of a voltage-dependent K<sup>+</sup> channel in a lipid membrane-like environment. *Nature*, 450(7168):376–382, November 2007.
- [17] Stephen B. Long, Ernest B. Campbell, and Roderick MacKinnon. Crystal Structure of a Mammalian Voltage-Dependent Shaker Family K<sup>+</sup> Channel. *Science*, 309(5736):897–903, August 2005.
- [18] Sheng Ye, Yang Li, and Youxing Jiang. Novel insights into K<sup>+</sup> selectivity from high resolution structures of an open K<sup>+</sup> channel pore. *Nature structural & molecular biology*, 17(8):1019–1023, August 2010.
- [19] Simon Bernèche and Benoît Roux. Molecular Dynamics of the KcsA K<sup>+</sup> Channel in a Bilayer Membrane. *Biophysical Journal*, 78(6):2900–2917, June 2000.
- [20] Morten Ø Jensen, David W. Borhani, Kresten Lindorff-Larsen, Paul Maragakis, Vishwanath Jogini, Michael P. Eastwood, Ron O. Dror, and David E. Shaw. Principles of conduction and hydrophobic gating in K<sup>+</sup> channels. *Proceedings of the National Academy of Sciences*, 107(13):5833–5838, March 2010.



- [21] Philip W. Fowler, Enrique Abad, Oliver Beckstein, and Mark S. P. Sansom. Energetics of Multi-Ion Conduction Pathways in Potassium Ion Channels. *Journal of Chemical Theory and Computation*, 9(11):5176–5189, November 2013.
- [22] Carmen Domene and Mark S. P. Sansom. Potassium Channel, Ions, and Water: Simulation Studies Based on the High Resolution X-Ray Structure of KcsA. *Biophysical Journal*, 85(5):2787–2800, November 2003.
- [23] Sergei Yu Noskov, Simon Bernèche, and Benoît Roux. Control of ion selectivity in potassium channels by electrostatic and dynamic properties of carbonyl ligands. *Nature*, 431(7010):830–834, October 2004.
- [24] B. Rudy. Diversity and ubiquity of K channels. *Neuroscience*, 25(3):729–749, June 1988.
- [25] Alexander Kamb, Julie Tseng-Crank, and Mark A. Tanouye. Multiple products of the drosophila Shaker gene may contribute to potassium channel diversity. *Neuron*, 1(5):421–430, July 1988.
- [26] W Stühmer, J P Ruppersberg, K H Schröter, B Sakmann, M Stocker, K P Giese, A Perschke, A Baumann, and O Pongs. Molecular basis of functional diversity of voltage-gated potassium channels in mammalian brain. *The EMBO Journal*, 8(11):3235–3244, November 1989.
- [27] J. Peter Ruppersberg, Klaus H. Schröter, Bert Sakmann, Martin Stocker, Sabine Sewing, and Olaf Pongs. Heteromultimeric channels formed by rat brain potassium-channel proteins. *Nature*, 345(6275):535–537, June 1990.
- [28] Gary Yellen. The moving parts of voltage-gated ion channels. *Quarterly Reviews of Biophysics*, 31(03):239–295, August 1998.
- [29] Krishnan Ramanathan, Timothy H. Michael, Guo-Jian Jiang, Hakim Hiel, and Paul A. Fuchs. A Molecular Mechanism for Electrical Tuning of Cochlear Hair Cells. *Science*, 283(5399):215–217, January 1999.
- [30] Christopher Miller. An overview of the potassium channel family. *Genome Biology*, 1(4):1–5, October 2000.
- [31] Oliver B. Clarke, Alessandro T. Caputo, Adam P. Hill, Jamie I. Vandenberg, Brian J. Smith, and Jacqueline M. Gulbis. Domain Reorientation and Rotation of an Intracellular Assembly Regulate Conduction in Kir Potassium Channels. *Cell*, 141(6):1018–1029, June 2010.

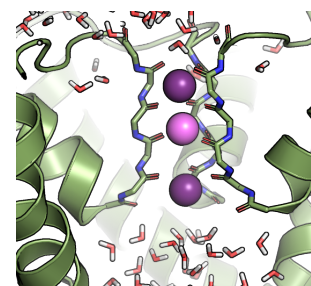


- [32] Vassiliy N. Bavro, Rita De Zorzi, Matthias R. Schmidt, João R. C. Muniz, Lejla Zubcevic, Mark S. P. Sansom, Catherine Vénien-Bryan, and Stephen J. Tucker. Structure of a KirBac potassium channel with an open bundle crossing indicates a mechanism of channel gating. *Nature Structural & Molecular Biology*, 19(2):158–163, February 2012.
- [33] Anling Kuo, Jacqueline M. Gulbis, Jennifer F. Antcliff, Tahmina Rahman, Edward D. Lowe, Jochen Zimmer, Jonathan Cuthbertson, Frances M. Ashcroft, Takayuki Ezaki, and Declan A. Doyle. Crystal Structure of the Potassium Channel KirBac1.1 in the Closed State. *Science*, 300(5627):1922–1926, June 2003.
- [34] Meredith LeMasurier, Lise Heginbotham, and Christopher Miller. Kcsa It's a Potassium Channel. *The Journal of General Physiology*, 118(3):303–314, September 2001.
- [35] Youxing Jiang, Alice Lee, Jiayun Chen, Martine Cadene, Brian T. Chait, and Roderick MacKinnon. Crystal structure and mechanism of a calcium-gated potassium channel. *Nature*, 417(6888):515–522, May 2002.
- [36] Jason G. McCoy and Crina M. Nimigean. Structural correlates of selectivity and inactivation in potassium channels. *Biochimica et Biophysica Acta (BBA) - Biomembranes*, 1818(2):272–285, February 2012.
- [37] Luis G. Cuello, Vishwanath Jogini, D. Marien Cortes, Albert C. Pan, Dominique G. Gagnon, Olivier Dalmas, Julio F. Cordero-Morales, Sudha Chakrapani, Benoit Roux, and Eduardo Perozo. Structural basis for the coupling between activation and inactivation gates in K<sup>+</sup> channels. *Nature*, 466(7303):272–275, July 2010.
- [38] L. Heginbotham and R. MacKinnon. Conduction properties of the cloned Shaker K<sup>+</sup> channel. *Biophysical Journal*, 65(5):2089–2096, November 1993.
- [39] Crina M. Nimigean and Christopher Miller. Na<sup>+</sup> Block and Permeation in a K<sup>+</sup> Channel of Known Structure. *The Journal of General Physiology*, 120(3):323–335, September 2002.
- [40] Christopher Miller. See potassium run. *Nature*, 414(6859):23–24, November 2001.
- [41] João H. Morais-Cabral, Yufeng Zhou, and Roderick MacKinnon. Energetic optimization of ion conduction rate by the K<sup>+</sup> selectivity filter. *Nature*, 414(6859):37–42, November 2001.



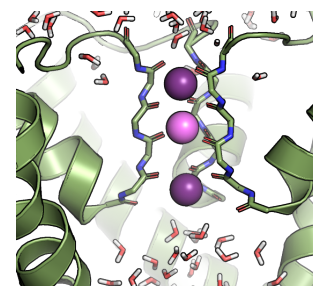
- [42] Simon Bernèche and Benoît Roux. Energetics of ion conduction through the K<sup>+</sup> channel. *Nature*, 414(6859):73–77, November 2001.
- [43] L Heginbotham, Z Lu, T Abramson, and R MacKinnon. Mutations in the K<sup>+</sup> channel signature sequence. *Biophysical Journal*, 66(4):1061–1067, April 1994.
- [44] Alexei Verkhratsky, O. A. Krishtal, and Ole H. Petersen. From Galvani to patch clamp: the development of electrophysiology. *Pflügers Archiv*, 453(3):233–247, October 2006.
- [45] Shunsuke Imai, Masanori Osawa, Koh Takeuchi, and Ichio Shimada. Structural basis underlying the dual gate properties of KcsA. *Proceedings of the National Academy of Sciences*, 107(14):6216–6221, April 2010.
- [46] Luis G. Cuello, Vishwanath Jogini, D. Marien Cortes, and Eduardo Perozo. Structural mechanism of C-type inactivation in K<sup>+</sup> channels. *Nature*, 466(7303):203–208, July 2010.
- [47] Simon Bernèche and Benoît Roux. A Gate in the Selectivity Filter of Potassium Channels. *Structure*, 13(4):591–600, April 2005.
- [48] Michael C. Sanguinetti and Martin Tristani-Firouzi. hERG potassium channels and cardiac arrhythmia. *Nature*, 440(7083):463–469, March 2006.
- [49] Y Zhou, J H Morais-Cabral, A Kaufman, and R MacKinnon. Chemistry of ion coordination and hydration revealed by a K<sup>+</sup> channel-Fab complex at 2.0 Å resolution. *Nature*, 414(6859):43–48, November 2001.
- [50] Prasanna K. Devaraneni, Alexander G. Komarov, Corey A. Costantino, Jordan J. Devereaux, Kimberly Matulef, and Francis I. Valiyaveetil. Semisynthetic K<sup>+</sup> channels show that the constricted conformation of the selectivity filter is not the C-type inactivated state. *Proceedings of the National Academy of Sciences*, 110(39):15698–15703, September 2013.
- [51] Julio F. Cordero-Morales, Vishwanath Jogini, Sudha Chakrapani, and Eduardo Perozo. A Multipoint Hydrogen-Bond Network Underlying KcsA C-Type Inactivation. *Biophysical Journal*, 100(10):2387–2393, May 2011.
- [52] Wayland W. L. Cheng, Jason G. McCoy, Ameer N. Thompson, Colin G. Nichols, and Crina M. Nimigea. Mechanism for selectivity-inactivation coupling in KcsA potassium channels. *Proceedings of the National Academy of Sciences*, 108(13):5272–5277, March 2011.

- [53] Julio F Cordero-Morales, Luis G Cuello, Yanxiang Zhao, Vishwanath Jogini, D Marien Cortes, Benoit Roux, and Eduardo Perozo. Molecular determinants of gating at the potassium-channel selectivity filter. *Nature Structural & Molecular Biology*, 13(4):311–318, March 2006.
- [54] Ulrich Zachariae, Robert Schneider, Phanindra Velisetty, Adam Lange, Daniel Seeliger, Sören J. Wacker, Yasmin Karimi-Nejad, Gert Vriend, Stefan Becker, Olaf Pongs, Marc Baldus, and Bert L. de Groot. The Molecular Mechanism of Toxin-Induced Conformational Changes in a Potassium Channel: Relation to C-Type Inactivation. *Structure*, 16(5):747–754, May 2008.
- [55] Julio F Cordero-Morales, Vishwanath Jogini, Anthony Lewis, Valeria Vasquez, D Marien Cortes, Benoit Roux, and Eduardo Perozo. Molecular driving forces determining potassium channel slow inactivation. *Nature Structural & Molecular Biology*, 14(11):1062–1069, November 2007.
- [56] Edward C. Cooper and Lily Yeh Jan. Ion channel genes and human neurological disease: Recent progress, prospects, and challenges. *Proceedings of the National Academy of Sciences*, 96(9):4759–4766, April 1999.
- [57] Thomas J. Jentsch. Neuronal KCNQ potassium channels: physiology and role in disease. *Nature Reviews Neuroscience*, 1(1):21–30, October 2000.
- [58] Frank Lehmann-Horn and Karin Jurkat-Rott. Voltage-Gated Ion Channels and Hereditary Disease. *Physiological Reviews*, 79(4):1317–1372, January 1999.
- [59] Sarah E. Flanagan, Ann-Marie Patch, Deborah J. G. Mackay, Emma L. Edghill, Anna L. Gloyn, David Robinson, Julian P. H. Shield, Karen Temple, Sian Ellard, and Andrew T. Hattersley. Mutations in ATP-Sensitive K<sup>+</sup> Channel Genes Cause Transient Neonatal Diabetes and Permanent Diabetes in Childhood or Adulthood. *Diabetes*, 56(7):1930–1937, July 2007.
- [60] Walter Stühmer, Frauke Alves, Franziska Hartung, Marta Zientkowska, and Luis A. Pardo. Potassium channels as tumour markers. *FEBS Letters*, 580(12):2850–2852, May 2006.
- [61] Christine Beeton, Heike Wulff, Nathan E. Standifer, Philippe Azam, Katherine M. Mullen, Michael W. Pennington, Aaron Kolski-Andreaco, Eric Wei, Alexandra Grino, Debra R. Counts, Ping H. Wang, Christine J. LeeHealey, Brian S. Andrews, Ananthakrishnan Sankaranarayanan, Daniel Homerick, Werner W. Roeck, Jamshid Tehranzadeh, Kimber L. Stanhope, Pavel Zimin, Peter J. Havel, Stephen Griffey, Hans-Guenther Knaus, Gerald T. Nepom,



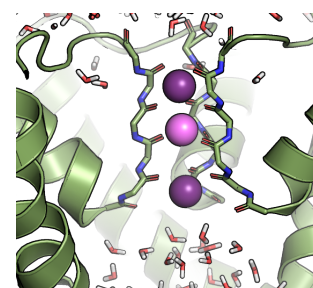
- George A. Gutman, Peter A. Calabresi, and K. George Chandy. Kv1.3 channels are a therapeutic target for T cell-mediated autoimmune diseases. *Proceedings of the National Academy of Sciences*, 103(46):17414–17419, November 2006.
- [62] Heike Wulff, Peter A. Calabresi, Rameeza Allie, Sung Yun, Michael Pennington, Christine Beeton, and K. George Chandy. The voltage-gated Kv1.3 K<sup>+</sup> channel in effector memory T cells as new target for MS. *The Journal of clinical investigation*, 111(11):1703–1713, 2003.
- [63] Joseph C. Koster, M. Alan Permutt, and Colin G. Nichols. Diabetes and Insulin Secretion The ATP-Sensitive K<sup>+</sup> Channel (KATP) Connection. *Diabetes*, 54(11):3065–3072, November 2005.
- [64] Christoffel Jos van Boxtel, Budiono Santoso, and I. Ralph Edwards. *Drug Benefits and Risks: International Textbook of Clinical Pharmacology*. IOS Press, January 2008.
- [65] ionictransport.com. Assessing Astemizole, 2000.
- [66] drugs.com. Astemizole medical facts from Drugs.com, 2000.
- [67] Carsten Kutzner, Helmut Grubmüller, Bert L. de Groot, and Ulrich Zachariae. Computational Electrophysiology: The Molecular Dynamics of Ion Channel Permeation and Selectivity in Atomistic Detail. *Biophysical Journal*, 101(4):809–817, August 2011.
- [68] Tatyana Krivobokova, Rodolfo Briones, Jochen S. Hub, Axel Munk, and Bert L. de Groot. Partial Least-Squares Functional Mode Analysis: Application to the Membrane Proteins AQP1, Aqy1, and CLC-ec1. *Biophysical Journal*, 103(4):786–796, August 2012.
- [69] M. P. Allen and D. J. Tildesley. *Computer simulation of liquids*. Clarendon Press, 1987.
- [70] Daan Frenkel and Berend Smit. *Understanding Molecular Simulation: From Algorithms to Applications*. Academic Press, October 2001.
- [71] D. C. Rapaport. *The Art of Molecular Dynamics Simulation*. Cambridge University Press, April 2004.
- [72] Martin Karplus and J. Andrew McCammon. Molecular dynamics simulations of biomolecules. *Nature Structural & Molecular Biology*, 9(9):646–652, September 2002.

- [73] Riccardo Baron, Indira Chandrasekhar, Markus Christen, Xavier Daura, Peter Gee, Daan P. Geerke, Alice Glättli, Philippe H. Hünenberger, Mika A. Kastenholz, Chris Oostenbrink, Merijn Schenk, Daniel Trzesniak, Nico F. A. van der Vegt, and Haibo B. Yu. Biomolecular Modeling: Goals, Problems, Perspectives. *Angewandte Chemie International Edition*, 45(25):4064–4092, 2006.
- [74] Tamar Schlick, Rosana Collepardo-Guevara, Leif Arthur Halvorsen, Segun Jung, and Xia Xiao. Biomolecular modeling and simulation: a field coming of age. *Quarterly Reviews of Biophysics*, 44(02):191–228, May 2011.
- [75] Shuichi Miyamoto and Peter A. Kollman. Settle: An analytical version of the SHAKE and RATTLE algorithm for rigid water models. *Journal of Computational Chemistry*, 13(8):952–962, 1992.
- [76] Berk Hess, Henk Bekker, Herman J. C Berendsen, and Johannes G. E. M Fraaije. LINCS: A linear constraint solver for molecular simulations. *Journal of Computational Chemistry*, 18(12):1463–1472, September 1997.
- [77] K. Anton Feenstra, Berk Hess, and Herman J. C. Berendsen. Improving efficiency of large time-scale molecular dynamics simulations of hydrogen-rich systems. *Journal of Computational Chemistry*, 20(8):786–798, June 1999.
- [78] Viktor Hornak, Robert Abel, Asim Okur, Bentley Strockbine, Adrian Roitberg, and Carlos Simmerling. Comparison of multiple Amber force fields and development of improved protein backbone parameters. *Proteins: Structure, Function, and Bioinformatics*, 65(3):712–725, November 2006.
- [79] B. R. Brooks, C. L. Brooks, A. D. Mackerell, L. Nilsson, R. J. Petrella, B. Roux, Y. Won, G. Archontis, C. Bartels, S. Boresch, A. Caflisch, L. Caves, Q. Cui, A. R. Dinner, M. Feig, S. Fischer, J. Gao, M. Hodoscek, W. Im, K. Kuczera, T. Lazaridis, J. Ma, V. Ovchinnikov, E. Paci, R. W. Pastor, C. B. Post, J. Z. Pu, M. Schaefer, B. Tidor, R. M. Venable, H. L. Woodcock, X. Wu, W. Yang, D. M. York, and M. Karplus. CHARMM: The biomolecular simulation program. *Journal of Computational Chemistry*, 30(10):1545–1614, 2009.
- [80] Chris Oostenbrink, Alessandra Villa, Alan E. Mark, and Wilfred F. Van Gunsteren. A biomolecular force field based on the free enthalpy of hydration and solvation: The GROMOS force-field parameter sets 53a5 and 53a6. *Journal of Computational Chemistry*, 25(13):1656–1676, 2004.
- [81] George A. Kaminski, Richard A. Friesner, Julian Tirado-Rives, and William L. Jorgensen. Evaluation and Reparametrization of the OPLS-AA Force Field for Proteins via Comparison with Accurate Quantum Chemical



- Calculations on Peptides†. *The Journal of Physical Chemistry B*, 105(28):6474–6487, 2001.
- [82] Minoru Saito. Molecular dynamics simulations of proteins in solution: Artifacts caused by the cutoff approximation. *The Journal of Chemical Physics*, 101(5):4055–4061, September 1994.
- [83] Tom Darden, Darrin York, and Lee Pedersen. Particle mesh Ewald: An  $N \log(N)$  method for Ewald sums in large systems. *The Journal of Chemical Physics*, 98(12):10089, 1993.
- [84] Berk Hess, Carsten Kutzner, David van der Spoel, and Erik Lindahl. GRO-MACS 4: Algorithms for Highly Efficient, Load-Balanced, and Scalable Molecular Simulation. *Journal of Chemical Theory and Computation*, 4(3):435–447, March 2008.
- [85] H. J. C. Berendsen, J. P. M. Postma, W. F. van Gunsteren, A. Dinola, and J. R. Haak. Molecular dynamics with coupling to an external bath. *Journal of Chemical Physics*, 81:3684–3690, October 1984.
- [86] Giovanni Bussi, Davide Donadio, and Michele Parrinello. Canonical sampling through velocity rescaling. *The Journal of Chemical Physics*, 126(1):014101, January 2007.
- [87] Arthur R. Von Hippel. *Dielectric Materials and Applications*. Artech House, Incorporated, 1995.
- [88] S. Y. Ho and G. S. Mittal. Electroporation of Cell Membranes: A Review. *Critical Reviews in Biotechnology*, 16(4):349–362, January 1996.
- [89] C. Chen, S. W. Smye, M. P. Robinson, and J. A. Evans. Membrane electroporation theories: a review. *Medical and Biological Engineering and Computing*, 44(1-2):5–14, February 2006.
- [90] James C. Weaver and Yu. A. Chizmadzhev. Theory of electroporation: A review. *Bioelectrochemistry and Bioenergetics*, 41(2):135–160, December 1996.
- [91] J W Warmke and B Ganetzky. A family of potassium channel genes related to eag in *Drosophila* and mammals. *Proceedings of the National Academy of Sciences*, 91(8):3438–3442, April 1994.
- [92] Huizhen Wang, Yiqiang Zhang, Liwen Cao, Hong Han, Jingxiong Wang, Baofeng Yang, Stanley Nattel, and Zhiguo Wang. HERG K<sup>+</sup> Channel, a Regulator of Tumor Cell Apoptosis and Proliferation. *Cancer Research*, 62(17):4843–4848, 2002.

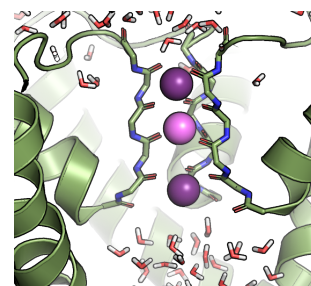
- [93] Paula L. Smith, Thomas Baukrowitz, and Gary Yellen. The inward rectification mechanism of the HERG cardiac potassium channel. *Nature*, 379(6568):833–836, February 1996.
- [94] Anna Stary, Sören J Wacker, Lars Boukharta, Ulrich Zachariae, Yasmin Karimi-Nejad, Johan Aqvist, Gert Vriend, and Bert L de Groot. Toward a consensus model of the HERG potassium channel. *ChemMedChem*, 5(3):455–467, March 2010.
- [95] M T Keating and M C Sanguinetti. Molecular and cellular mechanisms of cardiac arrhythmias. *Cell*, 104(4):569–580, February 2001.
- [96] Igor Splawski, Jiaxiang Shen, Katherine W. Timothy, Michael H. Lehmann, Silvia Priori, Jennifer L. Robinson, Arthur J. Moss, Peter J. Schwartz, Jeffrey A. Towbin, G. Michael Vincent, and Mark T. Keating. Spectrum of Mutations in Long-QT Syndrome Genes : KVLQT1, HERG, SCN5a, KCNE1, and KCNE2. *Circulation*, 102(10):1178 –1185, 2000.
- [97] M E Curran, I Splawski, K W Timothy, G M Vincent, E D Green, and M T Keating. A molecular basis for cardiac arrhythmia: HERG mutations cause long QT syndrome. *Cell*, 80(5):795–803, March 1995.
- [98] John S. Mitcheson. hERG Potassium Channels and the Structural Basis of Drug-Induced Arrhythmias. *Chemical Research in Toxicology*, 21(5):1005–1010, May 2008.
- [99] Jamie Vandenberg, Allan Torres, Terence Campbell, and Philip Kuchel. The HERG K<sup>+</sup> channel: progress in understanding the molecular basis of its unusual gating kinetics. *European Biophysics Journal*, 33:89–97, April 2004.
- [100] Arthur J. Moss, Wojciech Zareba, Elizabeth S. Kaufman, Eric Gartman, Derick R. Peterson, Jesaia Benhorin, Jeffrey A. Towbin, Mark T. Keating, Silvia G. Priori, Peter J. Schwartz, G. Michael Vincent, Jennifer L. Robinson, Mark L. Andrews, Changyong Feng, W. Jackson Hall, Aharon Medina, Li Zhang, and Zhiqing Wang. Increased Risk of Arrhythmic Events in Long-QT Syndrome With Mutations in the Pore Region of the Human Ether-a-go-go-Related Gene Potassium Channel. *Circulation*, 105(7):794–799, February 2002.
- [101] James P. Lees-Miller, Yanjun Duan, Guo Qi Teng, Kelly Thorstad, and Henry J. Duff. Novel Gain-of-Function Mechanism in K<sup>+</sup> Channel-Related Long-QT Syndrome: : Altered Gating and Selectivity in the HERG1 N629d Mutant. *Circ Res*, 86(5):507–513, March 2000.



- [102] Eckhard Ficker, Wolfgang Jarolimek, Johann Kiehn, Arnd Baumann, and Arthur M Brown. Molecular Determinants of Dofetilide Block of HERG K<sup>+</sup> Channels. *Circulation Research*, 82(3):386–395, February 1998.
- [103] Tadashi Nakajima, Tetsushi Furukawa, Toshihiro Tanaka, Yoshifumi Katayama, Ryoza Nagai, Yusuke Nakamura, and Masayasu Hiraoka. Novel Mechanism of HERG Current Suppression in LQT2 : Shift in Voltage Dependence of HERG Inactivation. *Circ Res*, 83(4):415–422, August 1998.
- [104] Matthew Perry, Frank B. Sachse, Jennifer Abbruzzese, and Michael C. Sanguinetti. PD-118057 contacts the pore helix of hERG1 channels to attenuate inactivation and enhance K<sup>+</sup> conductance. *Proceedings of the National Academy of Sciences*, 106(47):20075–20080, November 2009.
- [105] J.M. Cordeiro, R. Brugada, Y.S. Wu, K. Hong, and R. Dumaine. Modulation of IKr inactivation by mutation N588K in KCNH2: A link to arrhythmogenesis in short QT syndrome. *Cardiovascular Research*, 67(3):498–509, 2005.
- [106] Ramon Brugada, Kui Hong, Robert Dumaine, Jonathan Cordeiro, Fiorenzo Gaita, Martin Borggrefe, Teresa M. Menendez, Josep Brugada, Guido D. Pollevick, Christian Wolpert, Elena Burashnikov, Kiyotaka Matsuo, Yue Sheng Wu, Alejandra Guerchicoff, Francesca Bianchi, Carla Giustetto, Rainer Schimpf, Pedro Brugada, and Charles Antzelevitch. Sudden Death Associated With Short-QT Syndrome Linked to Mutations in HERG. *Circulation*, 109(1):30–35, January 2004.
- [107] Ihor Gussak, Pedro Brugada, Josep Brugada, R. Scott Wright, Stephen L. Kopecky, Bernard R. Chaitman, and Preben Bjerregaard. Idiopathic Short QT Interval: A New Clinical Syndrome? *Cardiology*, 94(2):99–102, 2000.
- [108] Lars Boukharta, Henrik Keränen, Anna Stary-Weinzinger, Göran Wallin, Bert L de Groot, and Johan Aqvist. Computer simulations of structure-activity relationships for HERG channel blockers. *Biochemistry*, 50(27):6146–6156, July 2011.
- [109] Maarten G Wolf, Martin Hoefling, Camilo Aponte-Santamaría, Helmut Grubmüller, and Gerrit Groenhof. g\_membed: Efficient insertion of a membrane protein into an equilibrated lipid bilayer with minimal perturbation. *Journal of Computational Chemistry*, 31(11):2169–2174, August 2010.
- [110] O. Berger, O. Edholm, and F. Jähnig. Molecular dynamics simulations of a fluid bilayer of dipalmitoylphosphatidylcholine at full hydration, constant pressure, and constant temperature. *Biophysical Journal*, 72(5):2002–2013, May 1997.

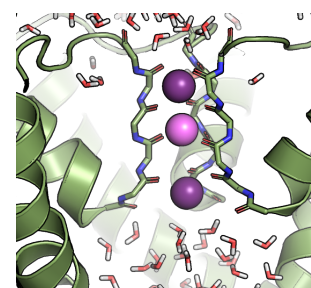


- [111] H. J. C. Berendsen, J. R. Grigera, and T. P. Straatsma. The missing term in effective pair potentials. *J. Phys. Chem.*, 91(24):6269–6271, 1987.
- [112] Vivek Garg, Anna Stary-Weinzinger, Frank Sachse, and Michael C Sanguinetti. Molecular Determinants for Activation of Human Ether-a-Go-Go-Related Gene 1 Potassium Channels by 3-Nitro-N-(4-Phenoxyphenyl) Benzamide. *Molecular Pharmacology*, 80(4):630–637, October 2011.
- [113] Christian Lemmen. Flex X, 2010.
- [114] W Stühmer. Electrophysiological recording from *Xenopus* oocytes. *Methods in Enzymology*, 207:319–339, 1992.
- [115] Shetuan Zhang, Steven J. Kehl, and David Fedida. Modulation of human ether-à-go-go-related K<sup>+</sup> (HERG) channel inactivation by Cs<sup>+</sup> and K<sup>+</sup>. *The Journal of Physiology*, 548(3):691–702, May 2003.
- [116] D.T. Wang, A.P. Hill, S.A. Mann, P.S. Tan, and J.I. Vandenberg. Re-examining the role of the voltage sensor in hERG channel inactivation. 18:25–41, 2011.
- [117] Ulrich Zachariae, Fabrizio Giordanetto, and Andrew G. Leach. Side Chain Flexibilities in the Human Ether-a-go-go Related Gene Potassium Channel (hERG) Together with Matched-Pair Binding Studies Suggest a New Binding Mode for Channel Blockers. *Journal of Medicinal Chemistry*, 52(14):4266–4276, July 2009.
- [118] Phillip J Stansfeld, Alessandro Grottesi, Zara A Sands, Mark S P Sansom, Peter Gedeck, Martin Gosling, Brian Cox, Peter R Stanfield, John S Mitcheson, and Michael J Sutcliffe. Insight into the mechanism of inactivation and pH sensitivity in potassium channels from molecular dynamics simulations. *Biochemistry*, 47(28):7414–7422, July 2008.
- [119] John S. Mitcheson, Jun Chen, Monica Lin, Chris Culberson, and Michael C. Sanguinetti. A structural basis for drug-induced long QT syndrome. *Proceedings of the National Academy of Sciences of the United States of America*, 97(22):12329–12333, October 2000.
- [120] Anruo Zou, Qing P Xu, and Michael C Sanguinetti. A mutation in the pore region of HERG K<sup>+</sup> channels expressed in *Xenopus* oocytes reduces rectification by shifting the voltage dependence of inactivation. *The Journal of Physiology*, 509(1):129–137, May 1998.
- [121] Shimin Wang, Shuguang Liu, Michael J Morales, Harold C Strauss, and Randall L Rasmusson. A quantitative analysis of the activation and inactivation



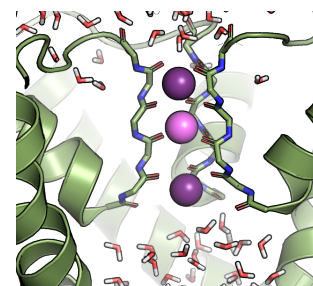
- kinetics of HERG expressed in *Xenopus* oocytes. *The Journal of Physiology*, 502(1):45–60, July 1997.
- [122] E Espinosa, E Molins, and C Lecomte. Hydrogen bond strengths revealed by topological analyses of experimentally observed electron densities. *Chemical Physics Letters*, 285(3-4):170–173, March 1998.
- [123] Jin-Song Bian, Jie Cui, Yonathan Melman, and Thomas V. McDonald. S641 Contributes HERG K<sup>+</sup> Channel Inactivation. *Cell Biochemistry and Biophysics*, 41(1):025–040, 2004.
- [124] S Durdagi, J Subbotina, J Lees-Miller, J Guo, H J Duff, and S Y Noskov. Insights into the molecular mechanism of hERG1 channel activation and blockade by drugs. *Current Medicinal Chemistry*, 17(30):3514–3532, 2010.
- [125] Harry J Witchel. The hERG potassium channel as a therapeutic target. *Expert Opinion on Therapeutic Targets*, 11(3):321–336, March 2007.
- [126] Aaron C Gerlach, Sally J Stoehr, and Neil A Castle. Pharmacological removal of human ether-a-go-go-related gene potassium channel inactivation by 3-nitro-N-(4-phenoxyphenyl) benzamide (ICA-105574). *Molecular Pharmacology*, 77(1):58–68, January 2010.
- [127] Henry Sackin, Mikheil Nanazashvili, Hui Li, Lawrence G. Palmer, and D. Eric Walters. An Intersubunit Salt Bridge near the Selectivity Filter Stabilizes the Active State of Kir1.1. *Biophysical Journal*, 97(4):1058–1066, August 2009.
- [128] Christian Ader, Robert Schneider, Sonke Hornig, Phanindra Velisetty, Erica M Wilson, Adam Lange, Karin Giller, Iris Ohmert, Marie-France Martin-Eauclaire, Dirk Trauner, Stefan Becker, Olaf Pongs, and Marc Baldus. A structural link between inactivation and block of a K<sup>+</sup> channel. *Nature Structural & Molecular Biology*, 15(6):605–612, May 2008.
- [129] David Gómez-Varela, Constanza Contreras-Jurado, Simone Furini, Rafael García-Ferreiro, Walter Stühmer, and Luis A. Pardo. Different relevance of inactivation and F468 residue in the mechanisms of hEag1 channel blockage by astemizole, imipramine and dofetilide. *FEBS Letters*, 580(21):5059–5066, September 2006.
- [130] Jie Liu, Mei Zhang, Min Jiang, and Gea-Ny Tseng. Structural and Functional Role of the Extracellular S5-P Linker in the HERG Potassium Channel. *The Journal of General Physiology*, 120(5):723–737, November 2002.

- [131] Allan M. Torres, Paramjit S. Bansal, Margaret Sunde, Catherine E. Clarke, Jane A. Bursill, David J. Smith, Asne Bauskin, Samuel N. Breit, Terence J. Campbell, Paul F. Alewood, Philip W. Kuchel, and Jamie I. Vandenberg. Structure of the HERG K<sup>+</sup> Channel S5p Extracellular Linker. *Journal of Biological Chemistry*, 278(43):42136–42148, October 2003.
- [132] Yufeng Zhou and Roderick MacKinnon. The Occupancy of Ions in the K<sup>+</sup> Selectivity Filter: Charge Balance and Coupling of Ion Binding to a Protein Conformational Change Underlie High Conduction Rates. *Journal of Molecular Biology*, 333(5):965–975, November 2003.
- [133] Johan Åqvist and Victor Luzhkov. Ion permeation mechanism of the potassium channel. *Nature*, 404(6780):881–884, April 2000.
- [134] Luisa Ceccarini, Matteo Masetti, Andrea Cavalli, and Maurizio Recanatini. Ion Conduction through the hERG Potassium Channel. *PLoS ONE*, 7(11):e49017, November 2012.
- [135] Fatemeh Khalili-Araghi, Emad Tajkhorshid, and Klaus Schulten. Dynamics of K<sup>+</sup> Ion Conduction through Kv1.2. *Biophysical Journal*, 91(6):L72–L74, September 2006.
- [136] Tao Lu, Alice Y. Ting, Joel Mainland, Lily Y. Jan, Peter G. Schultz, and Jian Yang. Probing ion permeation and gating in a K<sup>+</sup> channel with backbone mutations in the selectivity filter. *Nature Neuroscience*, 4(3):239–246, March 2001.
- [137] Indira H. Shrivastava and Mark S.P. Sansom. Simulations of Ion Permeation Through a Potassium Channel: Molecular Dynamics of KcsA in a Phospholipid Bilayer. *Biophysical Journal*, 78(2):557–570, February 2000.
- [138] Takashi Sumikama, Shinji Saito, and Iwao Ohmine. Mechanism of Ion Permeation in a Model Channel: Free Energy Surface and Dynamics of K<sup>+</sup> Ion Transport in an Anion-Doped Carbon Nanotube. *The Journal of Physical Chemistry B*, 110(41):20671–20677, October 2006.
- [139] Morten Ø Jensen, Vishwanath Jogini, Michael P. Eastwood, and David E. Shaw. Atomic-level simulation of current–voltage relationships in single-file ion channels. *The Journal of General Physiology*, 141(5):619–632, May 2013.
- [140] Kota Kasahara, Matsuyuki Shirota, and Kengo Kinoshita. Ion Concentration-Dependent Ion Conduction Mechanism of a Voltage-Sensitive Potassium Channel. *PLoS ONE*, 8(2):e56342, February 2013.



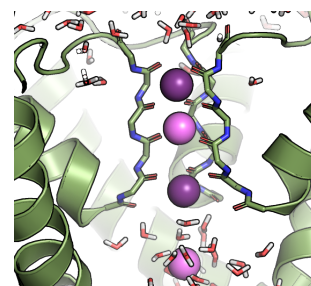
- [141] Simone Furini and Carmen Domene. Atypical mechanism of conduction in potassium channels. *Proceedings of the National Academy of Sciences*, 106(38):16074–16077, September 2009.
- [142] Tobias Linder, Bert L. de Groot, and Anna Stary-Weinzinger. Probing the Energy Landscape of Activation Gating of the Bacterial Potassium Channel KcsA. *PLoS Comput Biol*, 9(5):e1003058, May 2013.
- [143] Simon Bernèche and Benoît Roux. The Ionization State and the Conformation of Glu-71 in the KcsA K<sup>+</sup> Channel. *Biophysical Journal*, 82(2):772–780, February 2002.
- [144] In Suk Joung and Thomas E. Cheatham. Determination of Alkali and Halide Monovalent Ion Parameters for Use in Explicitly Solvated Biomolecular Simulations. *The Journal of Physical Chemistry B*, 112(30):9020–9041, July 2008.
- [145] L. X. Dang. Mechanism and Thermodynamics of Ion Selectivity in Aqueous Solutions of 18-Crown-6 Ether. a Molecular Dynamics Study. *Journal of the American Chemical Society*, 117(26), July 1995.
- [146] Jeffery B. Klauda, Richard M. Venable, J. Alfredo Freites, Joseph W. O'Connor, Douglas J. Tobias, Carlos Mondragon-Ramirez, Igor Vorobyov, Alexander D. MacKerell, and Richard W. Pastor. Update of the CHARMM All-Atom Additive Force Field for Lipids: Validation on Six Lipid Types. *The Journal of Physical Chemistry B*, 114(23):7830–7843, June 2010.
- [147] Benoit Roux and Simon Berneche. On the potential functions used in molecular dynamics simulations of ion channels. *Biophysical Journal*, 82(3):1681–1684, March 2002.
- [148] Martyn D. Winn, Charles C. Ballard, Kevin D. Cowtan, Eleanor J. Dodson, Paul Emsley, Phil R. Evans, Ronan M. Keegan, Eugene B. Krissinel, Andrew G. W. Leslie, Airlie McCoy, Stuart J. McNicholas, Garib N. Murshudov, Navraj S. Pannu, Elizabeth A. Potterton, Harold R. Powell, Randy J. Read, Alexei Vagin, and Keith S. Wilson. Overview of the CCP 4 suite and current developments. *Acta Crystallographica Section D Biological Crystallography*, 67(4):235–242, April 2011.
- [149] Tim Grune. mtz2sca and mtz2hkl : facilitated transition from CCP4 to the SHELX program suite. *Journal of Applied Crystallography*, 41(1):217–218, February 2008.
- [150] George M. Sheldrick. A short history of SHELX. *Acta Crystallographica Section A Foundations of Crystallography*, 64(1):112–122, December 2007.

- [151] Christian B. Hübschle, George M. Sheldrick, and Birger Dittrich. ShelXle: a Qt graphical user interface for SHELXL. *Journal of Applied Crystallography*, 44(6):1281–1284, December 2011.
- [152] L. Kissel and R. H. Pratt. Corrections to tabulated anomalous-scattering factors. *Acta Crystallographica Section A Foundations of Crystallography*, 46(3):170–175, March 1990.
- [153] Axel T. Brünger. [19] Free R value: Cross-validation in crystallography. In Robert M. Sweet Charles W. Carter Jr., editor, *Methods in Enzymology*, volume Volume 277 of *Macromolecular Crystallography Part B*, pages 366–396. Academic Press, 1997.
- [154] Tim Gruene, Hinrich W. Hahn, Anna V. Luebben, Flora Meilleur, and George M. Sheldrick. Refinement of macromolecular structures against neutron data with SHELXL2013. *Journal of Applied Crystallography*, 47(1):462–466, February 2014.
- [155] Andrea Thorn and George M. Sheldrick. ANODE: anomalous and heavy-atom density calculation. *Journal of Applied Crystallography*, 44(6):1285–1287, November 2011.
- [156] Garib N. Murshudov, Pavol Skubák, Andrey A. Lebedev, Navraj S. Pannu, Roberto A. Steiner, Robert A. Nicholls, Martyn D. Winn, Fei Long, and Alexei A. Vagin. REFMAC 5 for the refinement of macromolecular crystal structures. *Acta Crystallographica Section D Biological Crystallography*, 67(4):355–367, April 2011.
- [157] Joshua A. Anderson, Chris D. Lorenz, and A. Travasset. General purpose molecular dynamics simulations fully implemented on graphics processing units. *Journal of Computational Physics*, 227(10):5342–5359, May 2008.
- [158] Yang Li, Ian Berke, Liping Chen, and Youxing Jiang. Gating and Inward Rectifying Properties of the MthK K<sup>+</sup> Channel with and without the Gating Ring. *The Journal of General Physiology*, 129(2):109–120, February 2007.
- [159] Gerhard Hummer, Dikeos Mario Soumpasis, and Martin Neumann. Computer simulations do not support Cl-Cl pairing in aqueous NaCl solution. *Molecular Physics*, 81(5):1155–1163, 1994.
- [160] Motohiko Nishida, Martine Cadene, Brian T. Chait, and Roderick MacKinnon. Crystal structure of a Kir3.1 [U+2010] prokaryotic Kir channel chimera. *The EMBO Journal*, 26(17):4005–4015, September 2007.



- [161] Masayuki Iwamoto and Shigetoshi Oiki. Counting Ion and Water Molecules in a Streaming File through the Open-Filter Structure of the K Channel. *The Journal of Neuroscience*, 31(34):12180–12188, August 2011.
- [162] Torben Hoomann, Nadin Jahnke, Andreas Horner, Sandro Keller, and Peter Pohl. Filter gate closure inhibits ion but not water transport through potassium channels. *Proceedings of the National Academy of Sciences*, page 201304714, June 2013.
- [163] Sapar M. Saparov and Peter Pohl. Beyond the diffusion limit: Water flow through the empty bacterial potassium channel. *Proceedings of the National Academy of Sciences of the United States of America*, 101(14):4805–4809, April 2004.
- [164] Ameer N. Thompson, Ilsoo Kim, Timothy D. Panosian, Tina M. Iverson, Toby W. Allen, and Crina M. Nimigean. Mechanism of potassium-channel selectivity revealed by Na<sup>+</sup> and Li<sup>+</sup> binding sites within the KcsA pore. *Nature Structural & Molecular Biology*, 16(12):1317–1324, December 2009.
- [165] Benoît Roux, Simon Bernèche, Bernhard Egwolf, Bogdan Lev, Sergei Y. Noskov, Christopher N. Rowley, and Haibo Yu. Ion selectivity in channels and transporters. *The Journal of General Physiology*, 137(5):415–426, May 2011.
- [166] Sameer Varma, David M. Rogers, Lawrence R. Pratt, and Susan B. Rempe. Design principles for K<sup>+</sup> selectivity in membrane transport. *The Journal of General Physiology*, 137(6):479–488, June 2011.
- [167] Olaf S. Andersen. Perspectives on: Ion selectivity. *The Journal of General Physiology*, 137(5):393–395, May 2011.
- [168] Amer Alam and Youxing Jiang. Structural studies of ion selectivity in tetrameric cation channels. *The Journal of General Physiology*, 137(5):397–403, May 2011.
- [169] Johan Mahler and Ingmar Persson. A Study of the Hydration of the Alkali Metal Ions in Aqueous Solution. *Inorganic Chemistry*, 51(1):425–438, January 2012.
- [170] L. J. Mullins. An Analysis of Conductance Changes in Squid Axon. *The Journal of General Physiology*, 42(5):1013–1035, May 1959.
- [171] Sameer Varma and Susan B. Rempe. Tuning Ion Coordination Architectures to Enable Selective Partitioning. *Biophysical Journal*, 93(4):1093–1099, August 2007.

- [172] T. W. Allen, A. Bliznyuk, A. P. Rendell, S. Kuyucak, and S.-H. Chung. The potassium channel: Structure, selectivity and diffusion. *The Journal of Chemical Physics*, 112(18):8191–8204, May 2000.
- [173] Francisco Bezanilla and Clay M. Armstrong. Negative Conductance Caused by Entry of Sodium and Cesium Ions into the Potassium Channels of Squid Axons. *The Journal of General Physiology*, 60(5):588–608, November 1972.
- [174] Crina M. Nimigean, Joshua S. Chappie, and Christopher Miller. Electrostatic Tuning of Ion Conductance in Potassium Channels. *Biochemistry*, 42(31):9263–9268, August 2003.
- [175] Crina M. Nimigean and Toby W. Allen. Origins of ion selectivity in potassium channels from the perspective of channel block. *The Journal of General Physiology*, 137(5):405–413, May 2011.
- [176] Benoît Roux. Ion binding sites and their representations by reduced models. *The journal of physical chemistry. B*, 116(23):6966–6979, June 2012.
- [177] Andrej Sali and Ben Webb. Modeller, 2013.



## 11. Appendix

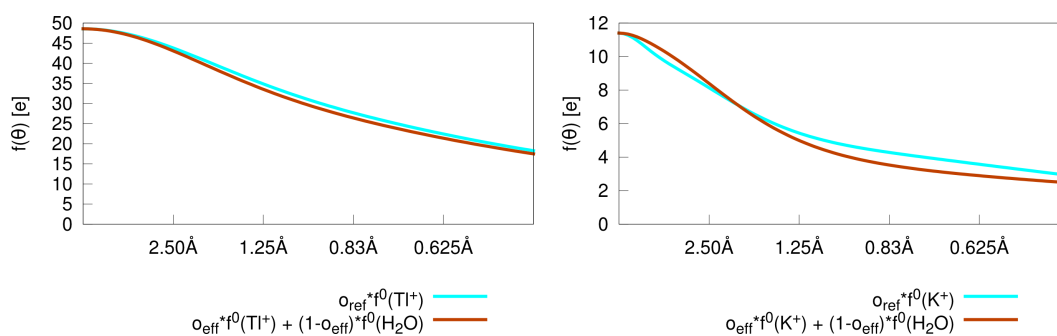


Figure 11.1: The scattering factor from either  $\text{K}^+$  or  $\text{Tl}^+$  compared to a mixture of  $\text{H}_2\text{O}$  and ion with an exemplary occupancy  $o_{ref} = 0.6$ . The difference is only small and justifies the modeling in the crystal structure with an ion only instead of using a mixed state. The latter leads to an unstable refinement.



Table 11.1: Correlation between the occupancy and atomic displacement parameters for the SF ions in PDB structures 1r3j and 3ldc, calculated with full matrix refinement in SHELXL. Despite somewhat lower resolution, 1r3j shows better agreement between anisotropic and isotropic refinement with smaller correlation coefficients. Owing to the I4 symmetry, only the diagonal elements of  $U$  are non-zero in the anisotropic refinement, and  $U_{22} = U_{11}$ . For 1r3j, correlations between occupancy and  $U_{33}$  below 0.72 were not specified further, as SHELXL only lists the 600 strongest correlations.

PDB id: 1r3j		anisotropic refinement				isotropic refinement			
Atom	binding site	occupancy	$U_{11}/U_{22}$	$U_{33}$	occ. correlation with $U_{11}$	$U_{33}$	occupancy	correlation	$U_{iso}$
TL1	S <sub>1</sub>	1.02	0.395	0.281	0.809	<0.72	1.01	0.895	0.358
TL2	S <sub>2</sub>	0.93	0.376	0.219	0.812	0.731	0.92	0.896	0.325
TL3	S <sub>3</sub>	0.92	0.346	0.260	0.816	<0.72	0.90	0.898	0.307
TL4	S <sub>4</sub>	0.99	0.405	0.229	0.807	<0.72	0.98	0.901	0.342

PDB id: 3ldc		anisotropic refinement				isotropic refinement			
Atom	binding site	occupancy	$U_{11}/U_{22}$	$U_{33}$	occ. correlation with $U_{11}$	$U_{33}$	occupancy	correlation	$U_{iso}$
K1	S <sub>1</sub>	0.91	0.223	0.237	0.841	0.706	0.87	0.919	0.221
K2	S <sub>2</sub>	0.78	0.238	0.138	0.830	0.792	0.84	0.925	0.212
K3	S <sub>3</sub>	1.22	0.257	0.284	0.835	0.695	1.15	0.915	0.258
K4	S <sub>4</sub>	1.10	0.242	0.322	0.842	0.644	1.07	0.911	0.263

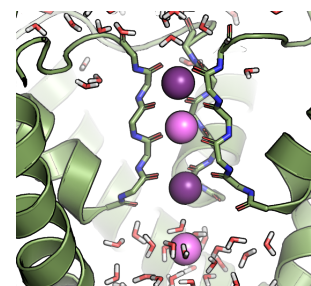


Table 11.2: **Results for occupancy refinement of  $\text{Ti}^+$  in PDB id 1r3j and  $\text{K}^+$  in PDB id 3ldc, respectively.** Standard uncertainties are given where available (SHELXL refinement); n/a means that the anomalous signal was too weak for reliable calculation. (Occupancies greater than one are caused by the correlation between occupancies and B-values.)  $U_{ij}$  values from SHELXL (1r3j, 3ldc) were converted by the standard conversions  $B_{iso} = 8\pi^2/3 (U_{xx}+U_{yy}+U_{zz})$  and  $\sigma_{iso} = 8\pi^2/3 (\sigma_{xx}+\sigma_{yy}+\sigma_{zz})$ . Please see main text and Eq.5.1 for a definition of  $\text{occ}_{ref}$  and  $\text{occ}_{eff}$ .

SHELXL				
1r3j	Ti <sup>+</sup> C401	Ti <sup>+</sup> C402	Ti <sup>+</sup> C403	Ti <sup>+</sup> C404
rel. occ	1.0	0.9	0.9	1.0
abs. $\text{occ}_{ref}$	1.02 (4)	0.93 (3)	0.92 (4)	0.99 (4)
abs. $\text{occ}_{eff}$	1.02 (5)	0.92 (3)	0.91 (5)	0.99 (5)
B(Å <sup>2</sup> )	22 (1)	26 (1)	25 (1)	20 (2)
SHELXL				
3ldc	K <sup>+</sup> A1	K <sup>+</sup> A2	K <sup>+</sup> A3	K <sup>+</sup> A4
rel. occ	n/a	n/a	n/a	n/a
abs. $\text{occ}_{ref}$	0.92 (7)	0.80 (7)	1.00 (8)	1.00 (8)
abs. $\text{occ}_{eff}$	0.81(16)	0.57 (15)	1.00 (16)	1.00 (17)
B(Å <sup>2</sup> )	18 (1)	17 (1)	18 (1)	20 (1)

Table 11.3: Results for occupancy refinement of K<sup>+</sup> in PDB id 2qks from REFMAC5 and SHELXL, respectively. Standard uncertainties are given where available (SHELXL refinement); n/a means that the anomalous signal was too weak for reliable calculation. (Occupancies greater than one are caused by the correlation between occupancies and B-values.)  $U_{ij}$  values from SHELXL (1r3j, 3ldc) were converted by the standard conversions  $B_{iso} = 8\pi^2/3 (U_{xx}+U_{yy}+U_{zz})$  and  $\sigma_{iso} = 8\pi^2/3 (\sigma_{xx}+\sigma_{yy}+\sigma_{zz})$ . Please see main text and Eq. 5.1 for a definition of  $occ_{ref}$  and  $occ_{eff}$

		REFMAC 5							
2qks	K+ A401	K+ A402	K+ A403	K+ A404	K+ B408	K+ B409	K+ B410	K+ B411	
abs. $occ_{ref}$	1.00	1.00	1.00	0.92	0.96	0.92	0.96	0.68	
abs. $occ_{eff}$	1.00	1.00	1.00	0.83	0.92	0.83	0.92	0.32	
B(Å <sup>2</sup> )	33.7	31.8	38.2	60.5	38.7	31.0	40.6	38.7	
2qks*	K+ A401	K+ A402	K+ A403	K+ A404	K+ B408	K+ B409	K+ B410	K+ B411	
abs. $occ_{ref}$	1.00	0.96	1.00	0.84	0.88	0.76	0.80	0.80	
abs. $occ_{eff}$	1.00	0.92	1.00	0.66	0.75	0.49	0.58	0.58	
B(Å <sup>2</sup> )	33.9	30.7	38.5	49.9	34.1	26.6	33.8	56.1	
		SHELXL							
2qks	K+ A401	K+ A402	K+ A403	K+ A404	K+ B408	K+ B409	K+ B410	K+ B411	
abs. $occ_{ref}$	1.0(3)	1.0(4)	1.0(4)	0.5(3)	1.0(4)	0.8(4)	0.9(4)	0.6(3)	
abs. $occ_{eff}$	1.0(6)	1.0(8)	1.0(8)	0.0(6)	1.0(8)	0.6(8)	0.8(8)	0.2(6)	
B(Å <sup>2</sup> )	34(13)	37(14)	42(13)	42(21)	42(19)	39(21)	46(17)	51(22)	
2qks*	K+ A401	K+ A402	K+ A403	K+ A404	K+ B408	K+ B409	K+ B410	K+ B411	
abs. $occ_{ref}$	1.0(7)	1.0(7)	1.0(6)	0.7(5)	1.0(9)	1.0(9)	1.0(7)	0.9(5)	
abs. $occ_{eff}$	1.0(1.5)	1.0(1.5)	1.0(1.3)	0.4(1.1)	1.0(1.9)	1.0(1.9)	1.0(1.5)	0.8(1.0)	
B(Å <sup>2</sup> )	50(32)	50(32)	50(26)	50(27)	54(41)	54(41)	54(32)	55(55)	

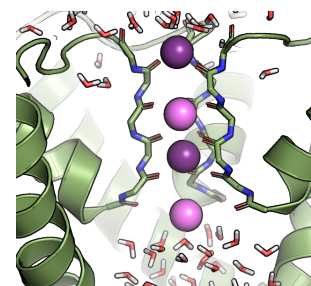


Table 11.4: **Calculated dispersive corrections  $f'(\lambda)$  and  $f''(\lambda)$  for  $K^+$  and  $Tl^+$**  . Dispersive corrections for all other elements were taken into account but only those for S differ significantly from  $0e^-$  [151, 152]

	<b>1r3j (<math>\lambda = 0.9504 \text{ \AA}</math>)</b>		<b>3l1c (<math>\lambda = 0.9794 \text{ \AA}</math>)</b>	
	<b>Tl<sup>+</sup></b>	<b>S</b>	<b>K<sup>+</sup></b>	<b>S</b>
<b><math>f'(e^-)</math></b>	-8.965	0.195	0.298	0.203
<b><math>f''(e^-)</math></b>	9.678	0.224	0.469	0.238

Table 11.5: **Data statistics for the dataset 1r3j, data block r1r3jA, as deposited in the PDB.** Res: Resolution shell; #data: measured number of reflections; #pred: theoretically possible number of reflections; %compl: data completeness, i.e. %compl = #data/#pred. Statistics are from XPREP.

Res. (Å)	# data	# pred.	% compl.	$\langle I/\sigma I \rangle$
$\infty - 8.04$	919	1006	91.4	27.80
8.04–5.43	2150	2156	99.7	27.12
5.43–4.32	3037	3040	99.9	27.65
4.32–3.77	3068	3068	100.0	26.15
3.77– 3.42	3112	3112	100.0	23.85
3.42– 3.18	2974	2975	100.0	21.01
3.18– 2.99	3106	3106	100.0	18.82
2.99– 2.84	3040	3041	100.0	16.01
2.84– 2.71	3221	3221	100.0	13.46
2.71– 2.61	2910	2911	100.0	13.27
2.61– 2.52	3031	3039	99.7	11.52
2.52– 2.44	3092	3096	99.9	9.89
2.44– 2.37	3045	3051	99.8	8.60
2.37– 2.30	3437	3445	99.8	7.68
2.30– 2.25	2705	2711	99.8	6.63
2.25– 2.20	2968	2982	99.5	6.02
2.20– 2.15	3242	3249	99.8	5.50
2.15– 2.10	3574	3591	99.5	4.99
2.10– 2.06	3071	3092	99.3	4.15
2.06– 2.03	2446	2468	99.1	3.84
2.03– 2.00	2900	2938	98.7	3.19
2.10– 2.00	8417	8498	99.0	3.73
$\infty - 2.00$	61048	61292	99.6	13.02

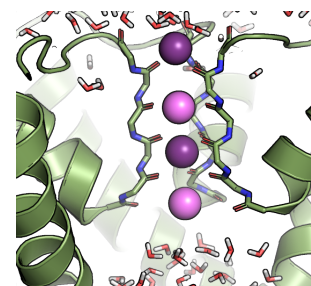


Table 11.6: **Data statistics for the anomalous differences from 1r3j used for determination of the relative occupancies with SHELXD.** Res: Resolution shell; #data: measured number of reflections; #pred: theoretically possible number of reflections; %compl: data completeness, i.e. %compl = #data/#pred. Statistics are from XPREP.

Res. (Å)	# data	# pred.	% compl.	$\langle I/\sigma I \rangle$
$\infty - 7.80$	857	1088	78.8	2.93
7.80 – 5.37	1992	2187	91.1	2.92
5.37 – 4.29	2860	3054	93.6	2.45
4.29– 3.76	2869	3022	94.9	2.30
3.76– 3.42	2889	3031	95.3	2.42
3.42– 3.18	2835	2975	95.3	2.59
3.18– 3.00	2789	2918	95.6	2.60
3.00– 2.85	2890	3005	96.2	2.68
2.85– 2.73	2777	2886	96.2	2.52
2.73– 2.62	3019	3148	95.9	2.56
2.62– 2.53	2854	3006	94.9	2.50
2.53– 2.45	2885	3045	94.7	2.24
2.45– 2.38	2816	3007	93.6	2.19
2.38– 2.31	3130	3376	92.7	2.13
2.31– 2.26	2466	2672	92.3	2.01
2.26– 2.20	3251	3540	91.8	1.99
2.20– 2.16	2359	2587	91.2	1.93
2.16– 2.11	3127	3475	90.0	1.86
2.11– 2.07	2749	3055	90.0	1.83
2.07– 2.03	2922	3283	89.0	1.73
2.03– 2.00	2557	2938	87.0	1.65
2.10– 2.00	7528	8498	88.6	1.73
$\infty - 2.00$	56893	61292	92.8	2.26

Table 11.7: Anomalous peak density for all four  $\text{Tl}^+$  ions in 1r3j. There are no peaks near S atoms above the noise level of about  $5\sigma$ . The height is measured in standard deviations  $\sigma$  of the map.  $\Delta_{\text{peak}}$  denotes the distance between the peak and the respective ion.

	$S_1$	$S_2$	$S_3$	$S_4$
$\sigma$	86.1	85.3	83.3	82.1
$\Delta_{\text{peak}}(\text{\AA})$	0.01	0.02	0.01	0.03

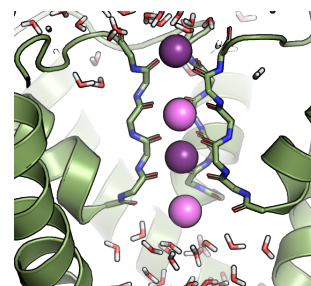


Table 11.8: Anomalous peak density for all four  $K^+$  ions in 3ldc. The two highest S peaks are included for comparison. The height is measured in standard deviations  $\sigma$  of the map.  $\Delta_{\text{peak}}$  denotes the distance between the peak and the respective ion/atom.

	$S_1$	$S_2$	$S_3$	$S_4$	$S_\delta(\text{Met73})$	$S_\gamma(\text{Cys77})$
$\sigma$	18.7	16.7	14.2	19.3	7.8	6.9
$\Delta_{\text{peak}}[\text{\AA}]$	0.09	0.01	0.23	0.09	0.09	0.23



Table 11.9: Data statistics for the data set 2qks as deposited in the PDB. Res: Resolution shell; #data: measured number of reflections; #pred: theoretically possible number of reflections; %compl: data completeness, i.e.  $\%compl = \#data/\#pred$ . Statistics are from XPREP.

Res. (Å)	# data	# pred.	% compl.	$\langle I/\sigma I \rangle$
$\infty - 8.14$	666	941	70.8	33.63
8.14 – 5.77	1550	1632	95	33.21
5.77 – 4.65	2190	2281	96	31.71
4.65 – 4.08	2233	2311	96.6	32.18
4.08 – 3.72	2211	2269	97.4	29.81
3.72 – 3.46	2183	2238	97.5	27.4
3.46 – 3.26	2241	2288	97.9	24.21
3.26 – 3.10	2173	2219	97.9	21.32
3.10 – 2.97	2172	2210	98.3	18.42
2.97 – 2.85	2372	2410	98.4	16.46
2.85 – 2.76	2048	2077	98.6	13.82
2.76 – 2.67	2347	2376	98.8	12.16
2.67 – 2.60	2041	2056	99.3	10.07
2.60 – 2.53	2309	2323	99.4	8.91
2.53 – 2.47	2201	2208	99.7	7.65
2.47 – 2.41	2389	2400	99.5	6.6
2.41 – 2.36	2216	2223	99.7	5.6
2.36 – 2.32	1875	1879	99.8	5.09
2.32 – 2.27	2594	2600	99.8	4.51
2.27 – 2.23	2209	2212	99.9	3.87
2.23 – 2.20	1770	1814	97.6	3.42
2.30 – 2.20	5548	5597	99.1	3.88
$\infty - 2.20$	43990	44962	97.8	15.9

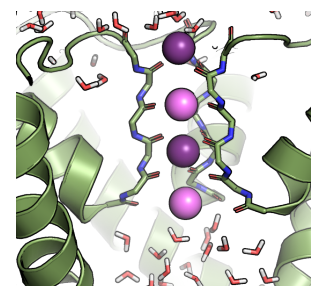


Table 11.10: Estimate of the strength of the anomalous signal in 1r3j. The signal is considered significant up to  $\Delta F_{ano}/\sigma_{ano} > 1.3$  [?]

d (Å)	$\infty$	-8.0	-6.0	-5	-4.0	-3.5	-3.2	-3	-2.8	-2.6	-2.4	-2.2	-2
$\Delta F_{ano}/\sigma_{ano}$	1.64	1.56	1.54	1.25	1.33	1.5	1.49	1.54	1.44	1.33	1.21	1.07	

Table 11.11: Data statistics for the data set 3ldc as deposited in the PDB. Res: Resolution shell; #data: measured number of reflections; #pred: theoretically possible number of reflections; %compl: data completeness, i.e.  $\%compl = \#data/\#pred$ . Statistics are from XPREP.

Res. (Å)	# data	# pred.	% compl.	$\langle I/\sigma I \rangle$
$\infty - 5.70$	250	343	72.9	63.24
5.70 – 3.95	581	606	95.9	72.69
3.95 – 3.15	834	836	99.8	71.59
3.15 – 2.75	840	842	99.8	60.73
2.75 – 2.50	821	822	99.9	55.8
2.50 – 2.32	829	830	99.9	47.22
2.32 – 2.18	837	838	99.9	42.36
2.18 – 2.07	821	821	100	35.54
2.07 – 1.98	814	815	99.9	30.83
1.98 – 1.90	863	864	99.9	25.13
1.90 – 1.83	867	867	100	18.59
1.83 – 1.77	854	855	99.9	14.15
1.77 – 1.72	816	817	99.9	11.38
1.72 – 1.67	931	931	100	8.18
1.67 – 1.63	792	793	99.9	6.72
1.63 – 1.59	894	894	100	5.58
1.59 – 1.56	729	729	100	4.49
1.56 – 1.53	784	785	99.9	3.56
1.53 – 1.50	847	847	100	3.18
1.50 – 1.47	914	915	99.9	2.39
1.47 – 1.45	644	659	97.7	1.84
1.55 – 1.45	2943	2959	99.5	2.72
$\infty - 1.45$	16562	16708	99.1	26.13

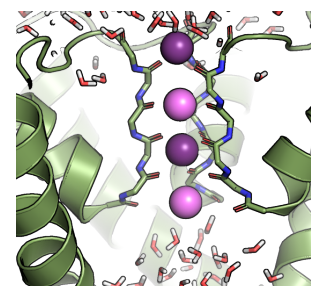


Table 11.12: Data statistics for the anomalous differences extracted from 3ldc. Res: Resolution shell; #data: measured number of reflections; #pred: theoretically possible number of reflections; %compl: data completeness, i.e. %compl = #data/#pred. Statistics are from XPREP.

Res. (Å)	# data	# pred.	% compl.	$\langle I/\sigma I \rangle$
$\infty - 5.32$	182	413	44.1	1.29
5.32 - 3.81	427	636	67.1	0.99
3.81 - 3.12	605	785	77.1	1.19
3.12 - 2.76	609	762	79.9	1.25
2.76 - 2.53	607	744	81.6	1.23
2.53 - 2.36	601	731	82.2	1.26
2.36 - 2.23	599	720	83.2	1.12
2.23 - 2.12	637	762	83.6	1.06
2.12 - 2.03	623	744	83.7	1.02
2.03 - 1.96	561	665	84.4	0.92
1.96 - 1.89	646	769	84	0.99
1.89 - 1.83	604	753	80.2	0.89
1.83 - 1.78	559	715	78.2	0.87
1.78 - 1.73	612	794	77.1	0.93
1.73 - 1.68	675	880	76.7	0.91
1.68 - 1.64	564	790	71.4	0.89
1.64 - 1.60	628	877	71.6	0.77
1.60 - 1.56	644	963	66.9	0.84
1.56 - 1.53	483	785	61.5	0.84
1.53 - 1.49	639	1146	55.8	0.75
1.49 - 1.45	575	1267	45.4	0.76
1.55 - 1.45	1540	2951	52.2	0.77
$\infty - 1.45$	12080	16700	72.3	0.98

# Curriculum Vitae

## Personal

Name: David Alexander Köpfer  
 Address: Goßlerstraße 44, 37075 Göttingen, Germany  
 Birth date: 06.01.1984, Tübingen, Germany

## Education

01/2011 – present: PhD at the Max Planck Institute for Biophysical Chemistry  
 in the group for Biomolecular Dynamics, Göttingen, Germany  
 Supervisor Bert L. de Groot  
 10/2004 – 05/2010: Diploma in biophysics at the TU Kaiserslautern, Germany  
 09/2007 – 05/2008: Two semesters with the European exchange program Erasmus  
 at the Université de Provence, Marseille, France  
 08/2003 – 07/2004: compulsory civilian service (“Zivildienst”)  
 as a paramedic with the German red cross  
 08/2000 – 07/2001: Year at the South High School in Minneapolis, Minnesota, USA  
 08/1997 – 06/2003: Abitur Starkenburg-Gymnasium, Heppenheim, Germany

## Awards

02/2012 – present: Excellence Stipend of the Göttingen Graduate School for  
 Neurosciences, Biophysics, and Molecular Biosciences  
 02/2007 – 05/2010: Fellow of the “Studienstiftung des Deutschen Volkes”  
 (German National Merit Foundation)

